UNIVERSITY OF CALIFORNIA
RIVERSIDE

The Feasibility of a Transparent Cranial Implant for Chronic Structural and Functional Brain Imaging

A Dissertation submitted in partial satisfaction
of the requirements for the degree of

Doctor of Philosophy

in

Mechanical Engineering

by

David L. Halaney

March 2021

Dissertation Committee:
Dr. Guillermo Aguilar, Chairperson
Dr. Lorenzo Mangolini
Dr. Suveen Mathaudhu

The Dissertation of David L. Halaney is approved:

_____

_____

_____

Committee Chairperson

University of California, Riverside

Acknowledgments

I would like to thank all of the researchers and mentors with whom I have had the pleasure of working on this and other related projects. Each of my Dissertation Committee members has provided me with extensive professional guidance and has taught me a great deal about scientific research. I would especially like to thank Dr. Guillermo Aguilar, the chairman of my committee and my primary PhD advisor, from whom I have learned so much. I would also like to thank Dr. Thomas E. Milner for his mentorship and guidance throughout this program and my entire career.

I would like to thank my parents, whose love and guidance have led me to where I am today. Above all, I would like to thank my wife, Sarah Halaney, and my children, Spencer Thompson, Sterling Thompson, and Roselyn Halaney, for their unwavering support, encouragement and love during this PhD program; they made this accomplishment possible.

ABSTRACT OF THE DISSERTATION

The Feasibility of a Transparent Cranial Implant for Chronic Structural and Functional Brain Imaging

by

David L. Halaney

Doctor of Philosophy, Graduate Program in Mechanical Engineering
University of California, Riverside, March 2021
Dr. Guillermo Aguilar, Chairperson

A variety of medical conditions (e.g., traumatic brain injury, cerebral edema, stroke, brain tumors) necessitate surgical craniectomy to access the brain, followed by the placement of a cranial implant to replace the excised cranial bone. Cranial implants provide mechanical protection to the brain, and are made from a variety of materials ranging from polymers to metals and ceramics. Despite this variety of implant options, all current cranial implants for patient use lack optical transparency which could allow for brain imaging or therapy without additional open-skull procedures. The "Window to the Brain" is a novel transparent cranial implant made from a tough, biocompatible ceramic called nanocrystalline-Yttria Stabilized Zirconia. Preliminary studies have shown that this material allows for acute brain imaging *in vivo*, but its suitability for chronic use has not been established. In this dissertation, I investigated (1) the stability of the optical access provided by the window for chronic brain imaging *in vivo*; (2) functional and structural

imaging techniques across the window; (3) laser bacterial antifouling strategies for use with the window; (4) characterization of the window's optical properties which impact imaging. This work provides answers to some of the key remaining questions regarding the feasibility of a transparent cranial implant for chronic structural and functional brain imaging based on nc-YSZ.

Table of Contents

List of Figures

Chapter 1. Introduction

Cranial implants are indicated in response to a variety of medical conditions, including the reconstruction of congenital defects or traumatic injury, or following surgical craniectomy to treat cerebral edema, stroke, or brain cancer. These implants provide mechanical protection to the brain in place of the missing cranial bone, and are currently made from a wide variety of materials ranging from polymers to metals and ceramics [1]. Despite this variety of materials, current cranial implants all lack optical transparency which could allow for brain optical imaging or therapy without implant removal or additional open skull procedures.

Transparent cranial windows have been used extensively in animal models to study brain function and dysfunction, neuropathologies, and to develop new theranostic approaches. These studies use cranial windows made from glass or transparent polymers [2-4], which are powerful research tools but which lack the mechanical toughness required for clinically-viable implants for patient application. My PhD dissertation work has centered around a novel transparent, tough, biocompatible ceramic material, nanocrystalline Yttria-Stabilized Zirconia (nc-YSZ), and investigating its potential as a "Window to the Brain" cranial implant for permanent use in patients.

As the toughest of the ceramic materials, conventional (microcrystalline) Yttria-Stabilized Zirconia (YSZ) has been used for decades as a prosthetic material to replace bone (e.g., for femoral caps) and tooth (e.g., for dental crowns). Conventional bulk YSZ ceramic is densified from a precursor YSZ nanopowder using sintering, a diffusion process which uses heat and pressure to join the nanopowder into a solid mass. During sintering,

recrystallization results in grain growth, yielding a bulk material with grains and pores on the micron scale. Refractive index variations on this size scale (between pores and grains) are highly scattering to visible light, causing the bulk ceramic to appear optically opaque. Recent developments in material processing have allowed for much higher densification rates, using a technology called Current-Activated Pressure-Assisted Densification (CAPAD) [5]. CAPAD uses electric current to rapidly heat the material, reducing densification times from hours to minutes. CAPAD densification is based on defect-mediated plastic deformation rather than diffusion, and the shortened densification time does not allow for grain growth to progress, resulting in a nanocrystalline bulk material. The nanoscale grains and pores reduce light scattering compared to conventional YSZ, and result in optical transparency, particularly in the near-infrared (NIR).

Prior to my dissertation work, the concept of a Window to the Brain cranial implant based on nc-YSZ underwent an initial test to compare optical coherence tomography (OCT) structural brain imaging through the window vs. through the native skull in an acute mouse model. This seminal study showed that a higher signal-to-noise ratio and greater depth of imaging could be achieved across the nc-YSZ compared to the mouse skull [6]. My dissertation work has built upon this foundation, to address some of the most important aspects of the central question: Can the Window to the Brain fulfill its promise of allowing for chronic optical access to the brain for optical imaging and/or therapy?

To answer this question, I developed a survival Window to the Brain cranioplasty mouse model to allow for chronic imaging studies. This model involved the development of procedures to thin, polish, and cut the nc-YSZ bulk samples into mouse cranial windows,

and craniectomy surgery and cranial implant fixation to the skull. This model allowed for investigation of structural and functional imaging across the window over time, to determine if the optical access provided by the Window to the Brain remains stable. Chapters 2 and 3 provide the results of these chronic studies. In Chapter 2, Laser Speckle Imaging (LSI) is applied across the window to image cerebral microvasculature and cerebral blood flow immediately after the cranioplasty, and during recovery in the weeks that follow [7]. Chapter 3 expands on this work, applying OCT structural brain imaging and OCT angiography to determine if the transparency across the window is maintained over 4 weeks [8]. These studies demonstrate that the window is well tolerated *in vivo*, and optical access is not lost due to the body's response (i.e., no inflammation or fibrotic encapsulation of the implant).

In Chapters 4 and 5, the optical range applied through the window is expanded beyond the NIR range of LSI (810 nm) and OCT (1300 ± 68 nm). In Chapter 4, Multispectral Reflectance Imaging (MSRI) is combined with LSI to provide vein-artery separation in cerebral vasculature flow maps [9]. MSRI uses wavelengths ranging from 560 nm – 610 nm to detect the ratio of oxygenated to deoxygenated hemoglobin, allowing for veins and arteries to be distinguished. In Chapter 5, the optical access across the window is examined using longer wavelengths (900 nm up to 2400 nm), as well as imaging across the scalp and window after topical application of optical clearing agents to render the scalp temporarily transparent [10]. These studies extend the usefulness of the window for eventual patient applications, by providing more information about the underlying tissue and avoiding the need for scalp resection to access the window for imaging.

In Chapters 6 and 7, other potential pitfalls for chronic use of the window are investigated. While chronic studies in Chapters 2 and 3 demonstrate that the window remains clear over time in a healthy subject, bacterial fouling and biofilm formation is the primary cause of conventional cranial implant failure and could preclude optical access to tissue underlying the window. For conventional opaque cranial implants, bacterial fouling necessitates removal and replacement of the fouled implant through an additional open-skull procedure. The transparency of the Window to the brain creates the opportunity to use laser bacterial anti-fouling strategies of the implant *in situ*. In Chapter 6, laser antifouling of nc-YSZ is investigated *in vitro* in cultures of *Escherichia coli (*E. coli) using NIR continuous wave and ms pulsed laser treatments [11]. Another potential pitfall for zirconia ceramics is the potential for low-temperature degradation ageing over years in the body. During this process, cubic and tetragonal grains in the YSZ can undergo phase transformation to monoclinic phase. The associated change in grain volume causes cracks to form in the sample, compromising its mechanical properties and potentially leading to catastrophic failure. This topic has undergone extensive study for conventional microcrystalline YSZ, and ISO testing standards have been developed to ensure ageing resistance of zirconia ceramics intended for implantation. In Chapter 7, ISO ageing protocols are followed to simulate a lifetime of *in vivo* ageing, and the nc-YSZ is shown to undergo no phase transformation, nor change in optical transmittance or Vickers Hardness [12]. These studies demonstrate that nc-YSZ is well suited for chronic implementation as a cranial prosthetic.

Finally, after establishing that the nc-YSZ Window to the Brain allows for chronic brain imaging by a variety of modalities and wavelengths, I expand on the characterization of key underlying optical properties of nc-YSZ. Understanding these properties is critical to the design of imaging strategies and interpretation of imaging results across the window. In Chapter 8, swept-source OCT is used to measure the group refractive index and chromatic dispersion by the window. These properties are investigated over the range of working temperatures at which the implant can be used *in vivo*. While the results I present in this dissertation are a proof-of-concept that this implant can fulfill its promise to provide long-term optical access to the brain, there is much more work to be done before this technology can benefit patients. In Chapter 9, I provide my recommendations on next steps and future directions to realize the potential of this novel Window to the Brain.

Chapter 2. Evaluation of a Transparent Cranial Implant as a Permanent Window for Cerebral Blood Flow Imaging

Background

Laser speckle imaging (LSI) is a widely used imaging technique which is capable of distinguishing between static and dynamic regions of a sample. Due to its high spatiotemporal resolution, this technique has proved useful for a range of applications such as object velocity measurements [13], blood flow sensing [14], laser vibrometry [15], surface roughness evaluation [16], and acousto-optic tomography [17, 18], as well as imaging blood flow [14, 19-33].

The first application of LSI to cerebral blood flow imaging [20] used LSI spatial contrast analysis [19]. Subsequently, LSI temporal contrast was developed [21, 22], which allowed for reduced static noise and improved spatial resolution compared to LSI spatial contrast analysis, at the expense of temporal resolution. In LSI temporal contrast imaging, a coherent source is directed onto a roughened surface, and the scattered light produces a random interference pattern called speckle [23, 24]. Movement of scattering particles within the random medium causes phase shifts in the scattered light and thus changes the random interference pattern, producing temporal fluctuations in the speckle pattern [23, 24]. When this speckle pattern is imaged with a camera of limited exposure time, these temporal fluctuations in the speckle pattern corresponding to dynamic regions of the sample appear smoother than the surrounding static regions [25, 34]. The degree of smoothness is measured as speckle contrast, and previous studies applying LSI to cerebral

blood flow have shown that this speckle contrast correlates with blood flow velocity [23, 25].

This improved method of LSI temporal contrast imaging was applied to intact rat skull [26], but the poor transparency of the skull resulted in limited spatial resolution of the underlying blood flow. Previous studies have addressed this challenge in animal models by thinning [27] or polishing [28] the skull, optically clearing the skull [29], or by replacing a portion of skull with a transparent window made from glass or PDMS [2-4], which are powerful research techniques but which are not appropriate for human application as permanent cranial implants for patients. Skull thinning and polishing techniques affects protection for the brain, glass-based windows have extremely low fracture toughness of typical glasses (K_{IC} = 0.7-0.9 MPa $\cdot$ $m^{1/2}$) [35] which increases potential for catastrophic failure by fracture, and the effect of skull optical clearing agents for long-term use on human skull is unknown. A number of biomedical considerations including biocompatibility, mechanical strength, and ageing should be examined in order to create an optical window for eventual clinical application. Conventional cranial prosthesis including titanium, alumina, and acrylic [36], have not provided the requisite combination of transparency and toughness required for clinically-viable transparent cranial implants. To address this challenge, our group has previously introduced a transparent nanocrystalline yttria-stabilized-zirconia cranial implant material, which possesses the mechanical strength and biocompatibility which are prerequisites for a clinically-viable permanent cranial implant for patients [6, 37, 38]. Yttria stabilized zirconia (YSZ)

represents an attractive alternative, due to its relatively high toughness (K_{IC} ~8 MPa · $m^{1/2}$) [39], as well as its proven biocompatibility in dental and orthopedic applications [40-42].

We have previously shown that this implant, which we refer to as the "Window to the Brain" implant (WttB), allows for increased imaging depth and contrast compared to the native skull for optical coherence tomography (OCT) [6] as well as ultrasound [43]. In this chapter, we expand upon previous indications that this WttB implant allows for improved LSI spatial resolution of brain blood flow compared to imaging through the native skull in mice [44]. Specifically, we investigate the stability of the WttB implant for LSI temporal contrast imaging by comparing the sharpness of mouse cerebral blood flow images over 28 days. We also compare LSI temporal contrast imaging between the WttB implant and native skull in a long-term mouse at 60 days post-implantation.

Methods

Implant Fabrication and Preparation

Transparent nanocrystalline 8 mol% $YO_{1.5}$ yttria-stabilized zirconia (nc-YSZ) implant samples were produced from a precursor YSZ nanopowder (Tosoh USA, Inc., Grove City, OH, USA) densified into a transparent bulk ceramic via Current-Activated Pressure-Assisted Densification (CAPAD) as described previously [5]. The resulting densified YSZ ceramic discs were 19 mm in diameter and 1 mm thick. The thickness of the discs were reduced from 1 mm to ~300 μm by polishing with 30 μm diamond slurry on an automatic polisher (Pace Technologies, Tucson, Arizona USA). The samples were then polished on both faces with successively finer diamond and silica slurries ranging from 6 to 0.2 μm to reduce light scattering by the implant surfaces and thus increase transparency

. Samples were sectioned into rectangles of approximately 2.1 x 2.2 mm using a diamond lapping saw (DTQ-5, WEIYI, Qingdao, China), followed by sonication in acetone and thorough rinsing in water. Optical transmittance and reflectance spectra for the polished implants are shown in Figure 2.1.

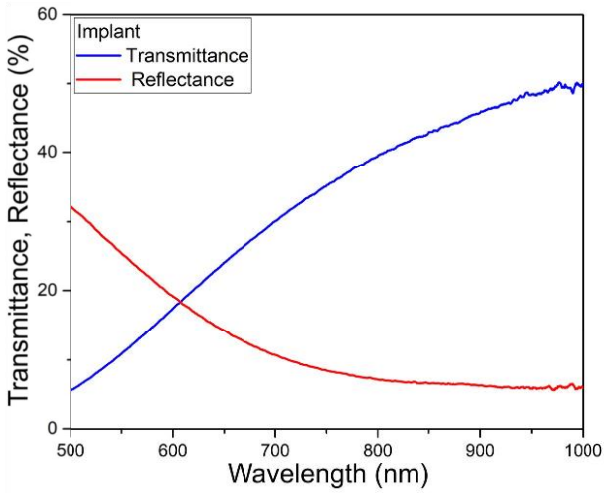

Figure 2.1. Reflectance and transmittance spectra of the Window to the Brain implant.

Animals

All experimental procedures and humane care of mice were conducted in compliance with the University of California, Riverside Institutional Animal Care and Use Committee approval. The n = 4 8-12-week-old C57Bl/6 male mice (Jackson Laboratory) used in this study were housed under a 12-hour light and 12-hour dark cycle with *ad libitum* access to food and water.

Surgical Procedures

Craniectomy surgery was conducted as previously described [44]. Briefly, mice were anesthetized with isoflurane inhalation (0.2-0.5%), and given ketamine and xylazine (K/X)

(80/10 mg/kg, i.p.). Additional anesthetic was administered as necessary. Hair was removed from the scalp using clippers and depilatory cream. Mice were then secured into stereotaxic frames to immobilize the head for surgery. Ophthalmic ointment was placed over the eyes, and the surgical site was sterilized with alternating application of betadine and 70% EtOH (3 times). Implants were also sterilized in 70% EtOH.

A sagittal incision was made to the left of the midline, and the scalp retracted to expose the skull. Periosteum was removed from the skull, and a craniectomy was performed with a surgical drill and carbide burr to remove a square section of skull over the right parietal lobe, with dimensions slightly larger than the implant. The YSZ implant was placed within the craniectomy directly on the intact *dura mater*, and dental cement was applied to each of the four corners of the implant to prevent displacement. Dental cement was cured with UV light exposure for 20 seconds. Figure 2.2(a) shows an illustration of implant placement envisioned in eventual human application, as well as implant placement used in mice in this study.

Imaging with LSI was conducted immediately after the cranioplasty procedure, while the scalp was still open, as well as follow-up imaging at 14 and 28 days (for Mice 1-3), or 60 days (for Mouse 4) after the implantation surgery. For each follow-up imaging procedure, mice were anesthetized as described above, and the scalp was reopened to expose the implant. Periosteum overlying the implant (and skull for Mouse 4) was removed, and imaging was conducted in an identical manner to the baseline imaging. During imaging sessions, small amounts of saline was dropped onto the skull periodically to prevent drying. Following each imaging procedure, the scalp was closed with

continuous suture, and triple antibiotic ointment was applied to the surgical site. Buprenorphine was administered (0.1 mg/kg, s.c.) for postoperative pain control. Mice were placed on a heating pad to aid recovery from anesthesia. A second buprenorphine injection was administered between 4 and 6 hours after surgery.

Laser Speckle Imaging

LSI and regular images of regions of interest (ROI) (Figure 2.2(c)) were acquired using a 12-bit CMOS camera (DCC1545M, Thorlabs, Newton, NJ, USA). For regular images, a diffuse IR source was used for illumination. For LSI, an 810 nm continuous wave NIR laser (Vari-Lase REF946, Vascular Solutions, Morrisville, NC, USA) was used to illuminate the ROI with incident power of 100 mW at a 45° incidence. While most LSI studies use visible wavelengths for illumination, we chose 810 nm to reduce reflectance and increase transmittance through the implant (see Figure 2.1). The 810 nm laser intensity was homogenized using a diffuser (ED1-C20-MD, Thorlabs) and was expanded using a pair of negative-positive lenses (KPC043, −25 mm EFL and KPX094, 100 mm EFL, Newport, Irvine, CA, USA). Collimated laser light was shown onto the cortex through the WttB implant (i.e., ROI 1 in Mice 1-3) or through both skull and implant (i.e., ROI 1 and ROI 2 in Mouse 4). A sequence of laser speckle images reflected from each illuminated region was captured by the CMOS camera, which was focused 0.2 mm below the cortical surface using a 10X zoom microscope (MLH-10X, 152.4 mm WD, Computar, Torrance, CA, USA). For each ROI, a sequence of n = 100 images were captured at each of four different exposure times (1, 2, 6, and 10 ms) at a speed of 14 frames per second. The aperture and magnification of the zoom microscope were carefully chosen to ensure that

the speckle size at the image plane was approximate to the area of a single pixel in the CMOS chip [21, 26, 30]. A schematic of the LSI system is shown in Figure 2.2(b).

Experimental Design

In this study, we conducted two separate experiments. Experiment 1 was conducted using mice 1-3, with LSI through the implant (i.e., ROI 1) at baseline immediately following implantation, and again after 14 and 28 days post-implantation. In Experiment 2, the LSI field of view was expanded to include both the implant (ROI 1) as well as native skull (ROI 2) in Mouse 4 at 60 days post-implantation. For both experiments, LSI imaging was conducted at 4 different exposure times. A timeline of imaging procedures for the two experiments is shown in Figure 2.2(d).

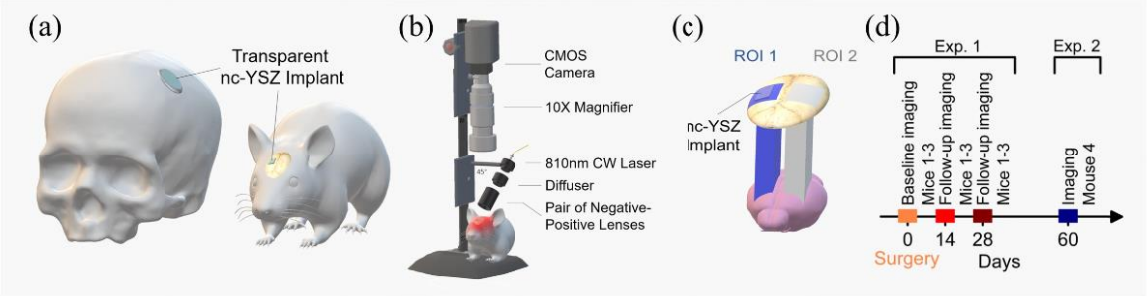

Figure 2.2. a) Illustration of the Window to the Brain concept in human and mouse skulls, b) Schematic of the experimental imaging setup, c) Schematic of the craniotomy location on murine cranium and regions of interest: ROI 1, the nc-YSZ implant and ROI 2, the left parietal bone, d) Timeline for imaging procedures.

Image Processing and Data Analysis

The contrast-resolved LSI images were constructed based on temporal statistical analysis of laser speckle which has been proven to preserve spatial resolution [26]. Experimental results have indicated that temporal speckle contrast analysis could expressively suppress the effect of the static laser speckle pattern formed by the stationary superficial reflection

and scattering tissue on the visualization of blood flow [21, 26, 30-32]. Suppressing this effect makes temporal contrast analysis an ideal method for imaging cerebral blood flow through skull and the transparent nc-YSZ implant. The temporal contrast, K_t, of each image pixel in the time sequence was calculated using Eq. (1) [21],

$$K_t(x,y) = \frac{\sigma_{(x,y)}}{\langle I_{(x,y)} \rangle} = \sqrt{\frac{1}{(N-1)} \left\{ \sum_{n=1}^{N} [I_{(x,y)}(n) - \langle I_{(x,y)} \rangle]^2 \right\}} \Big/ \langle I_{(x,y)} \rangle \quad (1)$$

where $I_{x,y}(n)$ is the intensity at pixel (x,y) in the nth image, N is the number of images acquired, and $\langle I_{x,y} \rangle$ is the mean value of intensity at pixel (x,y) over the N images.

We assessed the quality of the speckle contrast images over time in terms of signal to noise ratio (SNR) and vessel sharpness. To quantify signal to noise ratio for each exposure time and time point, the contrast intensity profile along a vertical line (across the blood vessels) was considered. The profile lines were chosen for each mouse such that 3 to 4 vessels were intersected, and remained the same between the time points and the exposure times. Figure 2.3(b) shows an example of the contrast intensity profile for 6 ms exposure time at day 0, 14 and 28 for Mouse 3. Equation (2) shows how SNR values were calculated for each exposure time and time point,

$$SNR = \Delta K / \sigma K_n \quad (2)$$

where ΔK is the depth of the vessel peak from the baseline (mean noise) and σK_n is the standard deviation of the noise. A visual example of ΔK and σK_n are shown in Figure 2.3(b). The SNR values were averaged over the mice (1, 2, and 3) and standard errors were calculated. The optimum SNR between the exposure times in each time point was chosen for the contrast images sharpness comparison. As an indicator of resolution, we compared the sharpness of the vessel edges in images by calculating fall distance (the number of pixels) of the edge of the vessel to go from 10% to 90% of ΔK value were calculated [45]. A shorter fall distance corresponds to greater sharpness. The same sampled contrast intensity profiles were considered for the fall distance calculation. Figure 2.3(b) shows an example trace and 10–90% fall distance measurement. In order to evaluate the change in sharpness over the time points in Experiment 1, relative change in fall distance over the time points day 14 and day 28 compared to day 0 baseline for each animal and vessel were evaluated using Eq. (3).

$$\textit{Relative fall distance} = \frac{\textit{Fall distance} - \textit{Fall distance}_{Day0}}{\textit{Fall distance}_{Day0}} \tag{3}$$

To compare the blood vessel images through-skull and through-implant in Experiment 2, absolute fall distances with respect to the vessels size (FWHM) were determined. FWHM of the vessels in profiles were taken as the vessel diameter [46] (Figure 2.3(b)).

Results

Experiment 1: LSI Image Quality Over Time

The results from Experiment 1 are shown in Figures 2.3 and 2.4. Figure 2.3(a) shows regular images and LSI temporal contrast images at each of the 4 exposure times, for days 0, 14 and 28 from Mouse 3 (data for Mice 1-2 not shown). In the regular images, some tissue regrowth is visible at the implant edges at 14 and 28 days. It should also be noted that at day 0, blood flow is expected to be altered in response to the invasive cranioplasty surgery (e.g., due to potential reactive hyperemia [47] (increased blood flow), changes in respiration, etc.). Due to these differences in the mouse biology and physiology at different imaging time points, we sought to determine the optimal exposure time for LSI imaging at each time point, so that we could compare the images of highest SNR that could be acquired at each time point.

Line intensity profiles like the example shown in Figure 2.3(b) were analyzed for all exposure times and imaging time points in Mice 1-3. From these intensity profiles, peak intensity and noise were determined (as described in the Methods section and illustrated in the inset of Figure 2.3(b)), and signal-to-noise ratio (SNR) was calculated. Data for each time point and exposure time was averaged between the three mice, and is shown in Figure 2.4(a). As shown in the figure, an exposure time of 6 ms gave the highest SNR at 0 and 28 days, while 10 ms exposure time gave a higher SNR at 14 days.

Next, using the 9 LSI temporal contrast images corresponding to these optimal exposure times for days 0, 14 and 28 for Mice 1-3, we sought to compare the sharpness (i.e., fall distance) of the vessels in the images to determine if the images were becoming

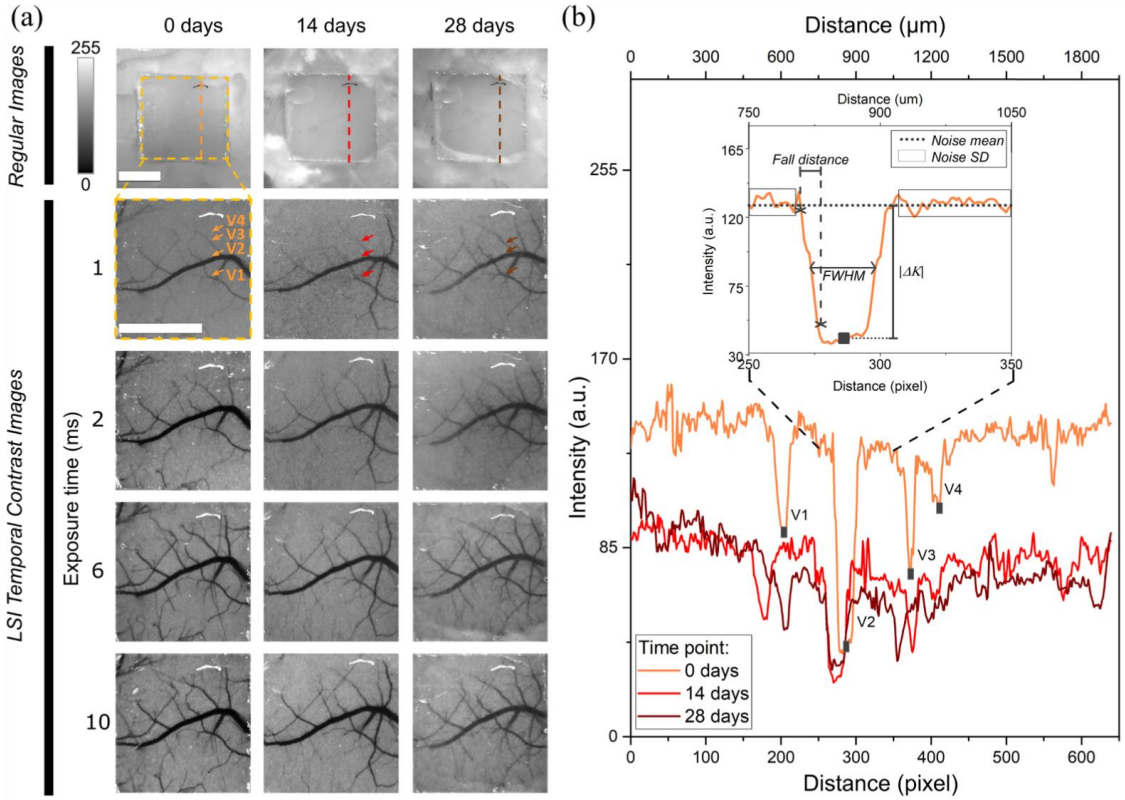

Figure 2.3. a) Regular images and LSI images for exposure times of 1, 2, 6, and 10 ms, at 0, 14 and 28 days post-surgery from Mouse 3 (scale bars = 1 mm). b) Contrast intensity profiles of lines across the images (shown as a dashed line in panel a) at 0, 14 and 28 days post-surgery from Mouse 3. The arrows in a) show the vessels that are intersected by the profile lines shown in b), labeled as V1 through V4 in day 0 image and profile (V4 arrow was not shown in day 14 and day 28 since the microvessel is not visible). The inset in b) shows how noise parameters, |ΔK|, FWHM and fall distance are determined from the line profiles.

blurred and losing resolution over time since implantation. The relative change in fall distance between days 14 and 28 compared to day 0 baseline are shown in Figure 2.4(b), and was below a 13% increase for all vessels analyzed. On average, relative fall distance increased by 6.56% ± 1.03% by day 14, and 7.69% ± 1.2% by day 28 compared to day 0.

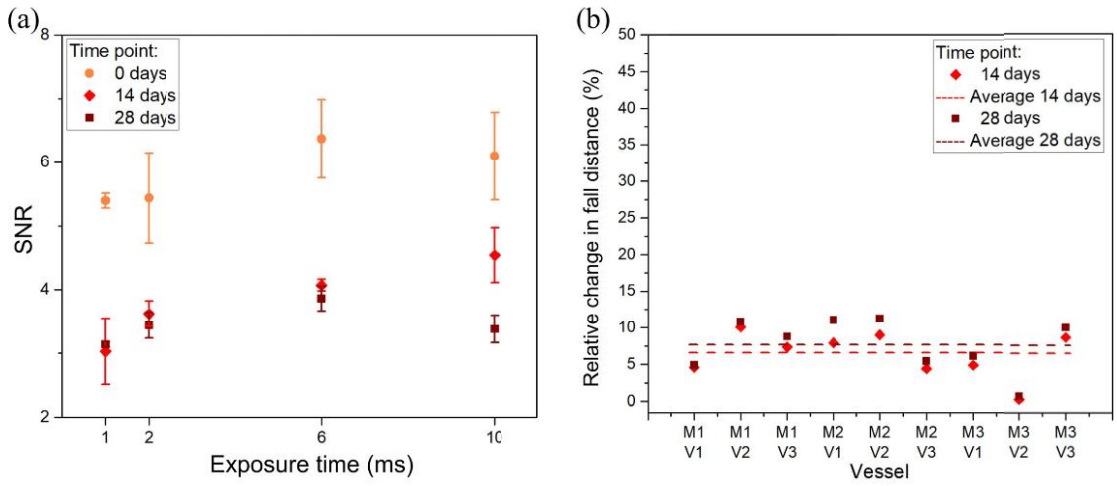

Figure 2.4. a) SNR for different exposure times and imaging time points (mean and standard error) and b) Relative change in fall distance between days 14 and 28 vs day 0 for 3 vessels each of Mice 1-3 (dashed lines represent mean change in fall distance for all 9 vessels).

Experiment 2: LSI Image Quality through Skull vs. Chronic Implant

As the goal of the WttB implant is to provide long-term optical access to the brain for imaging techniques such as LSI, we sought to compare LSI imaging through the native skull with imaging through a chronic implant which had been in the body long term. Thus, in Experiment 2, Mouse 4 was imaged with LSI 60 days post-implantation. To make a direct comparison between the implant and skull, the LSI field of view was expanded to include both ROI 1 (the implant over the right parietal lobe) and ROI 2 (corresponding region of skull over the left parietal lobe) in the same image. Figure 2.5(a) shows the LSI temporal contrast images for exposure times of 1, 2, 6 and 10 ms.

Unlike Experiment 1, where a given field of view was compared with itself over time, Experiment 2 compares two separate regions of the brain with different vessels. Thus, for this second experiment, 3 line profiles with taken for the implant and for the corresponding region of skull. To avoid selection bias, the location of these line profiles

were chosen arbitrarily at the ROI mid- and quarter-points, as depicted in the regular image in Figure 2.5(b). As an example, Figure 2.5(c) shows the intensity profiles from the midline of both ROI 1 and ROI 2 for exposure time 6 ms.

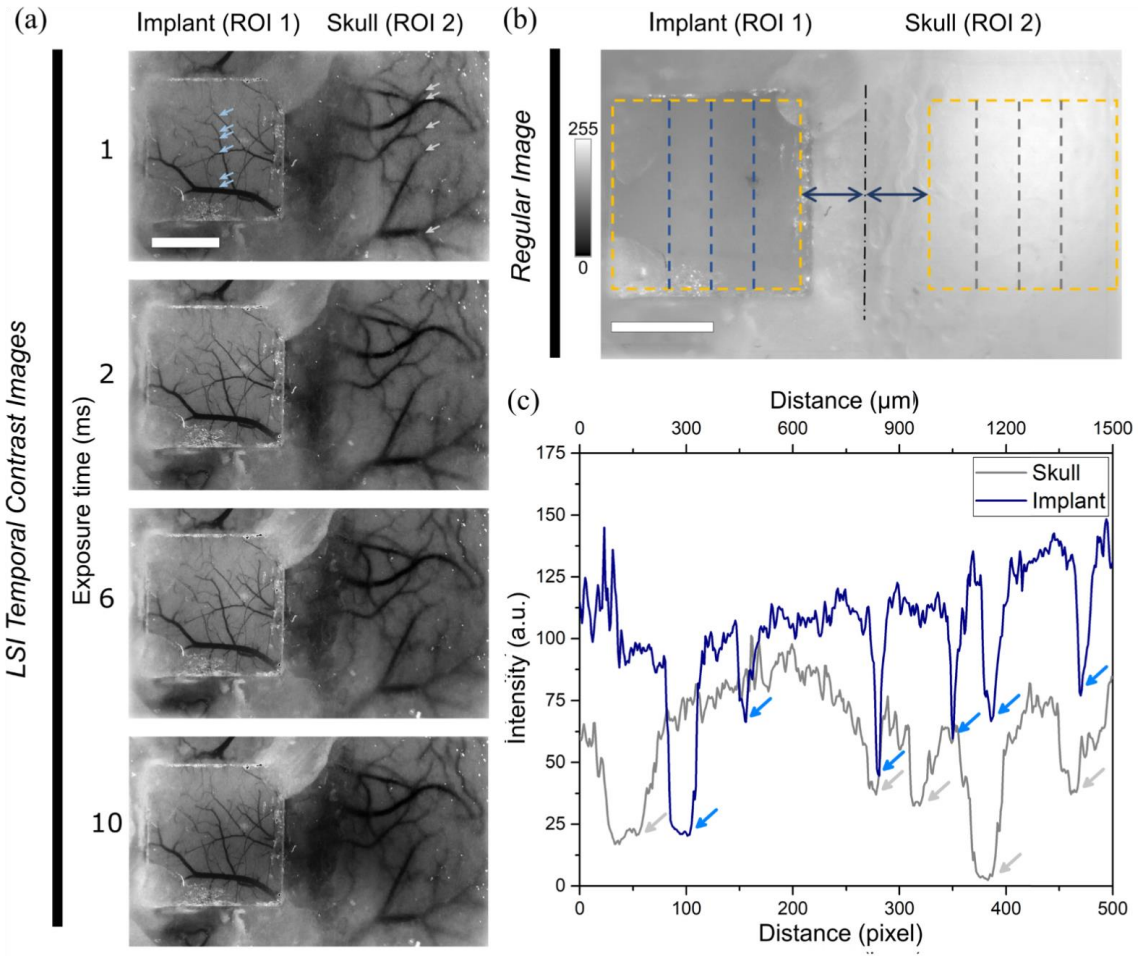

Figure 2.5. a) LSI temporal contrast images for 4 exposure times in Mouse 4. The left side of each image is the WttB implant (ROI 1), and ROI 2 is the corresponding region of skull on the right side of each image. b) Regular image of implant, showing the arbitrary locations where line profiles were taken. c) Example contrast intensity profiles along the midline of ROI 1 and 2 for exposure time 6 ms. The arrows in a) and c) show the vessels that are intersected by the midline intensity profiles. Scale bars = 1 mm.

Using the same analysis methods described in Experiment 1, we calculated the SNR from each line profile in ROI 1 and ROI 2 for each exposure time. The mean SNR for each exposure time is shown in Figure 2.6(a). The 6 ms exposure time LSI temporal contrast

image resulted in the highest SNR for both implant and skull, and thus we used this image to compare the SNR and sharpness of detected vessels by LSI between native skull and a long term WttB implant. By the same method used in Experiment 1, we analyzed the 3 line profiles across the WttB implant and 3 line profiles across the skull to determine the fall distance and SNR for each vessel. Additionally, the full-width half-max (FWHM) of each vessel in the line profiles were taken as vessel diameter [41]. Figure 2.6(b) shows a plot of all vessels intersected by the 6 profile lines, with SNR plotted against FWHM (i.e., vessel diameter). A plot of all vessels intersected by the 6 profile lines, with absolute fall distance (i.e., vessel sharpness) plotted against FWHM (i.e., vessel diameter) is shown in Figure 2.6(c).

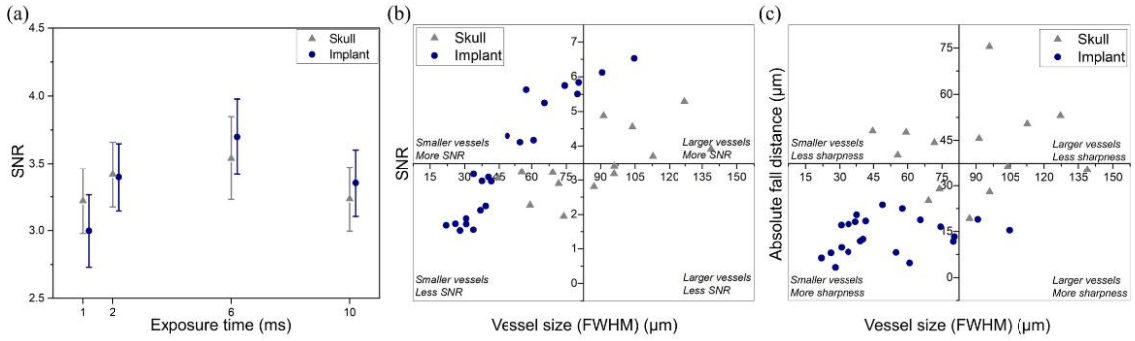

Figure 2.6. a) Mean SNR of contrast intensity along arbitrary line profiles on the implant and skull for 4 separate exposure times (error bars represent standard error), b) and c) SNR and sharpness (respectively) vs FWHM for all vessels intersected by arbitrary line profiles on the implant and skull for the LSI temporal contrast image acquired with 6 ms exposure time.

Discussion

The WttB holds the transformative potential for facilitating diagnosis and treatment of a wide variety of brain pathologies and neurological disorders. We envision this implant having the potential to enable delivery to and/or acquisition of light from the brain, in real-

time, without the need for repeated highly-invasive craniotomies. Such access may also create a new platform for understanding the brain. As the goal of the WttB implant is to provide this access long-term, it is important that the optical access is not lost over time. In this chapter, we assessed LSI temporal contrast imaging quality (i.e., sharpness) of cerebral blood vessels imaged through the implant up to 60 days post-implantation.

In LSI temporal contrast imaging, the exposure time of the camera can have a large effect on image quality. As exposure time increases, both the contrast intensity and noise of the image increase [33]. While the contrast plateaus after some threshold, noise continues to increase with exposure time. Several sources of noise contribute to the measured noise, including physiological noise, hardware noise, environmental noise, and noise due to statistical uncertainties. The total noise of the speckle contrast signal is a combination of all of these sources and the relative contributions of each of these exhibit different characteristics with respect to the exposure time [33]. However, in our experiments, the physiologic noise (including noise due to implantation surgery) is the dominant source because it is the only one that is changing considerably over time. Physiologic noise arises from motion of the tissue such as heartbeat or respiration-induced pulsatile motion of the exposed cortex, baseline fluctuations in the cerebral blood flow, and possibly tissue regrowth and revascularization following implantation. This motion and blood flow fluctuations introduce additional velocity components to the measured signal and therefore cause speckle contrast fluctuations. Since the physiological noises will be different on different days, exposure time should be optimized during each imaging session. To determine the optimal exposure time in this study, we compared the SNR of

images taken at exposure times of 1, 2, 6, and 10 ms (Figure 2.4(a), Figure 2.6(a)), and each imaging session proceeded with the exposure time that maximized SNR. Indeed, our results found that the optimal exposure time differed between the imaging time points in Experiment 1, with maximum SNR for exposure time of 6 ms at days 0 and 28, and 10 ms at day 14. This may be explained by the differences in physiology between these time points. At day 0, altered blood flow due to the implantation surgery is expected, and elevated blood flow could give high contrast to the vessels. Thus, a lower exposure time (6 ms) can provide sufficient contrast of the blood flow, while keeping noise low. By day 14, flow would no longer be modified in response to the surgery, and thus a higher exposure time (10 ms) may be needed to increase contrast in the images. At time points beyond 14 days, flow remains low compared to day 0, but noise may increase due to healing processes (tissue regrowth, revascularization, etc.), and thus a shorter exposure time (6 ms) may provide the best compromise between increased contrast and reduced noise. It should be noted, however, that the modification of blood flow at the different time points, as evidenced by the different optimal exposure times, may also be due to several other confounding factors. Anesthetic agents (including isoflurane and ketamine used in this study) are known to modulate cerebral blood flow, and the concentration of these drugs in the blood stream was not kept constant over the imaging sessions. Respiration can cause noise in LSI, and its rate, along with arterial blood gas levels, can significantly alter blood flow. These variables, in addition to the small sample size used in this study, make it difficult to attribute the observed differences in blood flow between the time points to a particular cause.

Image resolution (i.e., sharpness) was found to decrease by up to 13% over the 28 days compared to day 0 baseline in the 9 vessels analyzed from Mice 1-3 (Figure 2.4(b)). The relative increases in average fall distance between day 14 and day 28 compared to day 0 were 6.56% ± 1.03% and 7.69% ± 1.2%, respectively. It should be noted that while day 0 is considered as the baseline for comparison, it does not represent an unperturbed state of normal cerebral blood flow. It is likely that blood flow was altered in response to the invasive cranioplasty surgery, and thus the higher SNR and sharpness of the day 0 images compared with days 14 and 28 may be due in part to an elevated signal at day 0, rather than a loss of signal at days 14 and 28. SNR and sharpness stayed more stable between 14 and 28 days, consistent with this hypothesis. Additionally, new microvessels which were not visible in day 0 are visible at these later time points, which suggests revascularization may be occurring near the implant surface. Together, these results appear to indicate that image quality remains high up to 28 days post-implantation, but additional longer time points are needed to confirm this is the case. In Experiment 2, a day 60 time point shows that SNR is similar to the SNRs obtained at days 14 and 28 in Experiment 1 (SNR between 3 to 4 in both Figure 2.4(a) and Figure 2.6(a)), and microvessels are clearly visible at this later time point (Figure 2.5(a)).

Comparing imaging through the skull and a long-term (60 days) implant (Figure 2.5(a)), the skull had a higher SNR for lower exposure times (1 and 2 ms), and the implant SNR was higher at longer exposure times (6 and 10 ms) (Figure 2.6(a)). The higher SNR of the throughskull images compared with implant at short exposure times may be explained by the natural filtering-out of smaller vessels imaged through the skull. Imaging

through the window, on the other hand, resolves small vessels which are more sensitive to exposure time. At low exposure time, the contrast of these small vessels is very low, contributing to the lower SNR through the window compared to skull. Exposure time of 6 ms gave the highest SNR for both skull and implant and was used for comparing SNR and sharpness of vessels imaged beneath each. Because this comparison was made between two different spatial regions of the brain, different vessels of varying diameter were compared. Thus, SNR and sharpness of vessels (fall distance) are plotted against the vessel diameter (FWHM of vessels in intensity profiles). As mentioned earlier a number of small vessels, associated with lower blood flow and accordingly SNR, were detected through the implant which were naturally filtered-out by the skull (Figure 2.6(b)). These detected small vessels decreased the averaged SNR shown in Figure 2.6(a). In Figure 2.6(c), interestingly, the data from the skull and implant fell into separate clusters, with vessels imaged through the implant having smaller FWHM and shorter fall distances, while vessels imaged through the skull have larger FWHM and higher fall distances. This data shows that vessels imaged through the implant appear smaller in diameter and have sharper borders compared to those imaged through the skull. As the size of vessels and velocity of blood flow is not expected to differ on average between the two hemispheres of the mouse brain, the apparent increase in vessel diameter imaged through the skull vs implant is likely due to blurring of the image through the skull. In general, the light transmission to the brain and reflection from the brain are lower in the through-skull image. Additionally, the skull scattering disorders the speckle pattern that was created by the brain hemodynamics,

making a less accurate speckle pattern. Both of the defects are caused by skull and the skull texture is not homogeneous, making image correction or enhancement very complex [26].

The reduction in border sharpness of the vessels imaged through the skull vs implant is consistent with this explanation, and the blurred nature of the through-skull image compared to the through-implant image is visually apparent in Figure 2.5(a). It should also be noted that while the SNR and sharpness of the through-implant images are an improvement over the through-skull images, the mouse skull is inherently transparent itself [26], which is not the case in larger animals or humans.

LSI temporal contrast imaging has become a useful tool for brain blood flow applications as the images it produces contain functional information (i.e., relative blood velocity) in addition to showing structure of the vessel networks. Figure 2.7 contains a color map version of the 6 ms LSI image from Mouse 4 (Figure 2.5(a)), where minimum relative velocity (i.e., static regions) appears blue and maximum relative velocity (i.e., maximum blood flow velocity) appears red. As seen in Figure 2.7, much more precise velocity information, particularly of microvessels, can be detected through the implant, while the reduced sharpness of the vessels imaged through skull obscures precise flow determinations. Imaging microvessels (usually involving small arteries of less than 150 μm in diameter, arterioles, capillaries, and venules [48, 49]) is important for many applications, as microcirculation plays a critical role in physiological processes such as tissue oxygenation and nutritional exchange [50]. Monitoring the spatio-temporal characteristics of microcirculation is crucial for studying the normal and pathophysiologic conditions of tissue metabolism. It is also useful for assessing microcirculatory dysfunction

due to disease conditions such as type 2 diabetes, peripheral vascular disease (PVD), atherosclerotic coronary artery disease, obesity, heart failure, Alzheimer's, schizophrenia and hypertension, among others [51-53]. In addition, quantification of dynamic blood flow, angiogenesis, and vessel density are critical for monitoring the progression of wound healing [54]. Although high resolution vascular network mapping is possible using imaging modalities such as computed tomography (CT), these approaches require injection of contrast agents and pose disadvantages such as radiation exposure. Existing non-invasive methodologies (including LSI through skull) are inadequate to study blood flow at microvessel resolution [55]. Windows such as the WttB implant are thus important tools for research, and in the case of the WttB implant, can become important enablers of clinical diagnostics and therapy involving cerebral microvessels.

As recent studies show, creating novel windows for brain studies has been gaining attention recently [4, 56-58]. Some of these studies, involving optical clearing agents (OCAs) applied to the scalp overlying native skull, have shown limited success due to optical losses and scattering in the skull. These skin optical clearing strategies could work in conjunction with the WttB implant, to allow for imaging of cerebral blood flow in awake and behaving animals through closed scalp and implant, for example to study cerebrovascular hemodynamic responses and tissue oxygenation and other stimuli. Future studies by our group will explore this combined OCA-WttB strategy, as well as including additional imaging modalities which can couple with LSI to provide additive information, such as OCT and intrinsic optical signal (IOS).

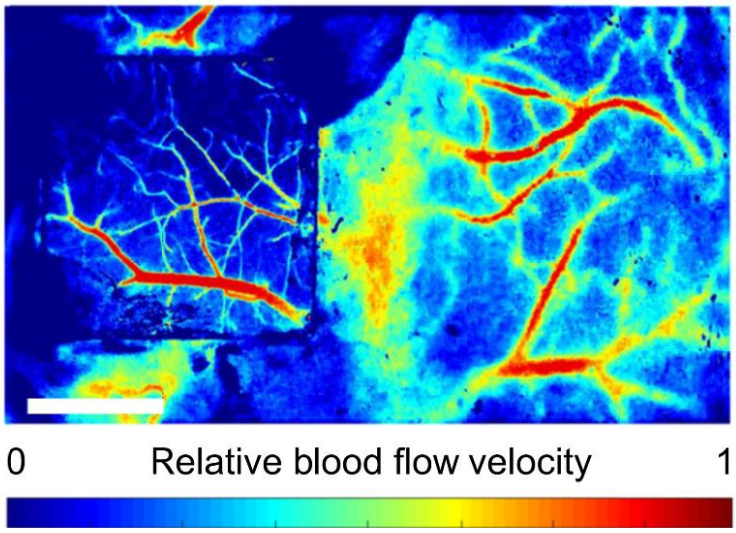

Figure 2.7. Relative blood flow velocity in the 6 ms exposure time LSI temporal contrast image from Mouse 4. Scale bar = 1 mm.

There are several limitations to the current study. The sample sizes used were small (n = 3 and n = 1), and further experiments are needed to confirm the reproducibility of these findings. While a permanent cranial implant can allow for less invasive imaging of the brain at later time points, it requires an initial implantation surgery which carries associated risks such as infection.

Conclusion

In conclusion, the Window to the Brain implant was found to remain stable for LSI imaging up to 28 days, with average relative change in vessel sharpness under 8%. An additional imaging session at 60 days found improved sharpness and visibility of microvessels compared to imaging through skull which blurred and distorted vessels. These results suggest that this implant can provide long-term access for brain imaging, but longer-term studies are needed.

Citation: The work presented in this chapter was published in *Biomedical Optics Express* [7]:

> Davoodzadeh N, Cano-Velazquez M, Halaney D, Jonak C, Binder D, Aguilar G. Evaluation of a transparent cranial implant as a permanent window for cerebral blood flow imaging. *Biomed. Opt. Express* 9, 4879-4892 (2018).

Acknowledgments

I would like to acknowledge the contribution of my co-authors to this work: Nami Davoodzadeh, Mildred S. Cano-Velázquez, Carrie R. Jonak, Devin K. Binder, and Guillermo Aguilar. This work was supported by National Science Foundation (NSF-PIRE) (1545852) and "Beca Mixta" from National Council of Science and Technology of Mexico (CONACYT) (741249). The authors would like to thank Gottlieb Uahengo for the fabrication of the YSZ samples.

Chapter 3. Chronic Brain Imaging across a Transparent Nanocrystalline Yttria-Stabilized-Zirconia Cranial Implant

Background

Repeated non-diffuse optical imaging of the brain is difficult. This is due to the fact that the cranial bone is highly scattering and thus a strong optical barrier. Repeated craniotomies increase the risk of complications and may disrupt the biological systems being imaged, motivating the development of several approaches to image the brain without repeatedly opening the skull. Modalities such as Magnetic Resonance Imaging (MRI), Computed Tomography (CT), Transcranial Doppler Ultrasonography, Positron Emission Tomography (PET), Single-photon Emission Computerized Tomography (SPECT), Near-Infrared Spectroscopy (NIRS), and Fluorescence Spectroscopy (with limited penetration depth) are capable of imaging through the intact skull [59], but limited spatial resolution precludes more detailed studies of brain function and disease using these approaches. Other approaches have focused on mitigating scattering by the skull so that imaging strategies with higher spatial resolution can be applied to the brain. In animal models, these approaches have included thinning [27, 60] or polishing [28] the skull, rendering the skull temporarily transparent using skull optical clearing agents [29], or implanting temporary transparent windows made from glass or polymers [2-4]. These represent powerful scientific tools for studying the brain, but are not feasible for chronic imaging applications in human patients.

We previously introduced a potential solution [6, 7, 11, 12, 37, 43, 61, 62] in the form of a transparent ceramic cranial implant called the Window to the Brain (WttB)

implant. This implant is made of nanocrystalline Yttria-Stabilized Zirconia (nc-YSZ), which possesses the requisite mechanical strength [12] and biocompatibility [37] to serve as a permanent optical access window in human patients. In our previous work, we demonstrated the *in vivo* use of this WttB implant for Optical Coherence Tomography (OCT) imaging of the brain in mice [6] as well as for repeated Laser Speckle Imaging (LSI) of mouse cerebral blood flow [7] over 4 weeks. Our previous OCT study showed an improvement in imaging depth and signal-to-noise ratio (SNR) compared to imaging through unaltered mouse skull; however, the study was acute in nature and did not assess whether imaging quality across the WttB implant is maintained over time. Our LSI study showed that contrast and sharpness of brain vessels improved compared to imaging through the native mouse skull, but could not address the question of whether optical access remains stable over 4 weeks of imaging, as the cerebral blood vessels appeared to have different blood velocities and volumes at the different time points assessed. It was not possible to determine whether this was due to changes in the optical access provided by the WttB implant, or physiologic changes in the mouse between the different time points.

In this chapter, we demonstrate repeated brain imaging of n = 5 mice using both OCT and LSI across the WttB implant over 4 weeks. The main objectives are to determine if the WttB implant allows for chronic OCT imaging, and to shed further light on the question of whether optical access provided by the WttB implant remains stable over this duration in the body.

Methods

Implant Fabrication and Preparation

Implant fabrication and preparation was conducted as described in Chapter 2 (page 8).

Animals

N = 5 8-12 week old C57Bl/6 male mice were purchased from Jackson Laboratory and housed under a 12-hour light and 12-hour dark cycle with *ad libitum* access to food and water. All experiments were approved by the University of California, Riverside Institutional Animal Care and Use Committee, and were conducted in accordance with the National Institutes of Health and Institutional Animal Care and Use Committee guidelines.

Surgical Procedures and Post-Surgical Monitoring and Care

Craniectomy surgery was conducted as described in Chapter 2 (page 9). Craniectomy and implant fixation are shown in Figure 3.1(a, b).

The brain was imaged sequentially with LSI (Figure 3.1(c)) and OCT (Figure 3.1(d)) through the transparent WttB implant immediately after the cranioplasty, while the scalp was still open. Following the baseline imaging procedure, the scalp was closed with continuous suture. Triple antibiotic ointment was applied to the surgical site, and buprenorphine was administered (0.1 mg/kg, s.c.) for postoperative pain control. Mice were placed on a heating pad to aid recovery from anesthesia. A second buprenorphine injection was administered between 4 and 6 hours after surgery.

For follow-up imaging, mice were anesthetized as described above, and the scalp was reopened to expose the implant. Periosteum overlying the implant was removed, and imaging was conducted in an identical manner to the baseline imaging. Following the final

imaging procedure, mice were perfused, and brains were dissected and prepared for sectioning with a cryotome and histologic staining with Haemotoxylin and Eosin (H&E). A timeline of surgical procedures and imaging time points is provided in Figure 3.1(e).

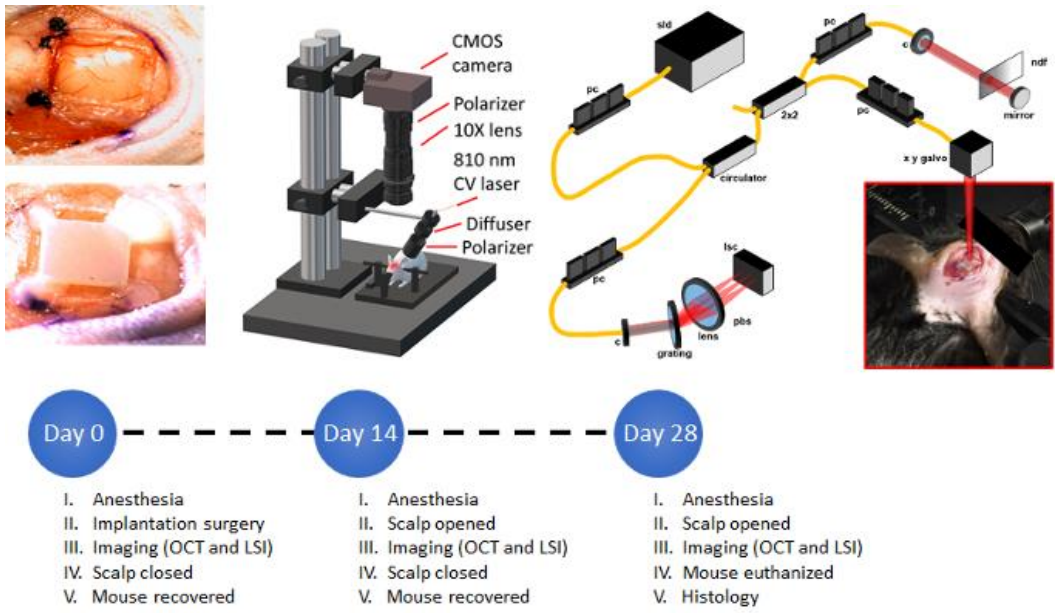

Figure 3.1: Experimental setup a) craniectomy over right parietal lobe showing exposed Dura Mater, b) WttB implant placement within craniectomy and fixation to skull with dental cement, c) illustration of laser speckle imaging system, d) illustration of optical coherence tomography imaging system, e) timeline of surgical and imaging procedures for the n = 5 mice. sld: super-luminescent diodes; pc: polarization controller c: collimator; pbs: polarization beam splitter; pm: polarization modulator; bs: beam splitter; ndf: neutral density filter; lsc: line scanning camera

Laser Speckle Imaging

The region of interest containing the WttB implant was illuminated by an 810 nm continuous wave laser (Vari-Lase REF946, Vascular Solutions, Morrisville, NC, USA) with incident power of 100 mW at a 45° incidence. The laser intensity was diffused and homogenized using an engineered diffuser (ED1-C20-MD; Thorlabs). A pair of negative-positive lenses (KPC043, −25 mm EFL and KPX094, 100 mm EFL; Newport, Irvine, CA) was used to expand the diffused laser light. The reflected light from the illuminated region

was captured by a 12-bit complementary metal-oxide-semiconductor (CMOS) camera (DCC1545M; Thorlabs) equipped with a X10 zoom microscope (MLH-10X, 152.4 mm WD; Computar, Torrance, CA) focused at ~200 μm below the cortical surface. For each mouse over the time points, a sequence of 100 laser speckle images were captured at an exposure time of 6 ms (per our previous report on optimized LSI exposure time [7]) at a speed of 14 frames per second. The aperture and magnification of the zoom microscope were carefully chosen to ensure that the speckle size at the image plane was approximate to the area of a single pixel in the CMOS chip [21, 26, 30]. A schematic of the imaging system is shown in Figure 3.1(c).

The laser speckle contrast images were calculated using temporal statistical analysis of laser speckle images. Experimental results have indicated that temporal speckle contrast analysis could expressively suppress the effect of the static laser speckle pattern formed by the stationary superficial reflection and scattering tissue on the visualization of blood flow [21, 26, 30-32]. Suppressing static laser speckle preserves spatial resolution and makes temporal contrast analysis an ideal method for imaging cerebral blood flow through the skull and implant. The temporal contrast, K_t, of each image pixel in the time sequence was calculated using Equation (1),

$$K_t(x,y) = \frac{\sigma_{(x,y)}}{\left\langle I_{(x,y)} \right\rangle} = \sqrt{\frac{1}{(N-1)} \left\{ \sum_{n=1}^{N} \left[I_{(x,y)}(n) - \left\langle I_{(x,y)} \right\rangle \right]^2 \right\}} \Bigg/ \left\langle I_{(x,y)} \right\rangle \qquad (1)$$

where $I_{x,y}(n)$ is the CMOS counts at pixel (x,y) in the nth image, N is the number of images acquired, and $\langle I_{x,y} \rangle$ is the mean value of CMOS counts at pixel (x,y) over the N images.

The quality of each speckle contrast image was assessed in terms of SNR and sharpness of the imaged vessels. To quantify signal to noise ratio for each imaging condition, the contrast intensity profile along a vertical line (across the blood vessels) was considered. To avoid selection bias, the location of these line profiles were chosen arbitrarily at the ROI mid-points (red dashed lines in Figure 3.4(a)). The midlines intersected 3 to 4 vessels, and remained the same between the time points. Figure 3.4(b) shows an example of the contrast intensity profile at day 0, 14 and 28 for Mouse 1. Equation (2) shows how SNR values were calculated for each time point using the contrast images,

$$SNR = \Delta K \Big/ \sigma K_n \tag{2}$$

where ΔK is the depth of the vessel peak from the baseline (mean noise) and σK_n is the standard deviation of the noise. For each time point, the SNR values were averaged over the mice and standard errors were calculated.

We compared the sharpness of the vessel edges in contrast images by calculating fall distance (the number of pixels multiplied by the pixel size (~3 μm)) of the edge of the vessel to go from 10% to 90% of ΔK value [45]. A shorter fall distance corresponds to greater sharpness. Fall distance was calculated for vessel edges intersected by the same line profiles used in the SNR calculation (red dashed lines in Figure 3.4(a)). Figure 3.4(b) shows an example trace and 10–90% fall distance measurement.

Optical Coherence Tomography Imaging

Our initial investigation of the transparency of the nc-YSZ implant using OCT to image the brain of an acute murine model successfully demonstrated an increase in back-reflected intensity and subsequent improvement of OCT image SNR [6]. The same laboratory-

developed spectral-domain OCT (SD-OCT) system was used here to assess the chronic stability of image quality.

The core component of an OCT system is low coherence interferometry. The broadband laser light beam, typically in the near-infrared spectral range, is split into two optical paths, where there is a mirror at the end of one path and the sample at the end of the other. The interference pattern of the backscattered light from the two paths is measured, demodulated, and mathematically transformed into one line of depth-resolved image. By governing the position of the laser beam on sample, two-dimensional (2D) cross-sectional or three-dimensional (3D) volumetric images can be obtained. The spectral-domain OCT system used in this study utilizes a broadband laser light source with center wavelength of 1298 nm and 120 nm full-width at half maximum (FWHM). The total optical power from the source is 16 mW. The laser light is split between the reference arm and the sample arm at a beam splitter, and the returning light beams from each arm combine and interfere with each other resulting in coherent light. A diffraction grating at the detection portion of the system spreads the coherent light into spectral form and the spectrum is detected by a line scan camera (Sensors Unlimited, Princeton, NJ) with a line acquisition rate of 16.5 kHz. Each spectrum is converted to a spatial-domain depth-resolved A-line of image by applying inverse Fourier transform in post computational processing. Further details of the OCT system have been previously reported by [63].

For all OCT imaging in this study, the OCT beam incident on the sample was focused at approximately 0.8 mm in depth along the incident axis (10 μm spot size) by a cemented achromatic doublet lens with 30 mm focal length (Thorlabs Inc., Newton, NJ).

2D cross-sectional images or 3D volumetric images were obtained by lateral scanning of the beam across the sample. Each of the cross-sectional OCT images presented in this study contain 2048 A-lines in a physical transverse range of 7 mm (Figure 3.3(b)) or 3 mm (Figure 3.6), whereas 3D volumes for *en face* vascular angiography analysis are composed of 200 cross-sectional frames, covering a 3 mm by 3 mm square region (Figure 3.2(a), Figure 3.5). In the previous and current study, the lateral resolution was approximately 20 μm while the axial resolution was about 8 μm.

Real-time sample visualization and data acquisition was implemented by lab developed software with the aid of a graphics processing unit (GPU). Structural intensity images were processed and displayed in real time, allowing for rapid identification of the implant and location of the same region of the brain for all imaging sessions. The angle of incidence of the optical beam with respect to the WttB surface was fixed to ensure the consistency of results.

Cross-Sectional OCT Intensity Images

A cross-sectional OCT intensity image (Figure 3.3(b) and Figure 3.6) was formed by consecutive A-lines and displayed on a decibel scale. The blackness and whiteness represent the regions of high and low backscattered light intensity, respectively. Quantitative analysis of the light signal intensity (decibel scale) over image depth is presented in Figure 3.7. Averaged depth profiles were calculated by horizontally averaging 200 A-lines in the middle of the image that contains the information of WttB implant, cortex, and sub-cortical white matter (corpus callosum). The amount of signal level is a critical factor in the determination of image quality across the WttB implant. In our

previous study, we concluded that the WttB implant enhanced imaging performance because the signal strength was significantly higher when imaging through the implant [6]. Similarly, in the assessment of imaging performance through the implant over time, we compare the image signal intensity of the same murine brain model taken at different time points over 4 weeks.

OCT Angiography Images

The motion of dynamic particles, such as red blood cells in vessels, can be determined by extracting temporal and spatial statistical information from OCT data. The detected OCT signals contain the superposition of back-reflected components from static and dynamic scatterers, and OCT angiography techniques aim to screening out the dynamic scattering from static scattering for good visualization of vasculature and measurement of blood flow velocity [64-66]. Current OCT-based angiography techniques can be categorized into complex signal-based methods, phase-based methods and intensity-based methods [67, 68]. Most of these techniques rely on the calculation of variance, decorrelation or a combination of both. The scanning protocol of OCT angiography typically requires high line acquisition rate and repeated scanning on the same location over a certain amount of time to obtain angiographic images with high sensitivity, however, due to the limitation of scanning speed of our system and limited time allowed for imaging because of animal anesthesia status, we generated the angiography images by computing the phase variance of two adjacent complex depth profiles.

As presented in our previous research [63, 67-69], phase variance is determined by the phase difference ($\Delta\phi_n$) resulted from the comparison of the phases in one depth profile to those in the previous depth profile at corresponding depth (z_m), yielding

$$\Delta\phi_n(z_m) = \phi_n(z_m) - \phi_{n-1}(z_m) \tag{3}$$

where *n* is the depth profile index while *m* is the index of pixel in the depth profile. The minimal detectable phase difference ($\sigma_{\Delta\phi\text{min}}$) is rudimentarily limited by the SNR of a measurement, which can be expressed as

$$\sigma_{\Delta\phi\text{min}} = \frac{1}{\sqrt{SNR}} \tag{4}$$

where *SNR* is the harmonic mean of the signal-to-noise ratio of the depth profiles involved in that measurement. Consistent sampling of data at the same location is fundamental to ensure that the measured phase difference is purely caused by the motion of flow. A correction algorithm to reduce the phase instability due to the movement of scanning mirror is included in the flow image processing [70]. Therefore, with the correction of overall phase shift between depth profiles, the phase variance can be calculated as

$$\sigma_{\Delta\phi}{}^2(z_m) = \left(\Delta\phi_n(z_m) - \frac{\sum_{z_m}\Delta\phi_n(z_m)\cdot SNR\Delta\phi_n(z_m)}{\sum_{z_m} SNR\Delta\phi_n(z_m)}\right)^2 \tag{5}$$

Spatial two-dimensional mean filter was applied to cross-sectional phase variance images to reduce the phase variance from arbitrary speckle noise. *En face* vasculature angiography was generated based on a depth range of 200 pixels (~ 1 mm) of subsurface cortex region below the window implant.

The 3D visualization of a wide view of the brain with WttB implant (Figure 3.2(b)) was constructed from a volumetric OCT imaging dataset with 800 frames and 4096 A-lines

per frame. The same filtering strategy was applied to each frame of phase variance image and the depth of each blood vessel was determined by the measurement of phase variance along corresponding A-lines. For better visualization of the high-scattering brain structure, such as corpus callosum, we utilized the calculation of depth-resolved attenuation coefficient as described in [71]. The processed sets of phase variance images and attenuation coefficient images were imported to Amira (Thermo Fisher Scientific and Zuse Institute Berlin) for 3D rendering.

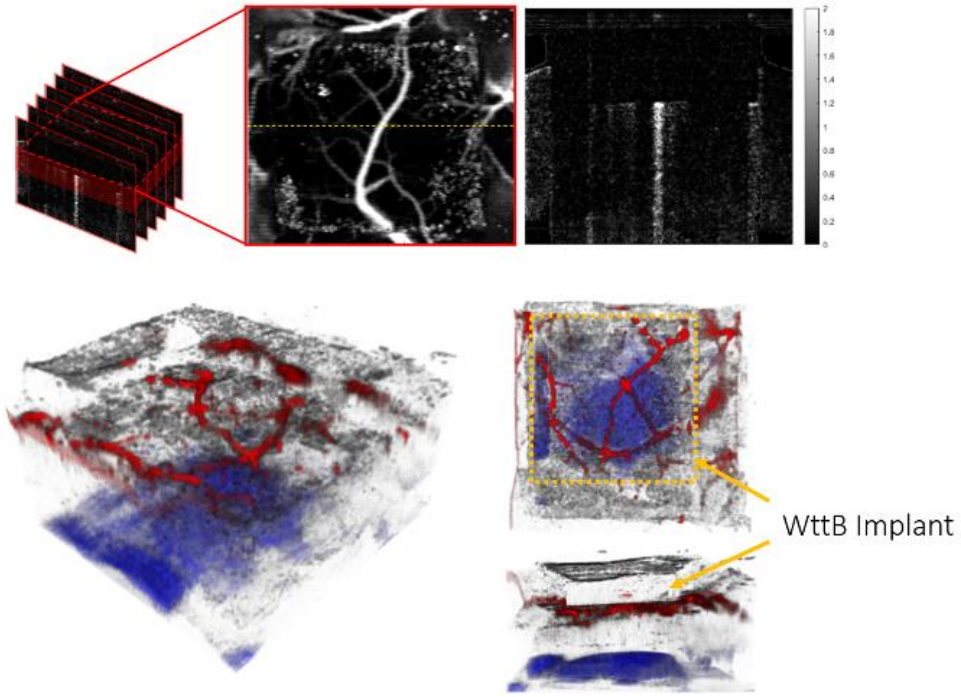

Figure 3.2: Schematic for volumetric and *en face* OCT visualization: a) Volumetric flow information was constructed from 200 cross-sectional frames 2 mm in depth, covering a 3 mm by 3 mm square region laterally across the surface of the brain. As the majority of visible vessels occur within 0.4 mm beneath the lower surface of the WttB implant, only this depth range was used to create an *en face* view. The image on the right side is one example of cross-sectional flow image located at the yellow dashed line on the *en face* flow image (unit of the color bar: rad). b) 3D visualization of OCT image of brain with WttB implant. Cerebral vasculature is colored in red and the corpus callosum, as identified through depth-resolved attenuation [71], is colored in blue. The upper and lower surfaces of the implant are visible, and can be contrasted with surrounding regions of native skull.

Results

Figure 3.3(a) and 3.3(b) provide LSI and OCT images with a wide field of view covering both sides of the head, to allow for visual comparison of brain vasculature and structural imaging, respectively, through the WttB implant vs. the skull. Figure 3.3(c) shows the near-infrared collimated transmittance spectra of the implant vs the mouse skull, including the wavelengths used for LSI (810 nm) and OCT (1238-1358 nm) imaging.

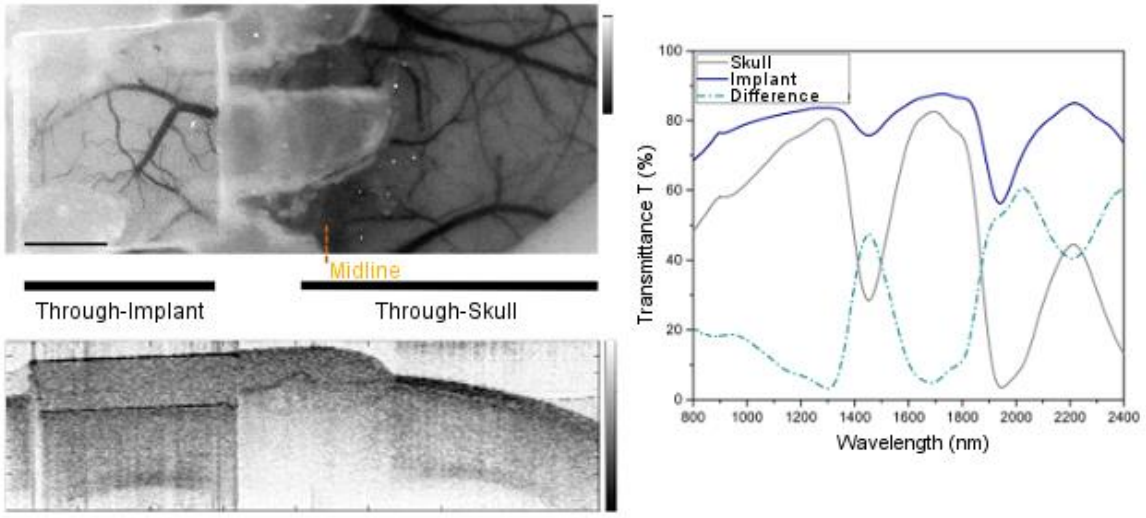

Figure 3.3: Comparison of imaging through WttB implant vs native mouse skull. a) LSI image of mouse cerebral vasculature with WttB implant, b) OCT image of mouse cranium with WttB implant, c) collimated transmittance spectra of the implant and mouse skull, showing the higher transparency of the implant compared to mouse skull.

Figure 3.4(a) shows the LSI images of cerebral blood flow for each of the 5 mice at the 3 time points of this study. The images are displayed as color maps, where higher relative velocity within the image (i.e., regions with blood flow) appear red and lower relative velocity within the images (i.e., static regions of tissue) appear blue. Figure 3.4(a) also includes regular white light images of Mouse 1. For all LSI images, line intensity profiles were taken at the midpoint of the implant (illustrated as red dashed lines in the regular

white light images) for quantitative analysis. Figure 3.4(b) shows the line intensity profiles for Mouse 1 at the 3 time points, which allowed for identification of vessels intersected by the line profile which appear as valleys in the intensity profile. The line profiles further allowed for determination of SNR, and fall distance of the vessel edges (see inset). Mean SNR and fall distance for the 5 mice are provided for each time point in Figure 3.4(c) and 4(D), respectively (error bars represent standard error).

LSI alone was not sufficient to answer the question of whether optical access provided by the WttB implant remains stable, as blood flow does not remain constant over time and differences found between the imaging time points could be due to physiologic changes such as hyperemia, changes in the optical access, or a combination of both. To answer this question, we used OCT imaging, and processed the data to render *en face* flow images (which provide similar information to LSI), and cross-sectional intensity images (which provide structural information on tissue and should remain stable over time). Figure 3.5 presents the OCT *en face* flow images for the 5 mice at the 3 imaging time points, and is in general agreement with the LSI images, showing higher flow at Day 0 compared to the later time points.

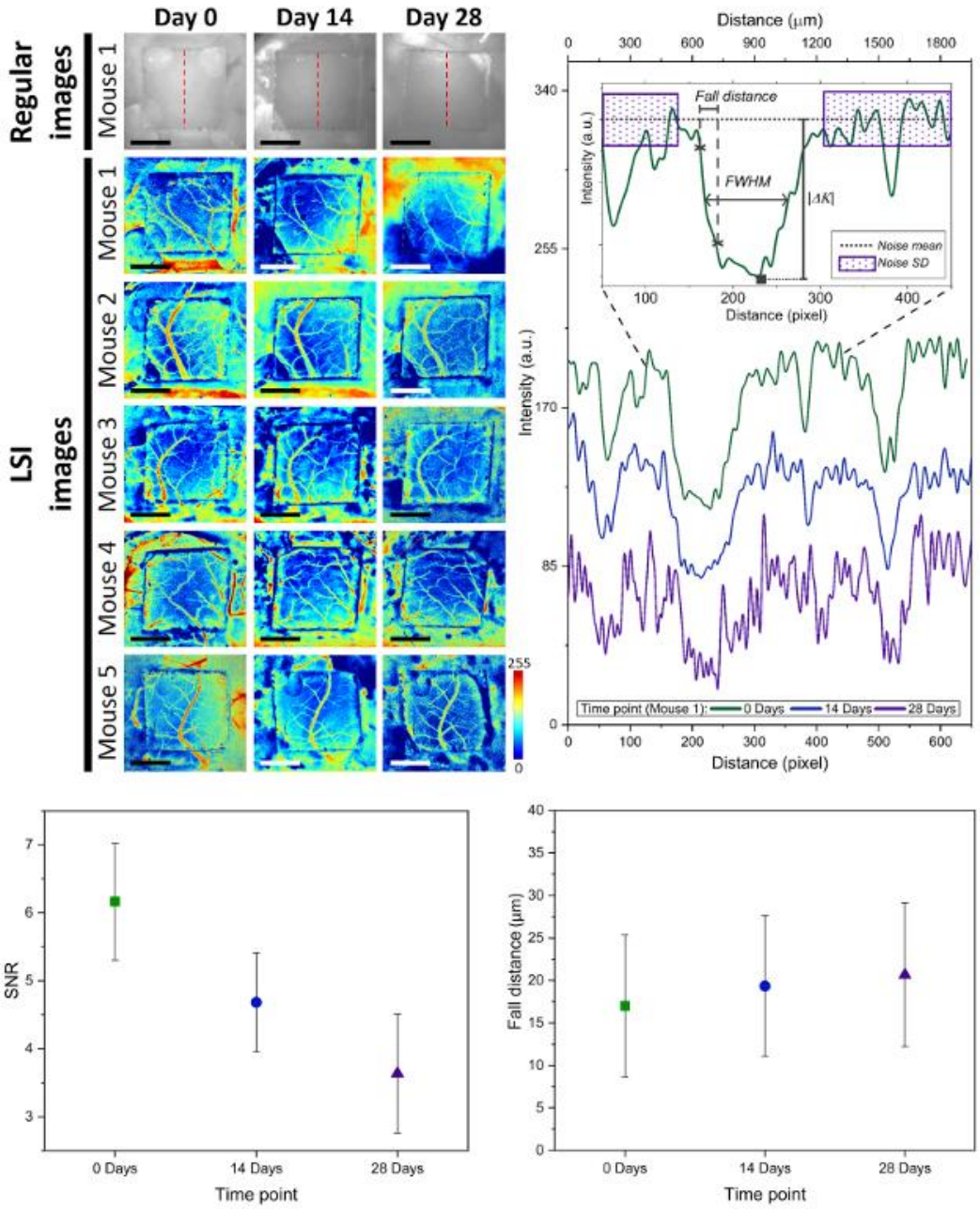

Figure 3.4: a) Comparison of LSI images between Day 0, Day 14, and Day 28 for the n = 5 mice, as well as regular white light images of Mouse 1. The red dashed lines show where line profiles were taken at the midline of the WttB implant. b) Analysis of line profiles from Mouse 1, showing decreasing intensity at days 14 and 28 compared to Day 0. The inset depicts how noise mean and standard deviation was measured, as well as fall distance and FWHM of vessels intersected by the line profiles. c) Mean SNR for the 5 mice decreased at later time points compared to Day 0. d) Fall distance of vessel edges increased at later time points compared to Day 0, indicating a reduction in the image sharpness at these later time points.

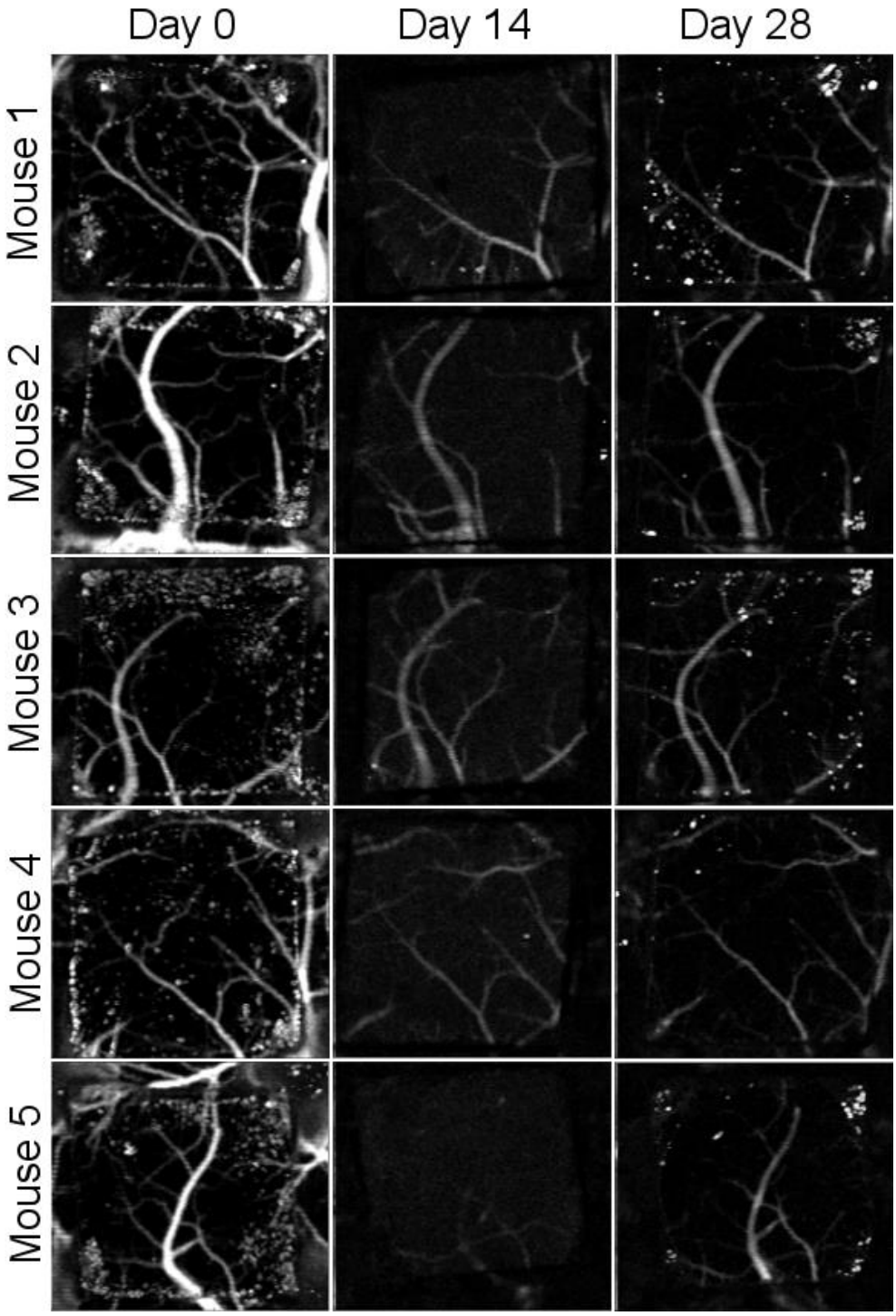

Figure 3.5: Comparison of *en face* OCT flow images between Day 0, Day 14, and Day 28 for the n = 5 mice. Flow appears higher at Day 0 than at later time points.

Cross-sectional OCT intensity images are shown in Figure 3.6 for the five mice across the three time points. All OCT images were acquired to position in the WttB implant within the same depth range to minimize the effect of depth-dependent OCT sensitivity between imaging sessions. The images were further normalized by the average intensity from within the interior of the WttB implant to further reduce the effects of slight variations in experimental acquisition between imaging sessions, such as the angle of incidence with respect to the implant surface. Normalized intensity depth profiles for each mouse at each time point are provided in Figure 3.7. The degree of overlap between these depth profiles provides quantitative verification of the longitudinal stability of OCT imaging through the WttB implant over the 28 day period.

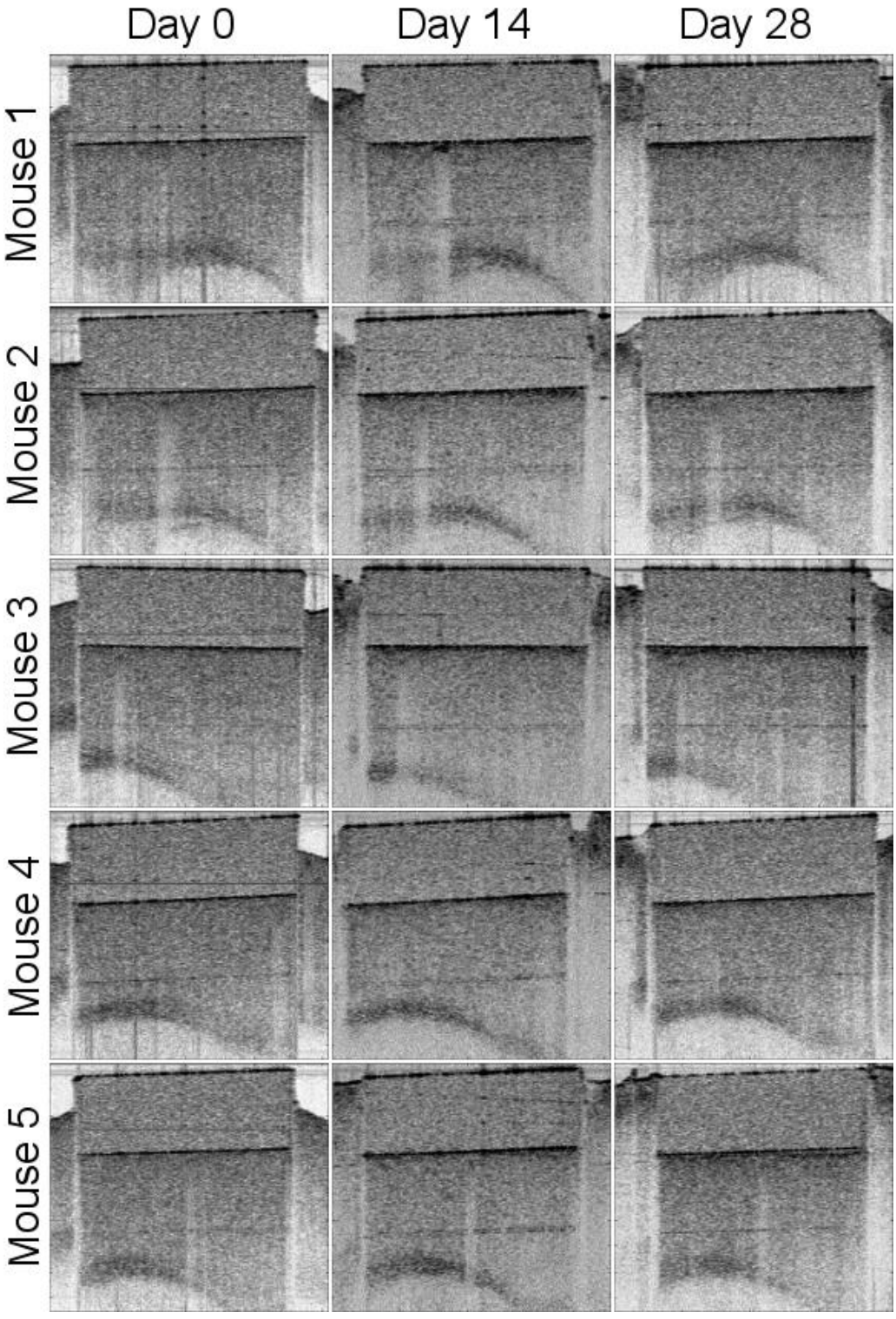

Figure 3.6: Comparison of cross-sectional OCT intensity images between Day 0, Day 14, and Day 28 for the n = 5 mice.

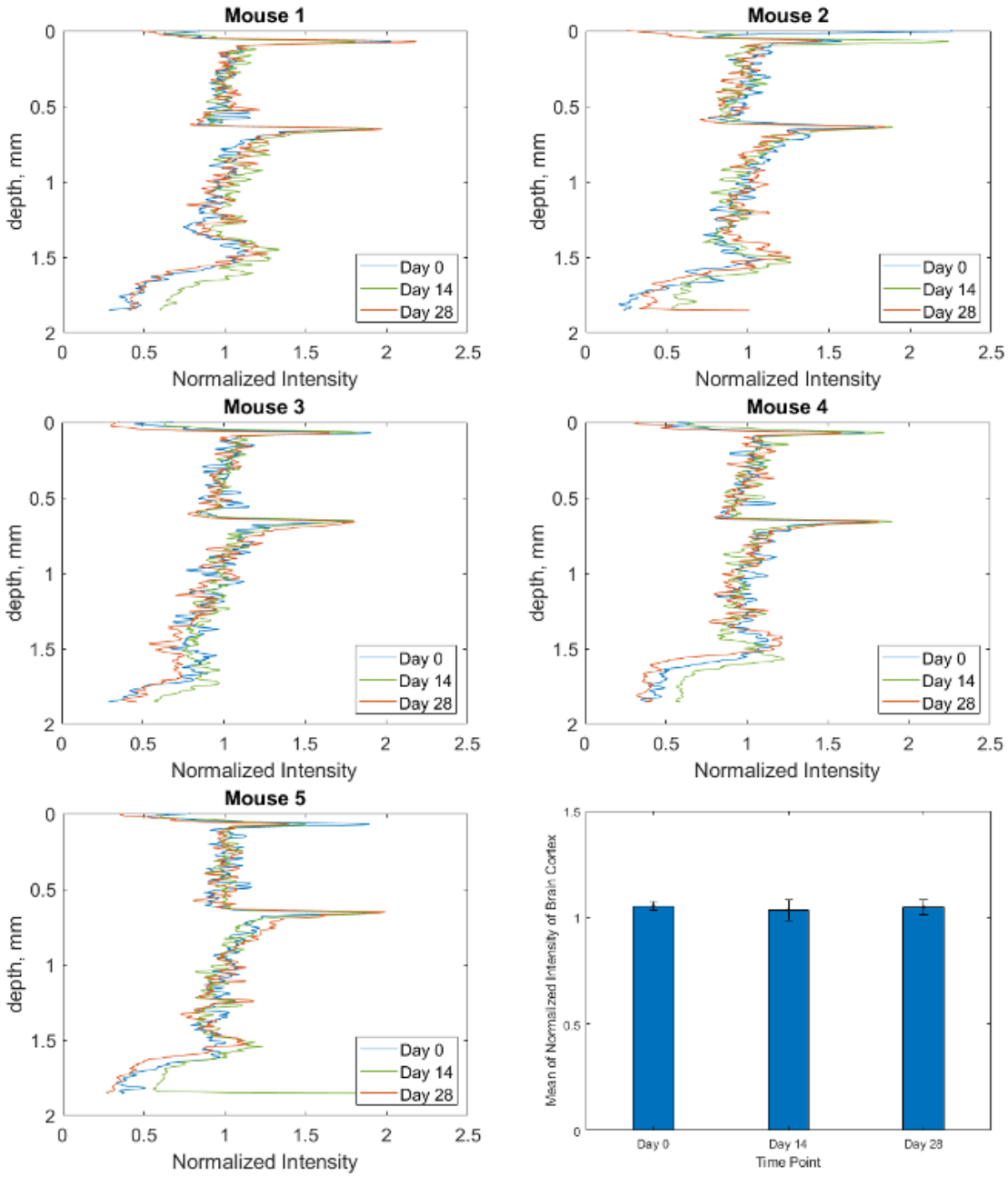

Figure 3.7: a-e) Intensity depth profiles for each of the n = 5 mice at each time point, showing that attenuation is not increasing over the 28 days. f) Bar graph showing mean of normalized intensity of brain cortex for all 5 mice at each time point.

Following the final imaging time point on Day 28, mice were sacrificed and histology was performed on the brain via H&E staining. Cross-sectional sections of the brain beneath the

craniectomy showed no signs of inflammation or histological damage. An example from Mouse 1 is provided in Figure 3.8.

Figure 3.8: Mouse 1 histology. a) Craniectomy with implant removed following euthanasia. b) Brain with skull removed. c) H&E stain of brain section from beneath the implant, showing no signs of inflammation.

Discussion

Consistent with our previous studies [6, 7], imaging through the WttB implant with LSI and OCT resulted in higher contrast than imaging through the mouse skull (Figure 3.3(a) and 3.3(b), respectively). Collimated transmittance spectra for the skull and WttB implant are provided in Figure 3.3(c), and show that transmittance is higher through WttB implant than skull for all wavelengths measured, including 810 nm (LSI wavelength) and 1298 nm (OCT central wavelength). It should be noted that although the difference in transparency between the implant and mouse skull is modest for some wavelengths, the mouse skull is inherently transparent [26], which is not the case for human skull where the difference between implant and skull transmittance will be larger.

In our previous study (Chapter 2) [7], LSI imaging of cerebral blood flow across the WttB implant did not remain constant over the 4 weeks. SNR and sharpness of the imaged vessels were found to be decreased at Day 14 and Day 28 compared Day 0. Visually, the vessels appeared to have smaller diameters and lower relative blood flow

velocity at these later time points. The data presented in this prior chapter came from 3 of the 5 mice presented in this present chapter, from data acquired at these same imaging sessions. Figure 3.4 includes data from these mice along with 2 additional mice, which show the same trend of decreased SNR and sharpness of imaged vessels at later time points compared to Day 0 imaging. In the previous study, we were unable to answer whether the optical access provided by the WttB implant was degrading over time, or whether the blood flow was different at the different imaging time points. We speculated that the change we observed was primarily due to changing blood flow and not to a change in the optical access, and that blood flow was elevated above normal levels on Day 0 due to the craniectomy surgery. This phenomenon of elevated blood flow in response to tissue trauma is known as reactive hyperemia [47]. In this present study, the inclusion of OCT imaging provides us with additional information to answer this question. First, we sought to assess blood flow between the time points using OCT to see if it was in agreement with the LSI. As shown in Figures 3.4 and 3.5, the OCT is in general agreement with the LSI, showing the vessels to be of larger diameter at Day 0, and with higher flow velocity, indicating that blood flow is indeed higher at Day 0 compared to Days 14 and 28.

To answer the question of whether the optical access to the brain provided by the WttB implant remains stable over time, we compared OCT intensity images between the 3 time points for each mouse. As shown in Figure 3.6, the images appear very similar over the 4 weeks of implantation. As shown in Figure 3.7, the intensity profiles of brain tissue imaged through the implant overlap and do not show any consistent trend towards faster

intensity drop-off with depth between the time points, indicating that the attenuation of light collected through the implant is not increasing over the 4 weeks of this study.

Together, these data suggest that the WttB implant provides stable optical access to the underlying tissue, at least for the wavelengths assessed by OCT (1238-1358 nm). The changes we found in this study and our previous LSI study regarding vessel diameter and relative flow velocity are likely actual changes in the blood flow and not imaging artifacts, as supported by OCT when processed for *en face* flow information. The blood flow appears to be elevated at Day 0 (following the craniectomy), and this change is no longer present by Day 14, where the flow is much closer to Day 28 blood flow. The histology of brain slices taken beneath the implant (Figure 3.8) further support this interpretation of the data, showing no signs of inflammation or structural damage to the surface of the cortex.

Conclusion

The Window to the Brain implant allowed for stable repeated imaging of the mouse brain with Optical Coherence Tomography over 28 days, without loss of signal intensity. Repeated Laser Speckle Imaging was also possible over this timeframe, but signal to noise ratio and the sharpness of vessels in the images decreased with time. This can be partially explained by elevated blood flow during the first imaging session in response to trauma from the surgery, which was also detected by OCT flow imaging. These results are promising for long-term optical access through the WttB implant, making feasible chronic *in vivo* studies in multiple neurological models of brain disease.

Citation: The work presented in this chapter was published in *Frontiers in Bioengineering and Biomedicine* [8]:

Halaney DL, Jonak CR, Liu J, Davoodzadeh N, Cano-Velázquez MS, Ehtiyatkar P, Park H, Binder DK, Aguilar G. Chronic brain imaging across a transparent nanocrystalline yttria-stabilized-zirconia cranial implant. *Fronteirs in Bioengineering and Biomedicine* 8:659 (2020).

Acknowledgments

I would like to acknowledge the contribution of my co-authors to this work: Carrie R. Jonak, Junze Liu, Nami Davoodzadeh, Mildred S. Cano-Velázquez, Pasha Ehtiyatkar, Hyle Park, Devin K. Binder, and Guillermo Aguilar. This work was supported by National Science Foundation (NSF-PIRE) (1545852). The authors acknowledge Gottlieb Uahengo for providing the nc-YSZ samples used in this study.

Chapter 4. Optical Access to Arteriovenous Cerebral Microcirculation Through a Transparent Cranial Implant

Background

Microcirculation, usually defined as small arteries (<150 μm in diameter), arterioles, capillaries, and venules [72, 73], plays a critical role in the physiological processes of tissue oxygenation and nutrient exchange within the brain [74, 75]. In recent years, the recognition that microcirculation is also involved in a number of pathophysiologic processes has further increased interest in its study [74]. Microcirculation can be measured in several ways, including (but not limited to) morphological imaging methods to measure vessel density, perfusion rate, vessel diameter, and dynamic measurements of microcirculatory blood flow velocity and blood cell concentration [74], as well as functional imaging methods to provide information on blood oxygenation, changes in metabolism, regional chemical composition, and so on [76].

Various imaging modalities have been developed, which are capable of measuring blood flow. Although they have resulted in a number of discoveries, there are notable drawbacks which should be considered in developing a scalable and real-time method for routine long-term brain microcirculation monitoring. Magnetic resonance imaging (MRI) and blood-oxygenation-level-dependent MRI [77, 78] are very expensive and large imaging tools [79]. Dynamic contrast enhanced computed tomography (CT) and micro-CT [80, 81] have a lower resolution than MRI and rely on ionizing radiation making it infeasible for monitoring [79]. Digital subtraction angiography (DSA) is an invasive and time-consuming method [82, 83]. Indocyanine green video angiography requires injection

of dyes and cannot provide continuous assessment of vessel perfusion [84, 85]. Optical coherence tomography (OCT) [86], photoacoustic imaging (PAM) [87], and fluorescence microscopy approaches like confocal microscopy or the two-photon variant [88] are based on laser scanning limiting the temporal resolution and field of view [89], although recent technical improvements in OCT and PAM have been reported, which provide sufficient temporal resolution for epileptic seizure monitoring [90-92]. Ultrasound (US) and micro-US [93] imaging depth is larger than light-based approaches, however, the resolution is poorer [94]. Fast full-field laser Doppler perfusion imaging (ffLDPI) [88] cannot simultaneously provide microvascular structural and functional information because of lacking adequate spatiotemporal resolution [95].

Laser speckle imaging (LSI), on the other hand, is a full-field, real-time, noninvasive, and non-contact imaging method with is sensitive to both the speed and morphological changes of the scattering particles, and is capable of mapping relative velocity in flow fields such as capillary blood flow [88]. LSI produces blood flow maps in a fraction of a second without the need for scanning, by utilizing the spatial statistics of time-integrated speckle, making it a true real-time technique [88]. Like LSI, ffLDPI can provide full field information in a short time and may be regarded as its main competing technique, but LSI has the advantage of being relatively simple and cheap since it does not require a high-speed imaging array, and can also be coupled with other imaging modalities [88].

In addition to information on vessel geometry and flow characteristics, distinction between arteries and veins is of great clinical importance. The ability to independently

render veins and arteries on blood perfusion maps has a variety of potential applications in the head, neck, lungs, heart, abdomen, and lower extremities, and most critically in the cerebrovascular system including brain arteriovenous malformation and dural arteriovenous fistulas [96], cerebral hemorrhage, stroke, and aneurysm [97].

Multispectral reflectance imaging (MSRI) is a simple and low-cost method capable of distinguishing between veins and arteries based on differences in the optical absorption of oxyhemoglobin and deoxyhemoglobin. This method has been developed in visible and near-infrared (NIR) wavelength range [98-105]. This method involves a white light source, optical filters, and a camera, and can easily be coupled with LSI [97, 102, 106]. Indeed, a single instrument combining laser speckle flowmetry and MSRI has been demonstrated in a rodent thinned skull model [99] for simultaneous relative cerebral blood flow and hemoglobin oxygen saturation changes during ischemia [102, 107, 108] and functional activation [109]. A thinned skull preparation was necessary due to the high scattering and absorption of the skull in the visible and NIR range, which limits the accessibility of MSRI wavelengths for detecting hemoglobin oxygenation information [110, 111]. When MSRI has been applied through the intact skull, only skull regions and not individual microvessels are visible [6, 111]. Likewise, in our own prior studies we have found that imaging through intact skull with LSI limits the size of vessels that can be detected, and precludes imaging of the microcirculation [7, 44]. Moreover, the absorption and reflectance features of the inhomogeneous cranial bone overlap with those of brain tissue, and the skull also has its own vessels. Together, these factors decrease the accuracy and reliability of the data.

Studies in the literature have addressed this optical barrier with various approaches including imaging the brain directly with an opened skull [106], thinned, and polished skull preparations [27, 112], temporary optical clearing of the skull using optical clearing agents [29, 113, 114], and implanting glass or poly-di-methyl-siloxane (PDMS) windows [4, 115]. Glass and PDMS windows are powerful research techniques, but are not appropriate for human application as permanent cranial implants for patients. Like skull thinning and polishing techniques, glass-based windows compromise protection for the brain due to the extremely low fracture toughness of typical glasses (K_{IC} = 0.7–0.9MPa · $m^{1/2}$) [35], which increases the potential for catastrophic failure by fracture, while the effect of skull optical clearing agents for long-term use on human skull is unknown [7]. A number of biomedical considerations including biocompatibility, mechanical strength, and ageing should be examined in order to create an optical window for eventual clinical application [7]. Conventional cranial prosthesis including titanium, alumina, and acrylic [36] have not provided the requisite combination of transparency and toughness required for clinically-viable transparent cranial implants. To address this challenge, our group has previously introduced a transparent nanocrystalline yttria-stabilized-zirconia cranial implant material, which possesses the mechanical strength and biocompatibility that are prerequisites for a clinically-viable permanent cranial implant for patients [6, 7, 43, 61, 116]. We refer to this in the literature as the "Window to the Brain" (WttB) implant. Yttria-stabilized zirconia (YSZ) represents an attractive alternative, due to its relatively high toughness (K_{IC} ~ 8 MPa · $m^{1/2}$) [39], as well as its proven biocompatibility in dental and orthopedic applications [117]. Additional benefits of this material over imaging through skull include its stable

optical behavior and lack of optical absorption by water (Figure 4.1(c)). We envision this implant as a potential future optical access to the brain allowing for real-time monitoring of arteriovenous cerebral blood flow (Figure 4.1).

In this chapter, we performed cerebral arteriovenous microcirculation imaging by combining MSRI and LSI techniques. This method was applied in a mouse model, first through the closed skull, then to the dura mater and brain directly after a craniectomy was performed to remove a piece of skull, and finally through the WttB implant after the implant was placed within the craniectomy on the dura mater. The imaging obtained through the WttB implant and through the skull were compared to the imaging obtained through the open skull, which served as a reference. The goal of this study was to assess the improvement in brain imaging with MSRI-LSI when captured through the WttB implant versus imaging through the skull.

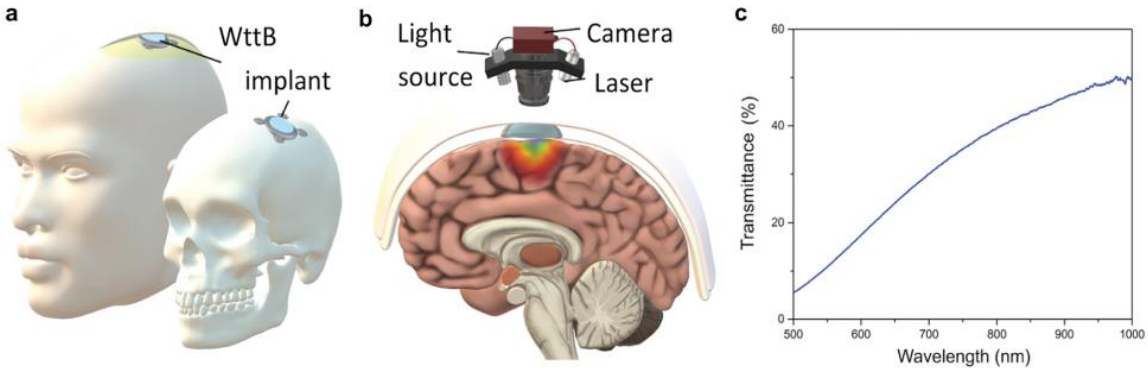

Figure 4.1. (a, b) Illustration of the Window to the Brain concept as envisioned for future human application, to allow for real-time monitoring of arteriovenous cerebral blood flow. (c) Transmittance spectra of Window to the Brain implant.

Methods

Transparent Stabilized-Zirconia Cranial Implant

Implant fabrication and preparation was conducted as described in Chapter 2 (page 8). Optical transmittance spectra for the polished implant is shown in Figure 4.1(c).

Animals

All experimental procedures and humane care of mice were conducted in compliance with the University of California, Riverside Institutional Animal Care and Use Committee approval. The n = 1 12-week-old C57Bl/6 male mouse (Jackson Laboratory, Bar Harbor, ME) used in this study was housed under a 12-hour light and 12-hour dark cycle with *ad libitum* access to food and water.

Surgical Procedures

The mouse was implanted with a WttB implant as described in Chapter 2 (page 9). Hair was removed from the scalp using clippers (Figure 4.2(a)), followed by a sagittal incision to the left of the midline and scalp retraction to expose the skull (Figure 4.2(b)). Periosteum was removed from the skull, and a craniectomy was performed with a surgical drill and carbide burr to remove a square section of skull over the right parietal lobe, with dimensions slightly larger than the implant (Figure 4.2(c)). The WttB implant was placed within the craniectomy directly on the intact dura mater, and dental cement was applied to each of the four corners of the implant to prevent displacement (Figure 4.2(d)). Dental cement was cured with UV light exposure for 20 seconds. Imaging was conducted with the scalp open, before craniectomy with the skull closed (condition 1), immediately after craniectomy with the skull open (condition 2), and after WttB implantation (condition 3).

MSRI and LSI

MSRI was performed by optically filtering a white-light source (MI-150; Dolan-Jenner, Boxborough, MA). Optical bandpass filters mounted on a fast-change filter wheel (FW103H; Thorlabs, Newton, NJ) were used to isolate different spectral components and

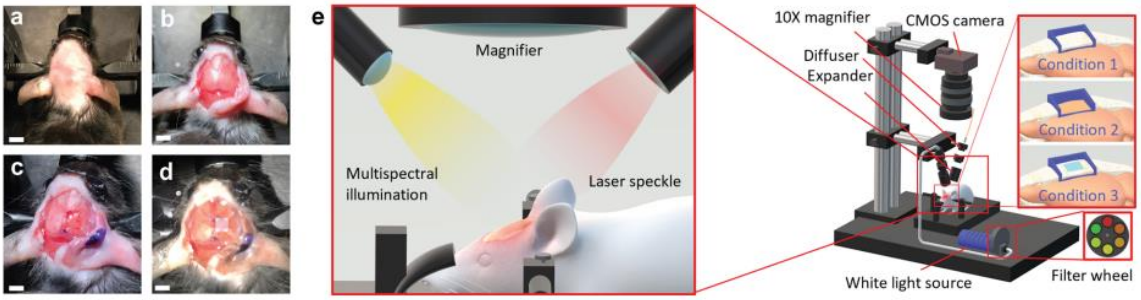

Figure 4.2. a–d) Surgical preparations including a) shaved scalp (scale bars = 2 mm), b) intact skull (i.e., condition 1), c) open skull (i.e., condition 2), d) and WttB implant (i.e., condition 3). e) Schematic of the experimental imaging setup including laser speckle imaging (LSI) and multispectral reflectance imaging (MSRI). The inset shows a schematic of the imaging fields of view on murine cranium, with the blue tetragonals representing the imaging field.

provided a six-wavelength (560, 570, 580, 590, 600, and 610 nm) multispectral dataset, as shown in Figure 4.2(e). For LSI, an 810 nm continuous wave NIR laser (DL808-7W0-O; CrystaLaser, Reno, NV) was used to illuminate the region of interest with incident power of 100 mW at a 45° incidence. While most LSI studies use visible wavelengths for illumination, we chose 810 nm to reduce reflectance and increase transmittance through the WttB implant (see Figure 4.1(c)). The 810nm laser intensity was homogenized using a diffuser (ED1-C20-MD; Thorlabs) and was expanded using a pair of negative-positive lenses (KPC043, −25mm EFL and KPX094, 100mm EFL; Newport, Irvine, CA). Multispectral incoherent light and diffused laser light were sequentially shown onto the closed skull (i.e., condition 1), onto the dura mater and cortex after craniectomy (i.e., condition 2) and through the WttB implant (i.e., condition 3). The reflected light from the illuminated region was captured by a 12-bit complementary metal-oxide semiconductor (CMOS) camera (DCC1545M; Thorlabs), which was focused at the cortical surface using a 10x zoom microscope (MLH-10X, 152.4 mm WD; Computar, Torrance, CA). For each imaging condition, a sequence of six multispectral images and 100 laser speckle images

were captured. Laser speckle images were acquired at exposure times of 6ms (per our previous report on optimized LSI exposure time [7]) at a speed of 14 frames per second. The aperture and magnification of the zoom microscope were carefully chosen to ensure that the speckle size at the image plane was approximate to the area of a single pixel in the CMOS chip [21, 26, 30]. A schematic of the imaging system is shown in Figure 4.2(e). In image processing, each camera frame was registered to one another to ensure appropriate spatial alignment over the MSRI and LSI Images. In MSRI, normalizing each individual wavelength to its corresponding white reference (WS-1; Ocean Optics, Oxford, UK) image compensated for variations in the illumination. The white reference images were captured through the WttB implant in condition 3.

Vein-Artery Separation Using MSRI

The MSRI approach relies on the distinctive absorption spectra of oxy- and deoxyhemoglobin (HbO_2 and HbR). The hemoglobin in blood is the most significant absorber in the brain at visible and NIR wavelengths. HbR and HbO_2 have different absorption spectra, and thus based on the Beer-Lambert law [118], measurements with different wavelengths of light can produce images that are preferentially sensitive to difference in the concentration of HbO_2 and HbR. At isobestic points, the HbR and HbO_2 optical extinction coefficient are similar (568 and 587 nm). At 560, 600, and 610 nm, areas with higher level of deoxyhemoglobin C (e.g., the veins) leads to more optical extinction and thus makes the corresponding area darker (i.e., lower intensity values in the images), and therefore we can provide artery-vein separation. In this case, we assume that scattering in the brain does not change significantly during the experiment. To separate the vein and

arteries in MSRI images, the vasculature branches were detected and mapped manually for seven branches in regular white-light images (Figure 4.3(a)). Each vasculature branch was labeled by a number. To obtain the mean intensity of a branch, 10 samples of intensity (4 × 4 pixels) were extracted and averaged from each branch and called vessel branch intensity. The sample intensities of each branch were evenly distributed along the midline of the main vessel of the branch (Figure 4.3(a)). The samples locations were kept constant for each vasculature branch over the multispectral images. Then, normalized extinction was obtained over the wavelengths by calculating the difference in intensities of the white reference and the vessel branch, normalized by white reference intensity following Equation (1),

$$\text{Normalized extinction} = \frac{I_{n,\lambda} - I_{R,\lambda}}{I_{R,\lambda}} \quad (1)$$

where $I_{n,\lambda}$ is vessel branch number n, intensity at λ wavelength, and $I_{R,\lambda}$ is the mean value of the white reference intensity at λ wavelength.

Rebuilding Arteriovenous Cerebral Blood Flowmetry Map Based on MSRI-LSI

Step 1: Constructing a blood flow map using laser speckle temporal contrast analysis (LSTCA)

The contrast-resolved LSI images were constructed in the same manner as our prior study [7], based on the temporal statistical analysis of laser speckle, which has been proven to preserve spatial resolution [26]. Experimental results have indicated that the temporal speckle contrast analysis could expressively suppress the effect of the static laser speckle pattern formed by the stationary superficial reflection and scattering tissue on the

visualization of blood flow [21, 26, 30-32]. Suppressing this effect makes temporal contrast analysis an ideal method for imaging cerebral blood flow through mouse skull and the transparent WttB implant. The temporal contrast, K_t, of each image pixel in the time sequence was calculated using Equation (2) [21],

$$K_t(x, y) = \frac{\sigma_{(x,y)}}{\langle I_{(x,y)} \rangle} = \sqrt{\frac{1}{(N-1)} \left\{ \sum_{n=1}^{N} [I_{(x,y)}(n) - \langle I_{(x,y)} \rangle]^2) \right\}} / \langle I_{(x,y)} \rangle \quad (2)$$

where $I_{x,y}(n)$ is the intensity at pixel (x,y) in the nth image, N is the number of images acquired, and $\langle I_{x,y} \rangle$ is the mean value of intensity at pixel (x,y) over the N images.

Step 2: Arteriovenous vasculature network

The vasculature network was extracted from the LSI image according to the difference in flow velocity between the vasculature and tissue. A Hessian-based filtering algorithm was then used to enhance contrast and connectivity in the image of the vasculature [119-121]. In this step, vessels are detected using the eigenvalues of the image [120], and detection is sensitive to vessels in any orientation. Vessel detection was performed over multiple vessel scales (from ~20 to 400 μm in diameter), and the maximum filter response for each pixel was used. The resulting image was thresholded to produce a binary mask of the vasculature. The arteriovenous information obtained by MSRI was then registered on the vasculature network obtained by LSI, and veins and arteries were labeled on the vasculature network LSI images.

Step 3: Weighting the arteriovenous vasculature network by the blood flow map

Finally, the resulted arteriovenous vasculature network was weighted by the calculated LSTCA relative blood flow information.

Quantitative Analysis of the LSI Resolution and Contrast

We assessed the quality of the speckle contrast images in terms of signal to noise ratio (SNR) and vessel sharpness. To quantify signal to noise ratio for each imaging condition, the contrast intensity profile along a vertical line (across the blood vessels) was considered (Figure 4.3(b)). The profile lines were chosen based on the open-skull images such that four vessels were intersected. The same spatial location (i.e., same vessels) were analyzed in the through-skull and through-implant conditions as well. When imaging through skull, one of the four vessels was not visible and was omitted from the analysis of that condition. Figure 4.3(c) shows an example of the contrast intensity profile for the brain with open skull, through-skull, and through-implant. Equation (3) shows how SNR values were calculated for each exposure time and time point,

$$\mathrm{SNR} = \Delta K/\sigma K_n \tag{3}$$

where ΔK is the depth of the vessel peak from the baseline (mean noise) and σK_n is the standard deviation of the noise. A visual example of ΔK and σK_n are shown in Figure 4.3. The SNR values were averaged over the profile vessels and standard errors were calculated. Sensitivity, which is considered as the ratio of the mean SNR to the mean SNR of the reference, was calculated using Equation (4).

$$\mathrm{Sensitivity} = \frac{\mathrm{SNR}_{\text{imaging condition } n}}{\mathrm{SNR}_{\text{imaging condition 2}}} \tag{4}$$

As an indicator of resolution, we compared the sharpness of the vessel edges in images by calculating the fall distance (the number of pixels) of the edge of the vessel to go from 10% to 90% of ΔK value [45]. A shorter fall distance corresponds to greater sharpness. The same sampled contrast intensity profiles were considered for the fall distance calculation. Figure 4.3(c) shows an example trace and 10–90% fall distance measurement. To compare the blood vessel images through-skull and through-implant, the fall distances were determined and averaged over the profile vessels and the standard errors were calculated.

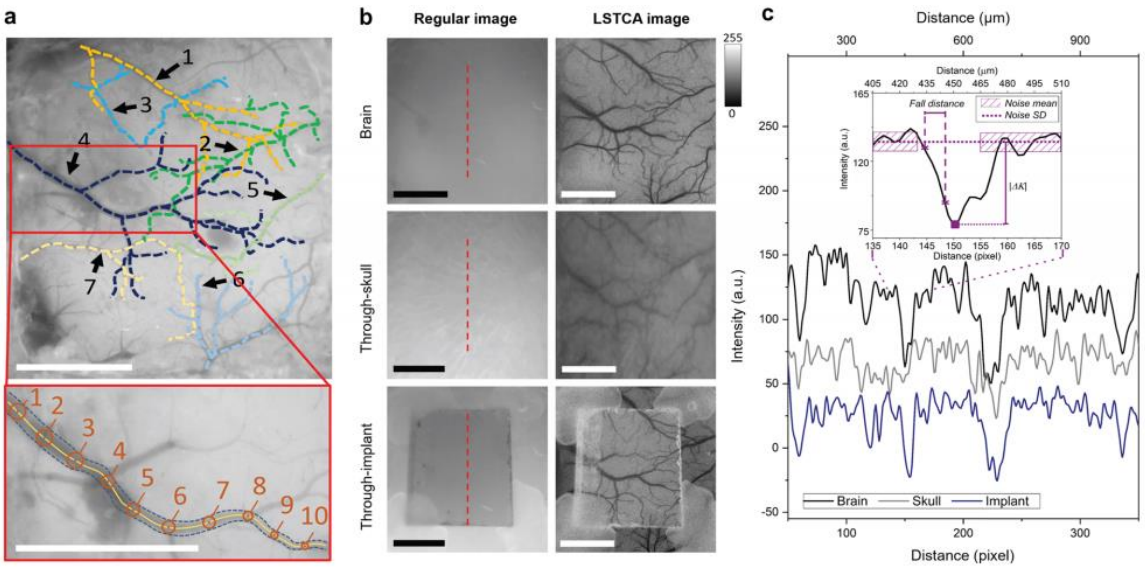

Figure 4.3. a) Vessels branches of 1–7 indicated by different colors on a regular white-light image of the brain image through the open skull (condition 2). The inset shows an example of evenly distributed intensity samples along the midline of the main vessel of the branch 4, which were used to calculate the vessel branch intensity. b) Regular white-light images and laser speckle imaging (LSI) images (scale bars = 1 mm). c) Contrast intensity profiles of lines across the images (shown as a dashed line in panel a). The inset in c) shows how LSI noise parameters, $|\Delta K|$ and fall distances are determined from the line profiles.

Results

MSRI Images of the Brain: Comparison of Through-Skull and Through-Implant Images

The mapped vasculature branches and vein-artery separated network from open-skull imaging (i.e., condition 2) are shown in Figure 4.4(a) and (b), respectively. Figure 4.4(d) shows the spectral behavior of the branches. The dashed line in Figure 4.4(d) shows the mean optical extinction of all seven branches. Overall, optical extinction is relatively high for wavelengths of 560–580 nm. A drastic decrease in optical extinction happens at wavelengths of 590, 600, and 610 nm. Notably, the vessel branches 1 and 4 show a different trend compared to branches 2, 3, 5, 6, and 7. These two groups were labeled in red and blue and the mean (solid lines) and standard deviation (colored shadow) of each group were separately calculated and shown. The blue group including branches 1 and 4 resulted in higher optical extinction at 560 nm. At wavelengths of 570 and 580 nm, red group showed the extremum values. Optical extinction values of red group have a higher decrease than the blue group at 590 nm and show lower optical extinction values at wavelengths of 590, 600, and 610 nm than the blue group. Comparing the relation between red and blue groups to the reported configuration of oxyhemoglobin and deoxyhemoglobin chromophores, optical extinction coefficients in the wavelength range of 560–610 nm [122] illustrates the existence of a higher concentration of oxyhemoglobin and relatively lower concentration of deoxyhemoglobin in the red group (vessel branches 2, 3, 5, 6, and 7) than the blue group (vessel branches 1 and 4).

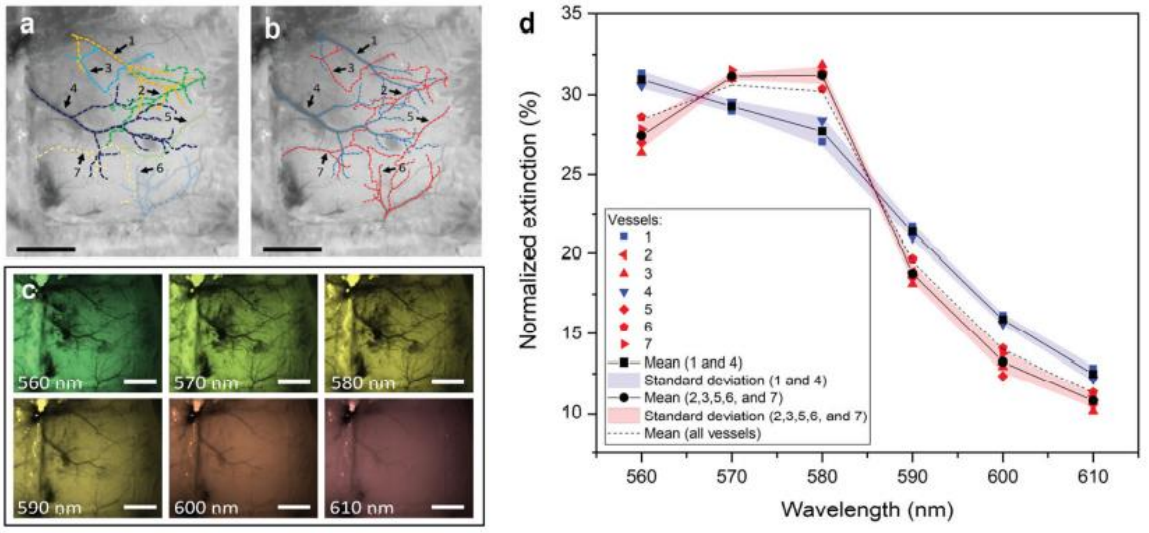

Figure 4.4. Cerebral arteries-veins separation using multispectral reflectance imaging (MSRI), in open skull imaging (i.e., condition 2). a) Labeling the vasculature branches on a regular white light image. The images were converted to gray color map to make the colored vasculature branches clear. b) The separated veins (blue) and arteries (red) (scale bars = 1 mm). c) Optical images of the brain illuminated by various wavelengths. d) Relative optical absorption values plotted for each branch.

A regular white-light image of the closed mouse skull (i.e., condition 1) is shown in Figure 4.5(a). The MSRI images captured through the cranial bone of the mouse do not show the vasculature network. Consequently, we were not able to identify the vessels branches and their intensities over the multispectral images in Figure 4.5(b).

Figure 4.6(a) shows mapped vasculature branches on a regular white-light image through the WttB implant (i.e., condition 3). Multispectral images as shown in Figure 4.6(c) resulted in a notable lower contrast compared with the references images (Figure 4.4(c)). The spectral behavior of the branches is plotted in Figure 4.6(d). The dashed line indicating the overall mean optical extinction for all seven branches shows a general decrease in the relative optical extinction compared with imaging the brain directly (Figure 4.4(c)), which is due to the reflected light from the WttB implant surface overcoming the

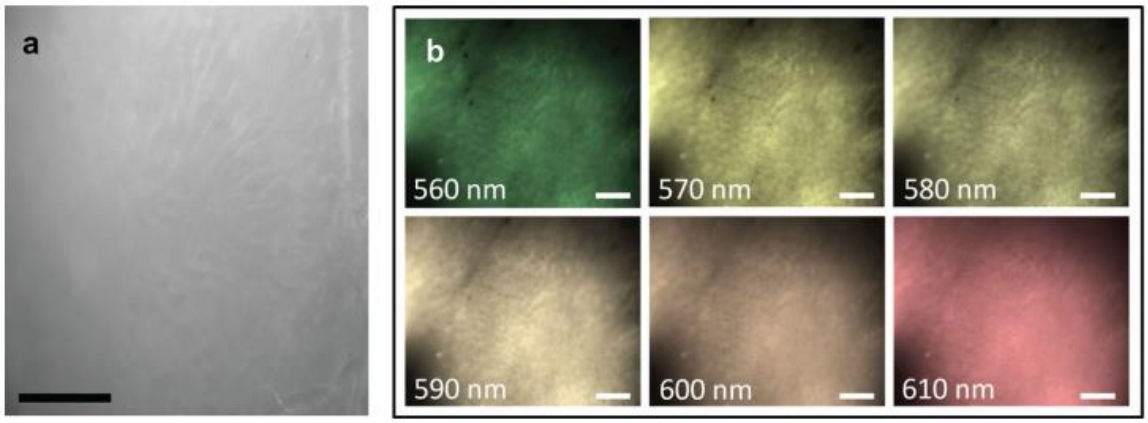

Figure 4.5. The multispectral reflectance imaging (MSRI) through closed skull (i.e., condition 1). a) Regular white-light image of the skull. The image was converted to gray color map to increase contrast. b) Optical images of the mouse skull illuminated by various wavelengths. As seen, the vasculature map is not evident when imaged through skull (scale bars = 1 mm).

vessels optical extinction. Similar to the direct brain images (imaging condition 2), the mean optical extinction (dashed line) is relatively high for wavelengths of 560–580 nm, followed by a decrease at wavelengths of 590, 600, and 610 nm. Although there is a lower deviation between the optical extinction values, the separate trend of the vessel branches 1 and 4 compared with branches 2, 3, 5, 6, and 7 is still noticeable. Accordingly, these two groups were labeled in red and blue and the mean and standard deviation of each group were separately calculated and shown in Figure 4.6(d). The analysis of the images obtained through WttB implant (imaging condition 3), shows a similar conclusion to the reference data (imaging condition 2). Although the relative optical extinction values have a notably higher deviation (which affects the accuracy of the analysis) compared with imaging the brain directly, the vein-artery separation is indeed doable through the WttB implant.

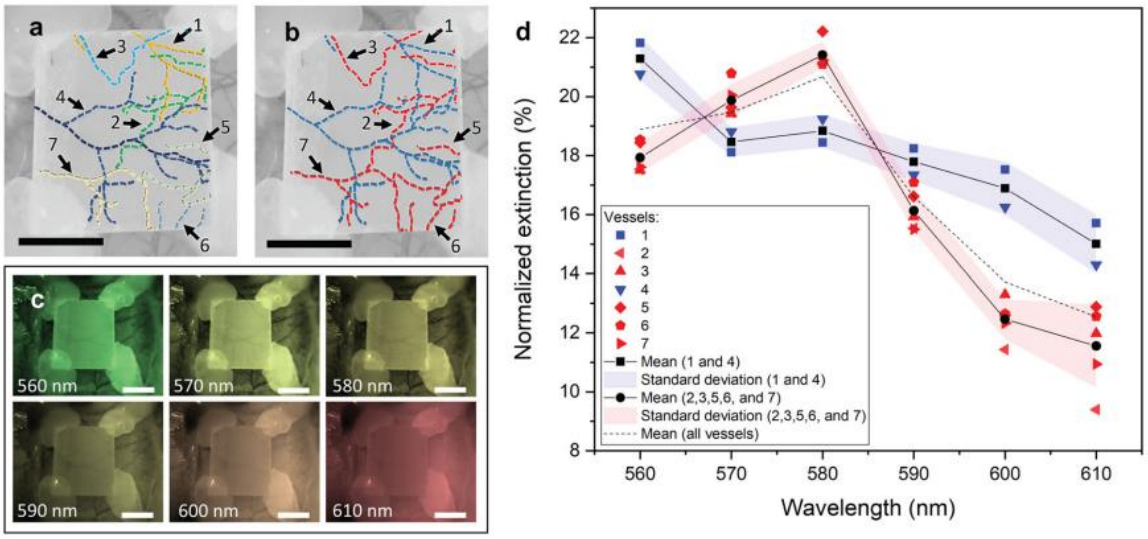

Figure 4.6. Cerebral arteries-veins separation using multispectral reflectance imaging (MSRI) through the Window to the Brain (WttB) implant (imaging condition 3). a) Labeling the vasculature branches on a regular white-light image of the implantation region (condition 3). b) The separated veins (blue) and arteries (red). c) Optical images of the brain illuminated by various wavelengths. d) Normalized mean intensity values plotted for each branch.

Comparison of the Improved LSI Image Quality: Through-Implant Versus Through-Skull

Figure 4.3(b) shows regular white-light images and LSI temporal contrast images of brain, through-skull, and through-implant. It should also be noted that after the surgery, blood flow is expected to be altered in response to the invasive craniectomy surgery (e.g., due to potential reactive hyperemia [47] (increased blood flow), changes in respiration, etc.). We previously reported the optimal exposure time for LSI imaging at each time point, so that we could compare the images of highest SNR that could be acquired of the brain, through-skull, and through-implant.

Line intensity profiles like the example shown in Figure 4.3(c) were analyzed for the brain, through-skull, and through-implant contrast images. To avoid selection bias, the

location of these line profiles were chosen arbitrarily at the region of interest (ROI) mid-points, as depicted in the regular white light image in Figure 4.3(b). From these intensity profiles, peak intensity and noise were determined (as described in the Methods section and illustrated in the inset of Figure 4.3(c)), and SNR ratio was calculated. Data for each imaging condition was averaged between the vessels and the mean SNR for each imaging condition is shown in Figure 4.7(a). As expected, the brain contrast image shows the highest SNR (imaging condition 2). The through-implant contrast image (imaging condition 3) resulted in the higher SNR compared with the through-skull contrast image (imaging condition 1) by 17.59% (relatively).

Sensitivity was calculated and resulted in 96.82% for the through-implant image (imaging condition 3) and 86.1% for the through-skull image (imaging condition 1). Then, we compared the sharpness (i.e., fall distance) of the vessels in the images to determine if the images were becoming blurred and losing resolution through the WttB implant.

The mean fall distance for each imaging condition is shown in Figure 4.7(b). The through-implant contrast image (imaging condition 3) provided 5.7 μm lower fall distance (higher sharpness) when compared with the through-skull contrast image (imaging condition 1).

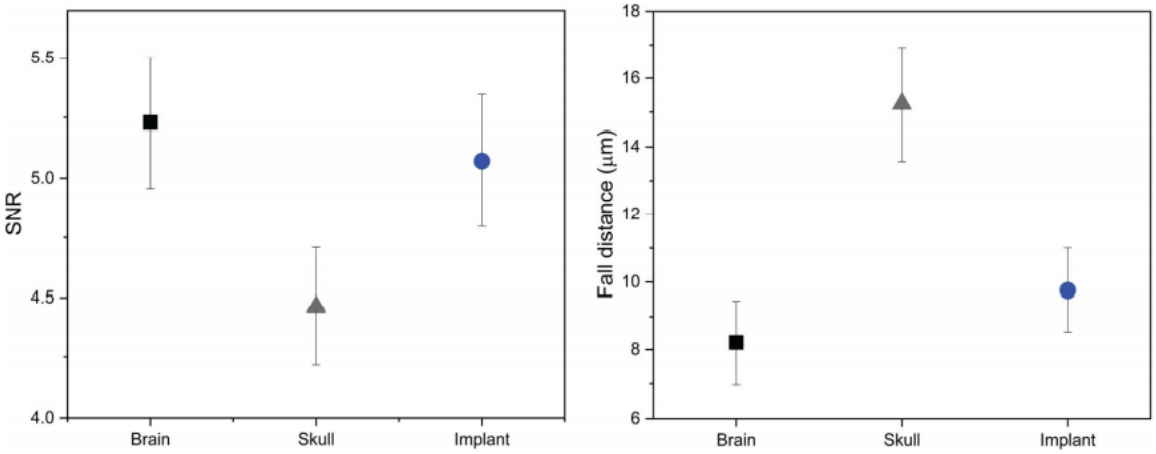

Figure 4.7. a) Mean signal to noise ratio (SNR) of contrast intensity and b) mean fall distance of contrast intensity along arbitrary line profiles on the brain, skull, and Window to the Brain (WttB) implant.

Assessing Arteriovenous Blood Flow Through-Implant

Figure 4.8 demonstrates the process of arteriovenous cerebral microcirculation image generation and the images obtained through each step. First, an LSI image is acquired, which contains information on vessel structures and relative flow velocities. The LSI image is also thresholded to provide a contrasted vessel map as a reference vasculature network (step 1). Next, MSRI imaging allows for separating cerebral veins and arteries based on optical extinction spectra over the wavelengths 560–610 nm, and this arteriovenous information is overlaid on the vasculature network LSI image (step 2). Finally, the arteriovenous vasculature network image is weighted by the relative blood flow velocities obtained during the initial LSI imaging in step 1 (step 3).

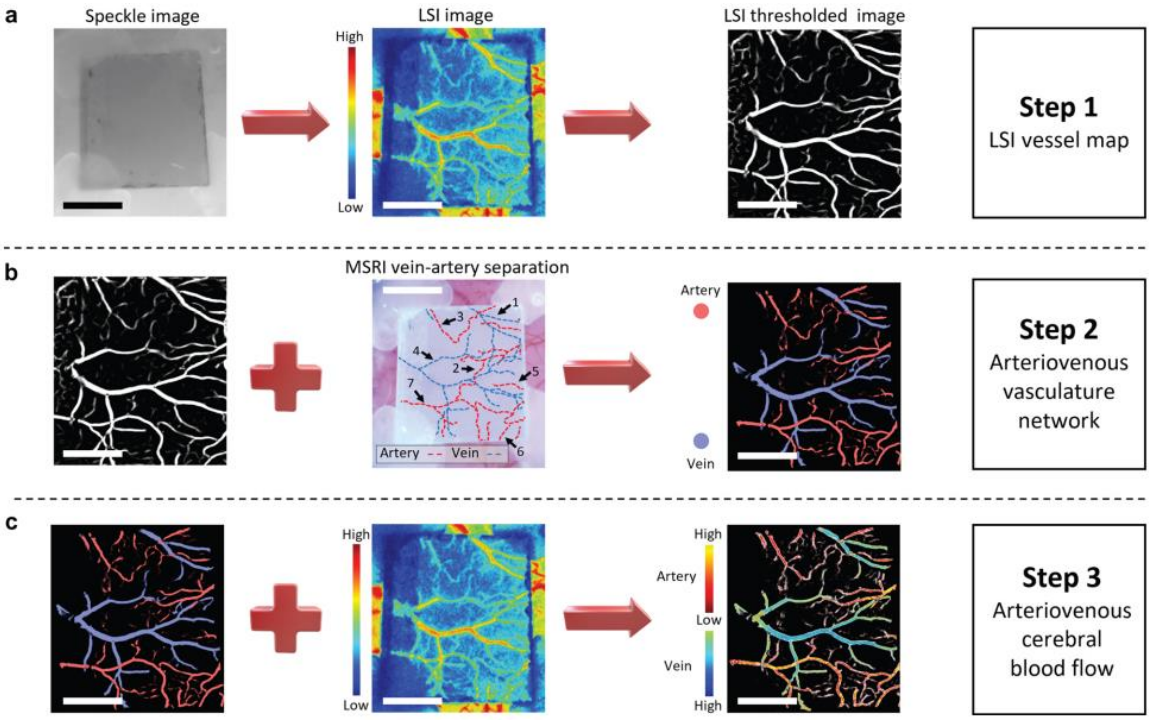

Figure 4.8. The steps of constructing an arteriovenous microcirculation image. a) Laser speckle imaging (LSI) image obtained by temporal analysis of laser speckle images. The LSI images were then processed to generate the LSI vessel map, where bright is the vasculature network and dark is the non-vascular region (step 1). b) Arteriovenous information from multispectral reflectance imaging (MSRI) is registered onto LSI vasculature network obtained using LSI (step 2). c) Arteriovenous vascular network is weighted by the blood flow map (LSI image) (step 3). Bar = 1 mm.

Discussion

The WttB holds the transformative potential for facilitating diagnosis and treatment of a wide variety of brain pathologies and neurological disorders. We envision this implant enabling delivery to and/or acquisition of light from the brain, in real-time, without the need for repeated highly-invasive craniotomies. Such access may also create a new platform for understanding the brain. In this chapter we assessed feasibility of MSRI-LSI imaging of the brain microcirculation through the WttB implant.

Other studies have investigated various methods of vein-artery separation, including velocity-based [123, 124], optical attenuation-based methods other than MSRI [97], and structural-based separation [125]. Besides the various proposed methods based on multi-wavelength imaging [126-130], like the MSRI approach we used in this present study, Miao *et al*. [131] distinguished arteries and veins by vascular anatomical features and optical intensity profiles in single-wavelength laser speckle contrast imaging (SW-LSCI) images, but arteries and veins may be misclassified because of similar absorption to the cerebral cortex. Feng *et al*. [132] proposed an automatic vein-artery separation method based on imaging the exposed cerebral cortex using SW-LSCI, however, the absorption and scattering of underlying parenchyma would also influence the accuracy of the vein-artery separation. Our method for accessing the intrinsic information of blood using MSRI with six wavelengths utilizes more complex instrumentation than many of these other reported methods of vein-artery separation [97, 125, 133]. Our reason for choosing the MSRI method over less complex vein-artery separation methods was that MSRI allows for functional imaging, which can be useful in our future functional brain imaging studies through the WttB implant. However, limitations exist for extracting componential information from intrinsic optical signals (IOSs). Optical properties of blood constituents other than hemoglobin (Hb), may absorb or scatter light, and these may alter the optical transmission of blood vessels, which can affect the measurement of hemoglobin [134].

The analysis of the MSRI images acquired through the open craniectomy (condition 2) clearly shows the different spectral behaviors of veins and arteries. For all vessels imaged, veins showed greater optical extinction in wavelengths of 560, 590, 600, and 610

nm, while arteries showed greater optical extinction at wavelengths of 570 and 580 nm. When the brain was imaged through skull (condition 1), only the main vessels were barely visible and analysis of MSRI for the microcirculation was not practical. On the other hand, the MSRI images obtained through the WttB implant (condition 3) resulted in a clear map of the vessels, although some of the microvessels were not visible. Comparing the vessel branches optical extinction shows similar results to the reference data (condition 2). Branches 1 and 4 were detected as vein with higher optical extinction at 560, 590, 600, 610 nm and branches 2, 3, 5, 6, and 7 resulting in higher optical extinction at 570 and 580 nm were thus identified as arteries. This result demonstrates that WttB implant can allow for reliable vein-artery separation imaging. It is worthwhile to mention that the images captured through the WttB implant have lower contrast, which limits the accuracy of the measurements when compared with imaging the brain directly. Lower average of optical extinction values in images through the WttB implant (16.98%) compared with open skull images (22.33%) shows this poorer contrast. Consequently, this lower contrast resulted in lower accuracy of the measurement shown by higher SD of red and blue groups. Averaged SD of red and blues groups is relatively increased by 33% and 31%, respectively, compared with open skull images.

Temporal contrast imaging has become a useful tool for brain blood flow applications as the images it produces contain functional information (i.e., relative blood velocity) in addition to showing structure of the vessel networks. As we previously reported, exposure time of 6 ms gave the highest SNR for both skull and WttB implant and was used for comparing SNR and sharpness of vessels imaged beneath each. Unlike our

previous study with compared two different spatial regions, here the comparison was made between three different imaging conditions. Thus, SNR and sharpness of vessels (fall distance) are evaluated for an identical target. Accordingly, we were able to compare the SNR values of through-implant and through-skull images to the reference image (open skull) to evaluate the sensitivity. This supplementary information to our previous study on SNR further demonstrates that the SNR of through-implant image is higher than that of through-skull imaging. Vessels imaged through the WttB implant have shorter fall distances, while vessels imaged through the skull have greater fall distances, indicating that vessels imaged through the implant have sharper borders compared to those imaged through the skull. As the size of vessels and velocity of blood flow is not expected to differ on average between the two imaging conditions, the apparent increase in vessel diameter imaged through the skull versus WttB implant is likely due to the blurring of the image through the skull. In general, the light transmission to the brain and reflection from the brain are lower in the through-skull image. Additionally, the skull scattering disorders the speckle pattern that was created by the brain hemodynamics. The skull poses these same issues for the MSRI imaging as well, and because the skull texture is not homogeneous, image correction or enhancement is very complex [26]. The reduction in border sharpness of the vessels imaged through the skull versus WttB implant is consistent with this explanation, and the blurred nature of the through-skull image compared with the through-implant image is visually apparent in Figure 4.3(b). It should also be noted that while the SNR and sharpness of the through-implant images are an improvement over the through-

skull images, the mouse skull is inherently transparent itself [26], which is not the case in larger animals or humans.

While vein-artery separation is possible by MSRI alone, in this study we combine MSRI with LSI. The combination with LSI has two major benefits. First, some of the microvessels are not visible through the WttB implant by MSRI since the transmitted light could not overcome the reflected light from the surface of the implant for these visible wavelengths (560–610 nm), and the microvessels have low contrast when compared with larger vessels. Registering the information from the MSRI to the LSI flow map, which does show the microvessels, helped to extend the arteriovenous information to the smaller vessel sizes, which were not visible by MSRI. Second, LSI imaging contains functional information (relative blood velocity), so combining these methods produces vasculature maps, which show relative velocities of flow within the separated arteries and veins. Figure 4.8 contains an example of how this method can produce arteriovenous vasculature network images weighted by relative blood flow velocity.

As seen in Figure 4.3(b), much more precise velocity information, particularly of microvessels, can be detected through the WttB implant, while the reduced sharpness of the vessels imaged through skull obscures precise flow determinations (Figures 4.3(b) and 4.7). Imaging microvessels (usually involving small arteries of less than 150 μm in diameter, arterioles, capillaries, and venules [72, 73]) is important for many applications, as microcirculation plays a critical role in physiological processes such as tissue oxygenation and nutritional exchange [74]. Monitoring the spatiotemporal characteristics of microcirculation is crucial for studying the normal and pathophysiologic conditions of

tissue metabolism. It is also useful for assessing microcirculatory dysfunction due to disease conditions such as type 2 diabetes, peripheral vascular disease, atherosclerotic coronary artery disease, obesity, heart failure, Alzheimer's, schizophrenia, and hypertension, among others [51-53]. In addition, quantification of dynamic blood flow, angiogenesis, and vessel density are critical for monitoring the progression of wound healing [54]. Although high-resolution vascular network mapping is possible using imaging modalities such as CT, these approaches require injection of contrast agents and pose disadvantages such as radiation exposure. Existing noninvasive methodologies (including LSI through skull) are inadequate to study blood flow at microvessel resolution [55]. Windows such as the WttB implant are thus important tools for research, and in the case of the WttB implant can become important enablers of clinical diagnostics and therapy involving cerebral microvessels.

Creating novel windows for brain studies has been gaining attention recently [4, 56-58]. Some of these studies, involving optical clearing agents (OCAs) applied to the scalp overlying native skull, have shown limited success due to optical losses and scattering in the skull [113]. These skin optical clearing strategies could work in conjunction with the WttB implant, to allow for imaging of cerebral blood flow in awake and behaving animals through closed scalp and implant, for example, to study cerebrovascular hemodynamic responses and tissue oxygenation to other stimuli. Future studies by our group will explore this combined OCA-WttB strategy, as well as include additional imaging modalities that can couple with LSI to provide additive information, such as OCT and IOS.

There are several limitations to the current study. The sample sizes used were small (n = 1), and further experiments are needed to confirm the reproducibility of these findings. While a permanent cranial implant can allow for less invasive imaging of the brain at later time points, it requires an initial implantation surgery, which carries associated risks such as infection.

Conclusion

In conclusion, this chapter has demonstrated the ability to perform MSRI-LSI across a transparent cranial implant, to allow for cerebral vessel networks to be mapped, including microvessels. These images contain additional information such as vein-artery separation and relative blood flow velocities, information which is of value scientifically and medically. The WttB implant provides substantial improvements over imaging through the murine cranial bone, where microvessels are not visible and MSRI cannot be performed.

Citation: The work presented in this chapter was published in *Lasers in Surgery and Medicine* [9]:

> Davoodzadeh N, Cano-Velazquez MS, Halaney DL, Jonak C, Binder D, Aguilar G. Optical access to arteriovenous cerebral microcirculation through a transparent cranial implant. *Lasers in Surgery and Medicine* 51(10):920-932 (2019).

Acknowledgments

I would like to acknowledge the contribution of my co-authors to this work: Nami Davoodzadeh, Mildred S. Cano-Velázquez, Carrie R. Jonak, Devin K. Binder, and Guillermo Aguilar. This study was supported by National Science Foundation (NSF-PIRE #1545852) and "Beca Mixta" from National Council of Science and Technology of Mexico

(CONACYT) (741249). The authors would like to acknowledge Gottlieb Uahengo for fabricating the YSZ samples.

Chapter 5. Enhanced Near Infrared Optical Access to the Brain with a Transparent Cranial Implant and Scalp Optical Clearing

Background

The brain is protected by different tissue layers, each of them having different optical properties (e.g., refractive index contrast, scattering and absorption); hence, the analysis of the spectral features provides information about these different layers [135]. Furthermore, it has been shown that physiological changes in the different head tissues produce variations in their optical properties thereby changing the spectral features of the transmitted and reflected light [136]. Compared to visible light, some spectral regions in the Near Infrared (NIR) spectral range (800 to 2500 nm) offers advantages such as reduced scattering and absorption as well as a deeper penetration depth in tissue media [136-138]. Because of these features, some spectral windows within the NIR wavelength range have shown promising results for brain studies, including deep imaging, diagnostics and therapeutic applications in brain diseases [139-142].

Different optically transparent windows for head tissues have been identified within the NIR spectral range. These wavelength windows avoid light attenuation by the tissue due to water absorption peaks located at 1450 nm and 1940 nm [135, 143, 144]. The first window NIR-I (~ 700 - 1000 nm), or conventional window, has been well characterized and studied for most tissues, including brain and other soft tissues [135]. Two additional optical windows have been also identified: NIR-II (~ 1000 - 1350 nm) and NIR-III, or short-wave infrared SWIR, (~ 1550 - 1870 nm); the latter spectral region has shown to provide maximum light penetration for some kinds of tissues [141, 145, 146]. More

recently, a fourth optical window, SWIR-II (~ 2100 - 2300 nm) has allowed for improved optical studies of the brain and for deep brain imaging, particularly when compared to the NIR-II window [142]. All of these spectral regions have been explored for many biophotonic applications, although the NIR windows have particularly shown excellent potential for noninvasive through-skull *in vivo* brain imaging and spectroscopy [140, 141, 145, 147]. Nonetheless, it is always desirable to reduce the highly scattering cranial bone over the cortex, which hinders the observation of optical signals deriving from deeper tissues and reduce the light penetration distance.

Reduction of the scattering from the skull has been addressed in animal models by craniotomy [57, 148, 149], using a thinned-skull cranial physical window [27, 150] or by polishing and reinforcing a thinned skull piece [110]. Other approaches include optical clearing of the skull [29, 114, 151], or replacement of a portion of the skull with a physical transparent window made from glass or PDMS [2-4]. All of these are powerful research techniques, but not adequate for translation into human applications that may require permanent cranial implants. While skull thinning and polishing techniques affect the required protection for the brain, glass-based physical windows have a very low toughness (K_{IC} = 0.7 - 0.9 MPa $\cdot$ $m^{1/2}$) [35] increasing the potentiality of catastrophic failure by fracture. Similarly, the effects of skull optical clearing agents for long-term use on human skull is still unknown. A number of biomedical considerations including biocompatibility, mechanical strength, and ageing performance must be considered for a physical window intended for eventual clinical applications. Conventional cranial prosthesis including titanium, alumina, and acrylic [36], do not provide the desired combination of transparency

and toughness required for clinically-viable transparent cranial implants. Other materials such as sapphire have been also proposed as implants owing to its broadband transparency and toughness thereby providing optical access to the brain [152]. We have recently also introduced a transparent nanocrystalline yttria-stabilized-zirconia cranial implant material showing suitable mechanical strength and biocompatibility sought for a clinically-viable permanent cranial implant for patients [6, 37, 38]. Yttria-stabilized zirconia (YSZ) is an attractive alternative due to its relatively high fracture toughness (K_{IC} ~ 8 MPa · $m^{1/2}$) [39], as well as its proven biocompatibility in dental and orthopedic applications [40-42]. By performing biocompatibility and ageing tests, and through imaging techniques such as optical coherence tomography [6], ultrasound transmission [43], multi-wavelength intrinsic optical signal imaging [9] and Laser Speckle Imaging (LSI) [7, 44], we have demonstrated the feasibility of YSZ implants for chronic cortical imaging in an acute murine model. Thus, YSZ holds as a promising platform for developing optically transparent implants with excellent potential for human applications.

In this chapter, we report on the enhancement in optical access provided by the transparent YSZ implant for brain studies in the NIR wavelength range. Because this cranial implant is sought as a means to obtain optical access for post-operatory and prolonged diagnostics and/or therapy purposes, scalp scattering must be overcome. In this context, we also evaluate the use of optical clearing agents (OCAs) in the scalp, particularly their effects on the optical transmittance in the NIR spectral range. As shown in previous reports, OCAs provide greater optical probing depths and better contrast, as well as improved light focusing and spatial resolution [153-155]. Therefore, evaluation of the

optical features of the YSZ implant together with the use of OCAs in the NIR spectral range will provide useful information for theranostics applications operating in this wavelength range (e.g., photobiomodulation [156-158], NIR and fluorescence imaging [137, 159], cancer diagnosis [160, 161] and brain edema [162]). Hence, we evaluate the enhancement in optical access to the brain upon comparing *ex vivo* transmittance measurements of mice native skull and the YSZ cranial implant coupled with scalp and OCAs. Using the transmittance data, the total attenuation lengths were calculated showing that this combination (YSZ and OCAs) offers the best option for gaining improved optical access to the brain.

Methods

Implant Fabrication and Preparation

Implant fabrication and preparation was conducted as described in Chapter 2 (page 8). For studies described in this chapter, implant dimensions were approximately 2.6 x 2.1 mm, and had a thickness of 440 ± 1 μm.

Scalp and Skull Samples

The tissue samples were obtained from animals from the University of California, Riverside (UCR). All experimental procedures and humane care of mice were conducted under a protocol approved by UCR's Institutional Animal Care and Use Committee, and in conformance with the Guide for the Care and Use of Laboratory Animals published by the National Institutes of Health (NIH Publication No. 85-23, revised 1996). The n = 9 8-12 week old C57Bl/6 male mice (Jackson Laboratory) used in this study were housed under a 12-hour light and 12-hour dark cycle with *ad libitum* access to food and water.

Surgical Procedures

Craniectomy surgery was conducted as described in Chapter 2 (page 9).

Optical Clearing

A mixture of two biocompatible agents, PEG-400 (PEG) and Propylene Glycol (PG) (Fisher Scientific, California, US), were used as scattering reducer and penetration enhancer, respectively, at a volume ratio of 9:1 [163, 164]. The OCA was prepared and topically applied at room temperature. A thin layer of the OCA was applied on the sample and remained for 50 minutes [163]. Characterization experiments were performed before and immediately after applying the OCA; the increase in transmittance for each tissue used in the samples was monitored every minute over a 50-minute period. For our experimental conditions, the maxima in transmittance were achieved within 50 minutes.

Tissue Characterization

Optical transmittance measurements of the different samples used in this study were obtained through optical spectrometry in the NIR. The setup used to obtain the transmittance spectra incorporates two multimode optical fibers (P400-2-VIS-NIR, Ocean Optics, FL) attached to individual fiber holders including VIS-NIR collimating lenses (MP-74-UV, Ocean Optics, FL, with focal length f = 10 mm, lens diameter D = 5 mm and NA = D/2 f = 0:4). As depicted in Figure 5.1, the holders were attached to a mechanical rail allowing to adjust the separation between the fibers and to allocate a sample holder. After the sample is fixed, the fiber holders were tightly joined together to mitigate detrimental effects from ambient light and back reflections. The light source used for these measurements was a visible-NIR source (HL2000 FHSA, Ocean Optics, FL) launched into

one of the optical fibers. The beam exiting the launching fiber then traverses the sample and is collected by the other fiber, which is connected to a solid-state spectrometer (NIRQUEST 520, Ocean Optics, FL) to obtain the optical transmission spectra. Spectra were acquired averaging 10 measurements, with an integration time of 300 ms, in the 900-2400 nm wavelength range.

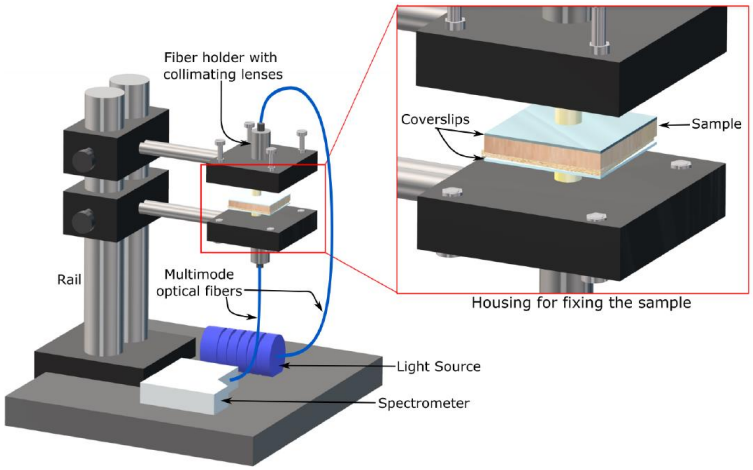

Figure 5.1. Collimated transmittance measurements setup. The inset shows the housing for fixing the sample, i.e., the fiber holders with the VIS-NIR collimating lenses. As seen in the inset, the samples are placed between coverslips (see text for further details).

For all the measurements, the collimated transmittance (T(λ)) was calculated as the ratio of light transmitted through the sample to the total incident light, i.e.:

$$T(\lambda) = \frac{S(\lambda)-D}{I(\lambda)-D} \quad (1)$$

where λ is the wavelength, S is the measured spectral intensity, I is the total light incident and D represents the reference reading under dark conditions (i.e., no light impinging on the sample). Basic models of light propagation in biological tissues are described in terms of radiation transport in a random inhomogeneous media, which includes ballistic and

diffuse light [136, 139, 142, 165]. However, when using a collimated beam, and in the case of thin samples with large absorption coefficients and relatively small light scattering, the ballistic part plays a dominant role and the diffusive part is negligible [136, 142, 165]. We further consider that the ballistic photons in the scattering samples are governed by the Beer-Lambert law. Hence, for analyzing the influence of the sample thickness z in the spectral transmittance, the total attenuation length ($l_t(\lambda)$) was calculated as [136, 139, 142, 165]:

$$l_t(\lambda) = \frac{z}{-\ln\left(T(\lambda)\right)} \quad (2)$$

Note that the attenuation length takes into account the sample thickness and therefore provides a better insight of the light penetration through the samples. In particular, for our experiments, the thicknesses of the samples are: 440 ± 1μm, 159 ± 1μm and 710 ± 20μm for the YSZ implant, the mice skull and scalp, respectively. Hence, the YSZ implant is 2.5 times thicker than the mice skull.

Experimental Method

The experimental procedure for measuring the ballistic transmittance through the different tissues and the implant was similar to those reported previously for spectroscopic measurements on soft tissue [139, 142, 165]. Transmittance measurements were obtained for three sets of samples arranged as the different scenarios illustrated in Figure 5.2. Spectra were obtained first for the skull and subsequently for the stacked array formed by the scalp placed on top of the skull. The OCAs were then applied on the scalp and the spectral transmittance was acquired once again. This set of measurements were also performed using the YSZ implant instead of the skull. The stacking arrangement used for this

measurements allowed for evaluating the effects of each layer on the spectral features of the sample. This further allows for comparing the spectral features of the skull and the YSZ implant under similar conditions. Excised full thickness scalp and forehead cranial bone were rinsed briefly in saline solution to remove the excess blood and their thicknesses were measured before placing them in the stacked samples. These were finally placed between two glass microscope coverslips to obtain the transmittance spectra. The same procedure was followed for the YSZ implant. For the cleared skin measurements, the scalps were topically exposed to PEG and PG as a scattering reducer and a penetration enhancer, respectively [163, 164].

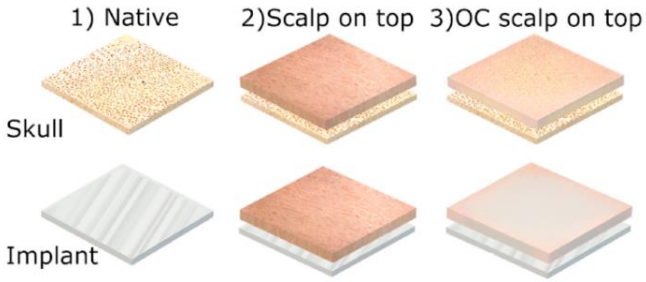

Figure 5.2. Stacked sample arrangement used to obtain the spectral transmittance of: 1) the native skull and YSZ implant, 2) the scalp on top of the skull and the YSZ implant, 3) optical cleared (OC) scalp on top of native skull and implant.

Results and Discussion

Figure 5.3 shows the transmittance ($T(\lambda)$) and the attenuation length ($l_t(\lambda)$) calculated for the native skull and the implant. The transmittance measurements (Figure 5.3(a)) show that the YSZ implant is more transparent throughout the tested NIR range (900-2400 nm) including all of the optical windows commonly used for biophotonic applications (i.e., NIR I, NIR II, SWIR I and SWIR II). This is due to the significant reduction in scattering and absorption when using the YSZ implant. In terms of relative differences in the optical

properties between skull and the implant, the latter improves the light transmission within the water absorption bands owing to its reduced water content compared to the native skull (70-75%) [139]. The skull transmittance shows the typical water absorption bands in the NIR spectral region (1450 nm and 1940 nm [143, 144]), while the YSZ implant shows improved transmittance in these bands. The water absorption peaks apparent in the implant spectrum are due to traces of the saline solution used for rinsing aiming at obtaining a fair comparison with the treated tissue samples. A simple calculation of the increase of light transmitted in these bands using the YSZ implant compared to the native skull yields values of 47% at 1450 nm and 53% at 1940 nm. The resulting attenuation length shown in Figure 5.3(b) further indicates that, even for the spectral regions with the smallest increase in transmission (e.g., 3% at 1300 nm), light can penetrate deeper when compared to the native skull. Clearly, with exception of the second water absorption band, the attenuation length obtained with the implant increases at least by 1.3 mm, i.e., a four-fold increase in length compared to the skull. The spectral regions covered by the water absorption peaks in the NIR have not been explored for through-skull techniques because of its high water content. Thus, the improved transmission obtained with the implant opens the possibility to explore new techniques in these wavelength ranges.

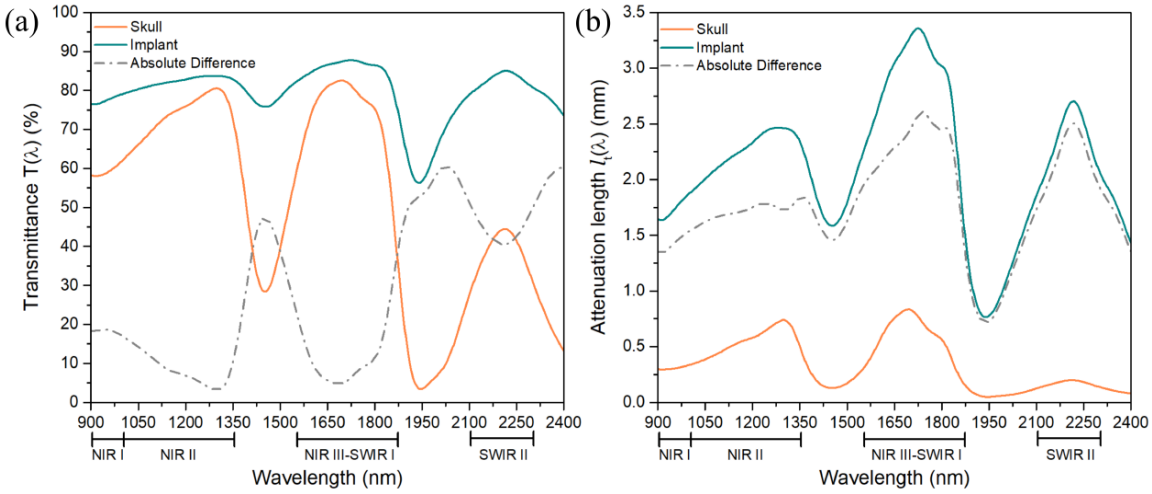

Figure 5.3. Transmittance a) and total attenuation length b) for the skull and the YSZ implant. The YSZ implant shows better transmittance throughout the full 900-2400 nm spectral range compared to the native skull.

The effect of the scalp on the spectra is evident in Figure 5.4(a), showing a considerable reduction in transmission owing to the increased scattering inherent to this tissue [135-137]. As shown in Figure 5.4(b), this leads to reduced attenuation lengths for both sample arrangements, i.e., scalp either on top of the skull or on the YSZ implant. Although for both cases the scalp stacking leads to a reduction in transmittance of at least 60%, the sample with the implant still provides the best performance, as confirmed by the attenuation length. Throughout all the spectral range, the sample formed with the scalp and the YSZ implant provides improved light penetration. Clearly, the scalp introduces large optical attenuation effects that must be overcome for the implant to become a convenient means to obtain access for non-invasive optical techniques for post-operatory diagnostics and/or therapeutic purposes. Hence, we evaluated the use of OCAs as a technique for improving the transmittance of the samples.

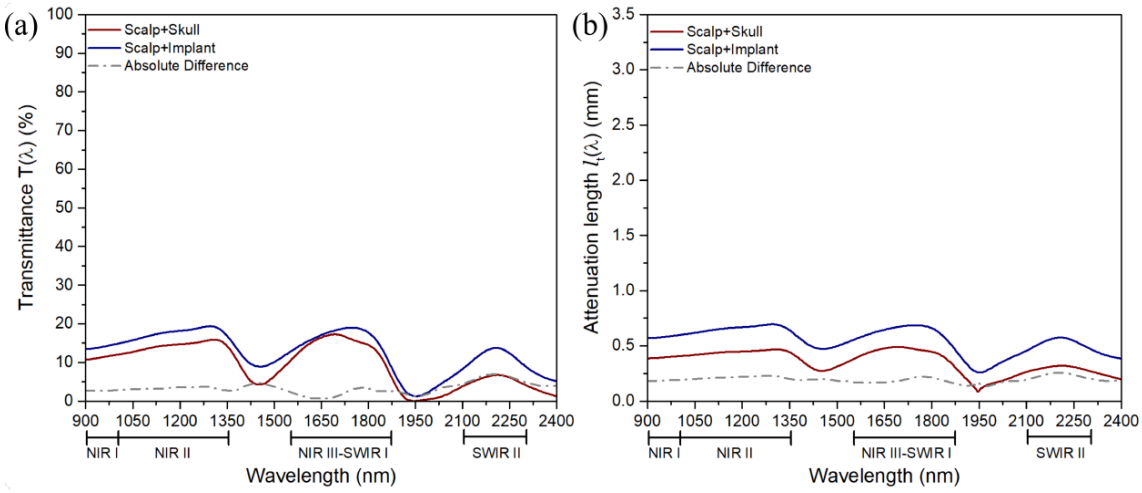

Figure 5.4. Transmittance a) and total attenuation length b) comparing the stacked samples of the scalp on top of the skull and on the YSZ implant. The sample with the YSZ implant still shows better transmittance and improved attenuation length compared to the sample with the native skull; however, the enhancement is only of 6% in the best case.

The effects of applying a layer of OCAs on the scalp are evident in Figure 5.5; the transmittance spectra increases by 20% for the sample with the skull, while for the YSZ implant the enhancement is 40% (Figure 5.5(a)). As shown in Figure 5.5(b), the attenuation length for both samples increases accordingly; when compared to the results shown in Figure 5.4(b), it is clear that the OCAs effectively enhance the light penetration yielding larger attenuation lengths throughout the whole NIR range for both samples. Further comparison of this parameter for the two samples show that the YSZ provides improved light penetration than attained with the skull (up to 1.8 mm more at 1717 nm). These results are consistent with previous reports involving OCAs [153-155], and further confirm that together with the YSZ implant, these biocompatible agents provide attractive features for optical access to the brain tissue without scalp removal.

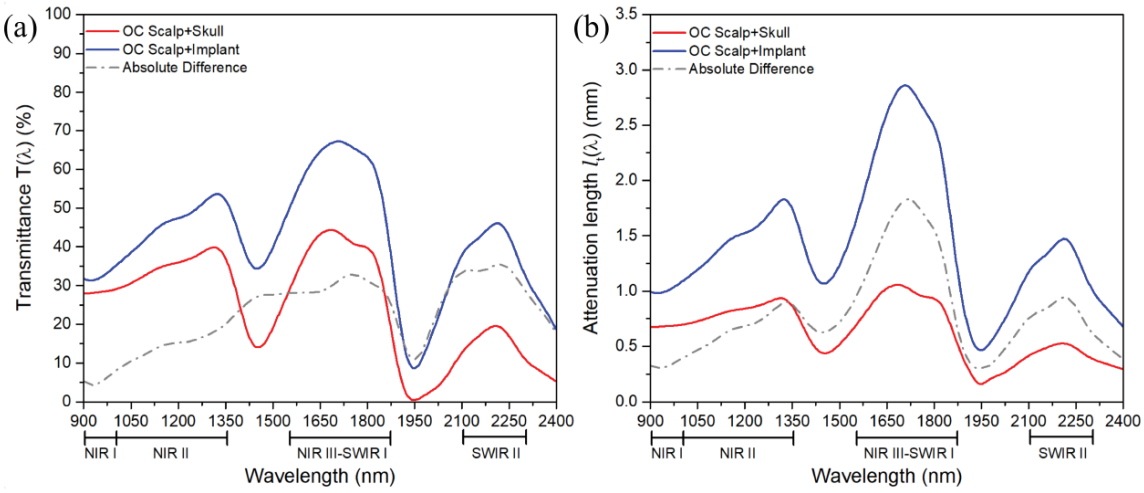

Figure 5.5. Transmittance a) and total attenuation length b) comparing the stacked samples of the scalp on top of the skull and on the YSZ implant after using the OCAs. The sample using the YSZ implant with optically cleared scalp (OC scalp) shows an increase of up to 30% in transmittance compared to the sample with the skull.

A better idea of the impact of our results in each of the NIR optical windows can be appreciated in Figure 5.6, showing a summary of the transmittances and attenuation lengths obtained from our experiments. Comparing all the scenarios, the YSZ implant provides the best option for optical access, showing the largest transmittance and attenuation length. Although the transmittance for the YSZ is seemingly comparable to that of the skull for the NIR II and NIR III windows, the attenuation lengths for the implant are clearly larger than those obtained for the skull (Figure 5.6(b)). In fact, for all the windows, the YSZ implant offers improved features and thus better potential for deeper optical access to the brain tissue, even when using the scalp on top. When using OCAs to reduce the scattering of the scalp, the YSZ implant offers improved transmittance and larger attenuation lengths than those observed for the skull. Remarkably, the attenuation lengths achieved with the OCAs and the YSZ show at least a two-fold increase for the last three windows (i.e., NIR

II, NIR III-SWIR I and SWIR II). Evidently, the optical features offered by the YSZ implant together with the use of biocompatible agents to reduce scalp scattering pose new possibilities for probing brain tissue in spectral regions that are commonly discarded owing to the low penetration depths that can be commonly achieved [139]. Note that these results provide a direct comparison of the attenuation lengths achieved when replacing the mice skull by the YSZ implant. It is evident that the transparency of the YSZ implant improves the light penetration, but the ultimate increase in penetration depth achievable will depend on the scattering features of the specific bone tissue. Further considerations for the analysis of the spectral transmission should include the diffuse light component, which is relevant when using thicker and more absorbent tissue samples (e.g., rat skull [139]).

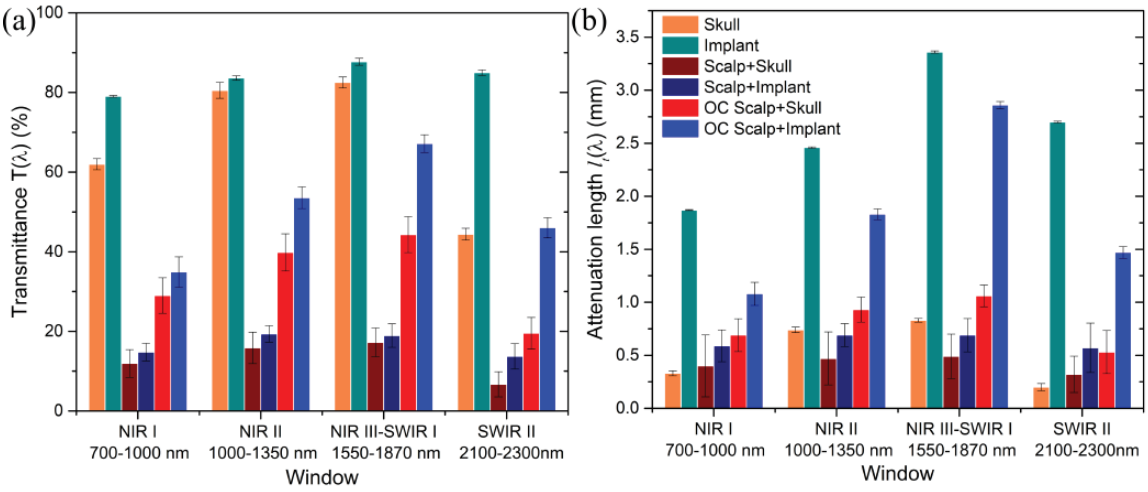

Figure 5.6. Summary of the registered transmittance a) and total attenuation length b) for the different samples tested in our experiments. Throughout the whole NIR spectral range the YSZ implant shows enhanced transmittance among all the samples. The use of OCAs on the scalp effectively increases both, the transmittance and the attenuation length, providing enhanced light penetration. The most favored optical window for the stacked sample of optically cleared scalp on top of the YSZ implant is the NIR III (1550-1870 nm, T = 67%, l_t = 2.86 mm). Error bars represent standard deviation (n = 3).

The enhanced transparency of the YSZ implant coupled with the OCAs shows promising features to facilitate various NIR techniques for theranostics. Photobiomodulation (600-1064 nm) [156-158], NIR and fluorescence imaging (700-1700 nm) [137, 159], as well as some types of cancer diagnosis (1500-1800 nm) [160, 161] and brain edema [162] are a few examples of optical techniques that could benefit from the improved transmission in NIR spectral range offered by the YSZ implant. Additionally, any potential adhesion of biochemical agents and/or tissue growth on the implant (e.g., fibrotic tissue, proteins, cell adhesion) could be potentially monitored over time using IR reflection techniques [166]. Imaging techniques (e.g., LSI, fluorescence, absorption) that have been successfully demonstrated to improve with clearing and thinning skull methods [114], may also benefit from the combination of the OCAs and a transparent YSZ implant.

Conclusions

We have evaluated the optical transmission and attenuation length of a novel YSZ-based implant intended for chronic optical access to the brain performing *ex vivo* transmittance measurements. In addition, the use of OCAs to overcome the low transparency of the scalp was explored together with the implant. Direct comparison of the YSZ implant with mouse skull in different stacked arrangements showed that this ceramic material offers enhanced transmission throughout the NIR spectral range. Furthermore, since OCAs effectively reduce the scattering features of the scalp, the use of these biocompatible agents together with the YSZ implant provide improved optical features. In particular, when compared to a typical arrangement comprised of scalp and native skull, the use of the YSZ implant yields an increase in transmittance of up to 50% and attenuation lengths of up to 2.4 mm

(i.e., a five-fold increase in light penetration). These experimental results show evidence that the YSZ implant, when used together with the OCAs, offers the best option for gaining improved optical access to the brain. This novel approach seeks to provide new opportunities for monitoring brain conditions on a chronically recurring basis, without requiring repeated craniotomies or scalp removal. Although this study represents only the first step towards the application of NIR optical techniques for brain theranostics through an implant, it offers a relevant insight of the opportunities that this transparent material may eventually provide.

Citation: The work presented in this chapter was published in *Biomedical Optics Express* [10]:

> Cano-Velázquez MS, Davoodzadeh N, Halaney D, Jonak CR, Binder DK, Hernandez-Cordero J, Aguilar G. Enhanced near infrared optical access to the brain with a transparent cranial implant and scalp optical clearing. *Biomed. Opt. Express* 10, 3369-3379 (2019).

Acknowledgments

I would like to acknowledge the contribution of my co-authors to this work: Mildred S. Cano-Velázquez, Nami Davoodzadeh, Carrie R. Jonak, Devin K. Binder, Juan Hernández-Cordero and Guillermo Aguilar. This study was supported by Conacyt-FONCICYT (246648); Conacyt-'Beca Mixta' (741249); National Science Foundation (NSF) (NSF-PIRE 1545852, NSF-EAGER 1547014). The authors would like to acknowledge Gottlieb Uahengo for fabricating the YSZ samples.

Chapter 6. Evaluation of Laser Bacterial Anti-Fouling of Transparent Nanocrystalline Yttria-Stabilized-Zirconia Cranial Implant

Background

The fundamental aim of the window to the brain (WttB) implant/platform is to improve patient care by providing a technique for delivery and/or collection of light into/from the brain, on demand, over large areas, and on a chronically recurring basis without the need for repeated craniotomies. Transparent nanocrystalline yttria-stabilized-zirconia (nc-YSZ) provides both the transparency and toughness required for enhancing the light-based diagnosis and treatment of a wide variety of brain pathologies including cerebral edema, traumatic brain injury, stroke, glioma, and neurodegenerative diseases, among many others. Using optical coherence tomography (OCT), we demonstrated the initial feasibility of nc-YSZ cranial implants within the context of cortical imaging of an acute murine model [6]. For optical clearing of the scalp temporarily, our study on delivery techniques of optical clearing agents (OCA) such as propylene glycol (PG) showed that the combination of heated PG, micro-needling and vacuum pretreatments, and positive pressure posttreatment significantly enhanced the perfusion of this topically applied OCA [167].

Unfortunately, bacterial adhesion to cranial implant biomaterials (fouling) is followed by colonization, biofilm formation, infection and, eventually, implant failure [168]. Despite advances in sterilization and antiseptic techniques, deep infection is the major leading complication after cranioplasty, with reported rates between 21% and 40% [169-172]. Infection might evolve due to contamination during surgery, local infections elsewhere in the body, or suppressed immune system [173]. Thus, bacterial adhesion to the

implant and biofilm formation may limit the use of WttB for optical imaging and therapy, especially in immunocompromised patients. In particular, Escherichia coli (E. coli) is one of the most common isolates in gram-negative bacillary meningitis after cranial surgery or trauma in adults [168, 174]. It has also been shown that E. coli peritonitis causes increased blood-brain barrier permeability [175]. Due to poor penetration of antimicrobial agents to the cerebrospinal fluid and resistance of biofilms to antimicrobial agents, the conventional treatment for cranial implant infection is removal and replacement of the implant, adding delays and cost to cranioplasties [176, 177].

Sterilization of implant surfaces using lasers has been suggested [178, 179] and resulted in several promising reports [180, 181]. Previous data, however, demonstrates that temperature increase of 10°C induces tissue damage in the bone [182-184] and denaturation of lipids and proteins [185]. Therefore, it is critical to ensure that the temperature change stays below this threshold for thermal damage during laser application.

Genetically engineered bacteria that express luciferase, from the American firefly, has been used in several models to optically monitor bacterial number and viability in real time [186]. Bioluminescence occurs when luciferase catalyzes the formation of the luciferin excited state in the presence of Mg^{2+} , ATP, and oxygen. Therefore, light can only be produced from live and metabolically active cells, which are able to generate ATP [187]. Validation of a noninvasive, real-time imaging technology using bioluminescent E. coli has been demonstrated in the neutropenic mouse thigh model of infection [188]. This demonstration showed that the intensity of luminescence images is proportional to the magnitude of the infection.

The transparency of the nc-YSZ implant provides us with the unique opportunity to shine a near-infrared (NIR) laser to treat the infected biomaterial locally and chronically, on-demand, without the need for removing the implant. Although the use of lasers to reduce bacterial growth *in vitro* was previously reported [189-191], the use of a transparent nc-YSZ implant for a non-invasive laser treatment of implant fouling is entirely novel. The objective of this *in vitro* study was to model bacterial growth underneath the nc-YSZ implant (i.e., implant fouling) and study the efficacy of distinct NIR laser irradiation parameters to disrupt bacteria viability and biofilm formation. The results from this *in vitro* model provide a strategy to study properties of nc-YSZ transparent cranial implants prior to investigations in more complex models such as *in vivo* animal studies.

Methods

Implant Fabrication and Preparation

Implant fabrication and preparation was conducted as described in Chapter 2 (page 8). Details of nc-YSZ fabrication and optical characterization have been reported previously [38, 192], and %Transmittance measured with a Varian Cary 500 spectrophotometer (350–3,300 nm) and Equinox 55 FTIR spectrometer (3,300–13,000 nm) is provided in Figure 6.1. The room temperature thermal conductivity (k) for nc-YSZ has been reported previously as ~ 2–2.45 W m^{-1} K^{-1} [193], and the specific heat (C_p) of YSZ (an intrinsic material property which does not exhibit any significant dependence on stabilizer content, phase composition or microstructure) has been reported as 427 ± 14 J kg^{-1} K^{-1} [194]. The volumetric density (ρ) of the nc-YSZ samples used in this study was measured to be 6042

kg m^{-3}, allowing for the thermal diffusivity (α) of our samples to be calculated as ~7.75x10^{-3} – 9.49x10^{-3} cm^2 s^{-1} (Equation 1):

$$\alpha = \frac{\kappa}{\rho \cdot C_p} \quad (1)$$

The nc-YSZ samples used in this study were circular discs of 19.07 mm diameter and 0.70 mm thickness, and the average surface roughness (Ra) was measured using atomic force microscopy (AIST-NT) to be approximately 10nm. Prior to each experiment, nc-YSZ samples were dry sterilized (Germinator 500) at 250°C for 10 seconds to remove all pre-existing bacteria.

Bacteria Inoculation

For all experiments, genetically engineered BL21 E. coli (CMC0014, Sigma–Aldrich, St. Louis, MO) phenotype that emits bioluminescence was used. Briefly, BL21 cells were transformed with *P. Pyralis* luciferase gene on pET28b(+) vector. The transformants were cultured in Lysogeny Broth (LB) media supplemented with Kanamycin antibiotic (K^+). Laser irradiation experiments were run on agar plates containing K^+ and protein expression inducer Isopropyl b-D-1-thiogalactopyranoside (IPTG). Specifically, BL21 E. coli culture was grown overnight in a shaker at 37°C for 16 hours in the LB-K^+ until the OD_{600} reached 0.6–0.7.

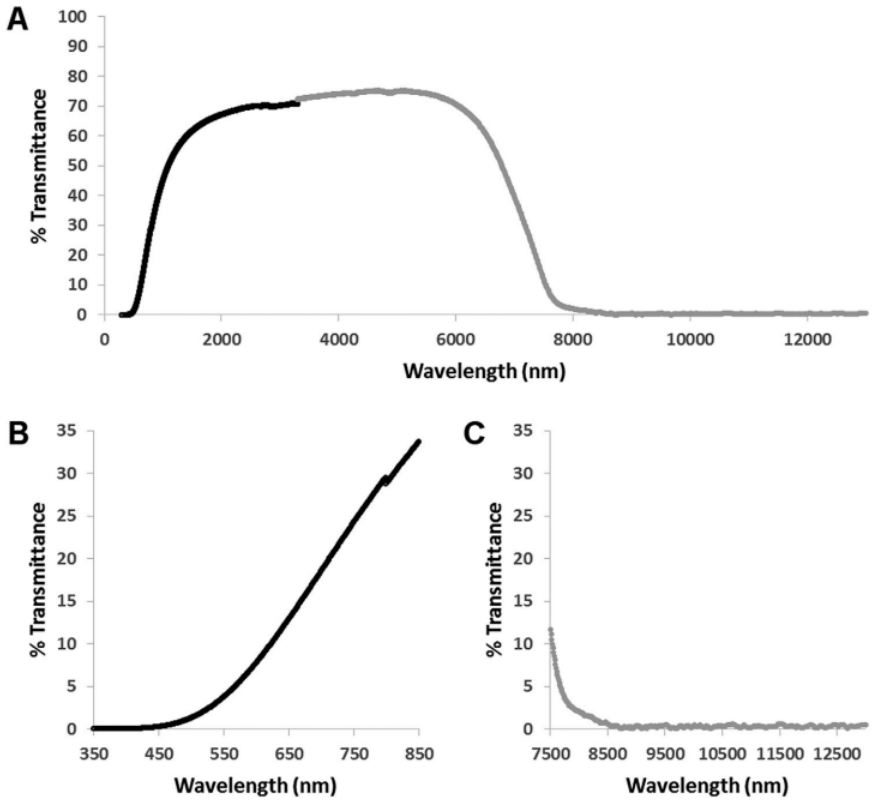

Figure 6.1. a) %Transmittance of nc-YSZ over the visible-IR spectral range. b) Blowup of %Transmittance of nc-YSZ over the vis-NIR spectral range, including the laser treatment wavelength of 810 nm. c) Blowup of %Transmittance of nc-YSZ over the IR spectral range measured by the infrared thermal camera. The black curve was measured with a Varian Cary 500 spectrophotometer (350–3,300 nm) and the gray curve was measured with an Equinox 55 FTIR spectrometer (3,300–13,000 nm).

One microliter of the overnight culture was diluted in 100 µL of fresh LB-K^+ media. As shown in Figure 6.2, agar plates were placed on a heated pad set to body-temperature in order to simulate *in vivo* conductivity and diffusivity of heat. For each experiment, 0.5µL of the diluted bacteria was seeded on agar and the nc-YSZ was placed on top. The bacteria underlying nc-YSZ was treated with selected laser parameters through the nc-YSZ. The nc-YSZ was then removed from the culture and the plate was incubated for 24 hours at 37°C.

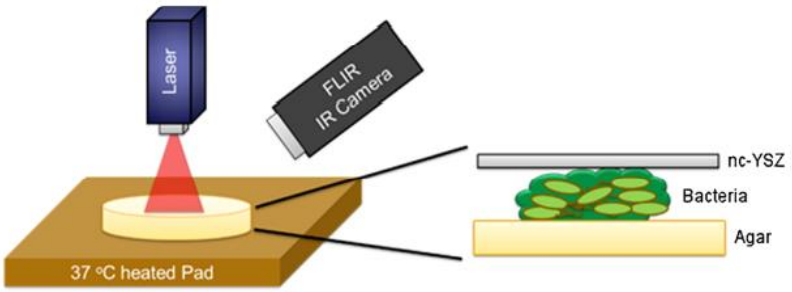

Figure 6.2. Schematic diagram for the treatment of biofilm formation under nc-YSZ with NIR laser irradiation.

Laser Device

Photo-irradiation was performed using an 810nm laser (Vari-Lase) operated in continuous (CW) and pulse (PW) modes. The laser beam was coupled into a 600 µm optical fiber to produce a 7 mm diameter ($1/e^2$) circular spot with a Gaussian profile on the nc-YSZ. The variable laser parameters were power (1–3 W corresponding to 2.6–7.8 W cm^{-2}) and pulse rate (0.3–5 Hz), and all laser treatments were 20 seconds in duration. Each combination of radiant exposure and frequency modulation was tested a total of nine times. Control cultures were treated in an identical manner to the irradiated cultures, except that the laser was not switched on.

Temperature Measurements

During laser treatment, the temperature of the surface of nc-YSZ was recorded with a non-contact infrared thermal camera (A325sc, FLIR Systems Inc., Wilsonville, OR) operating in video mode at 60 frames/s over the spectral range of 7.5–13 µm. Over this wavelength range, the nc-YSZ implant was essentially opaque (Figure 6.1(c)), and thus the IR radiation measured by the camera was primarily emitted by the upper surface of the implant, and not originating from the underside of the implant in contact with the bacteria. The video was

post-processed using ResearchIR software (FLIR ResearchIR4). According to specifications, the camera measures temperatures with a precision of 50 mK, has an accuracy of 2%, and a viewing angle of 5–60°.

Bioluminescence Imaging System

Following the 24 hours incubation, 100 µL of luciferin solution (13.4 µg of D-Luciferin potassium salt/mL; Research Products International Corp., Mt Prospect, IL) was added at room temperature to evenly cover each agar plate containing the irradiated bacteria (hereafter referred to as "sample") in preparation for bioluminescence measurements. Luciferin diffuses through the cell membrane where it reacts with the luciferase that is expressed by the E. coli to produce oxyluciferin. The decay of oxyluciferin produces a photon of light. Light emission of the bioluminescent bacteria was measured using a Macro Luminescence Dark Box (Stanford Photonics, Inc., Palo Alto, CA) in darkness with 5 seconds exposure at 2 MHz rate. ImageJ software (National Institute of Health) was used to quantify the light emission intensity at the irradiated Regions of Interest (ROIs). The ROIs encompassed a circle equal to the beam spot size on the sample (7 mm diameter). The relative luminescence unit (RLU) in the ROI was normalized with respect to the RLU outside of the ROI for each sample. The imaging procedure, acquisition parameters, and post-analysis were kept constant for all measurements.

Statistical Analysis

The difference between normalized RLU of control samples and laser-irradiated samples was statistically evaluated using analysis of variance for repeated measurements (ANOVA). When appropriate, post hoc analyses were performed with the Bonferroni's

multiple comparisons test. Thompson Tau test was used to remove outliers. All statistics were calculated using GraphPad Prism 5.01 (GraphPad Software, Inc., San Diego, CA). Changes were considered statistically significant when the P-value was less than 0.05.

Results

Figure 6.3 shows normalized RLU of biofilm after 24 hours and the average temperature (ΔT) of the upper surface of the nc-YSZ at the end of the 20 seconds laser treatment using CW laser with 1, 2, and 3 W of power and 20 seconds of exposure time to deliver a total of 20, 40, 60 J of energy, respectively. The results show that the decrease in the RLU value is statistically significant for all treated groups compared to control ($P<0.05$) and that ΔT for the CW laser powers above 1 W is above 10°C, which is considered the critical threshold for thermal damage. When CW laser is used, the reduction in biofilm formation seems to follow a linear relationship with ΔT.

Figure 6.4 shows normalized relative luminescence unit (RLU) of biofilm after 24 hours and the average temperature (ΔT) of the upper surface of the nc-YSZ at the end of the 20 seconds laser treatment using CW or PW laser with 3 W of power. Treatment with all laser parameters except for 0.5 and 0.3 Hz leads to a significant reduction of E. coli viability compared to the control group ($P<0.05$). The results indicate that the ΔT is above the 10°C critical temperature threshold for CW laser and all the PW laser settings exceeding 200 ms pulse duration and 1 Hz, when 3 W power is used.

Comparing bar #3, bar #5, bar #6, and bar #7 (frequency of 5, 1, 0.5, and 0.3 Hz, respectively) in Figure 6.4 indicates that laser treatment with higher frequency results in greater reduction in E. coli biofilm formation. Comparing bar #4 and bar #5 (1 Hz 400ms

vs. 1 Hz 200 ms) indicates that doubling the energy density per pulse and pulse duration increases the temperature of the surface of the implant by about 3°C while it has negligible effect on the reduction rate of E. coli biofilm formation.

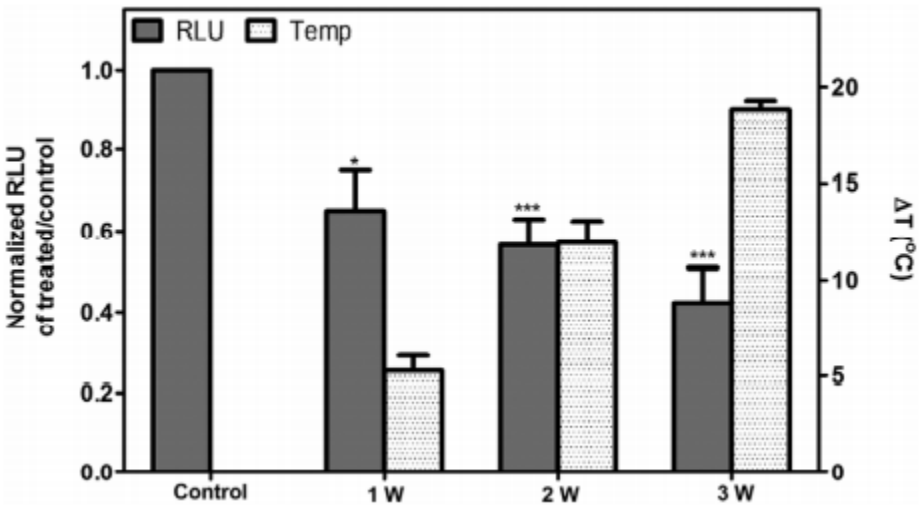

Figure 6.3. Normalized relative luminescence unit (RLU) of biofilm after 24 hours and the average temperature (ΔT) of the upper surface of the nc-YSZ at the end of the 20 seconds laser treatment using CW laser with 1, 2, and 3 W of power to deliver a total of 20, 40, 60 J of energy, respectively. Each bar represents mean ± SEM (n = 9 for each treatment). One-way ANOVA and Bonferroni's multiple comparison test *P<0.05, **P<0.01, ***P<0.001 relative to control.

The results indicate that CW laser has the higher reduction rate of E. coli biofilm formation compared to PW laser at the same power (3 W), but also causes a greater increase in temperature. In contrast to the linear relationship of temperature and reduction in biofilm formation for CW laser (Figure 6.3), there is no linear relationship between the differences in temperature change and the distinct variability of the bactericidal effects of PW laser (Figure 6.4).

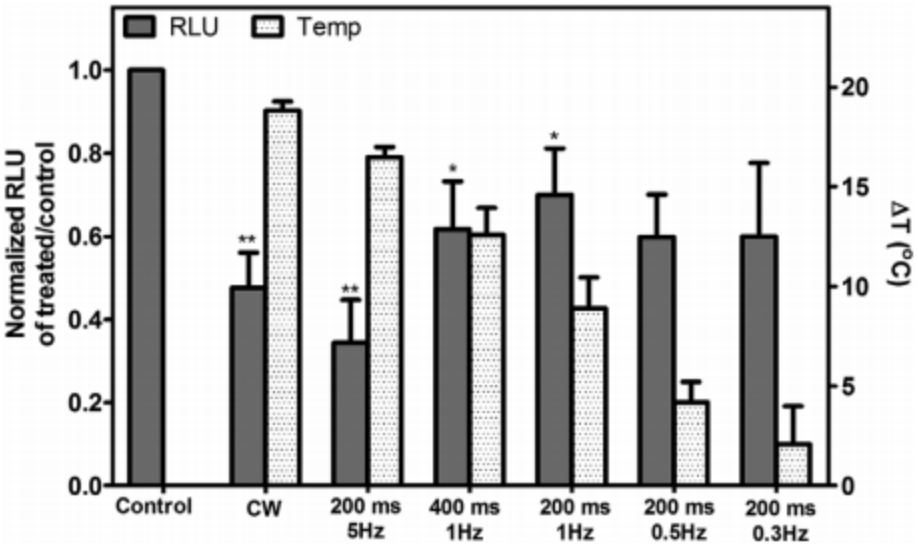

Figure 6.4. Normalized relative luminescence unit (RLU) of biofilm after 24 hours and the average temperature (ΔT) of the upper surface of the nc-YSZ at the end of the 20 seconds laser treatment using 3 W of power with CW and PW modes. Each bar represents mean ± SEM (n = 9 for each treatment). One-way ANOVA and Bonferroni's multiple comparison test *P<0.05, **P<0.01, ***P<0.001 relative to control.

Discussion

WttB provides the transparency and toughness required for clinically viable cranial implants for optical therapy and imaging of the brain [6]. Zirconia surfaces have lower bacteria adhesion compared to other implant materials [195], however, infection due to implantitis is the most significant risk factor associated with cranial implants independent of the implant material [196]. In almost all cases of cranial implant infection, it is recommended to remove and later replace the implant to avoid intradural propagation of the infection and the severe consequent risk [176]. Therefore, new treatment techniques are demanded as infections associated with cranial implants lead to chronic complications [197].

In this study, we chose 810nm as our wavelength to conduct the laser treatment of bacteria for several reasons. Various NIR diode lasers and Nd:YAG lasers are commonly and successfully used in endodontics for disinfection of almost all bacteria species. Diode lasers (λ = 810 nm) have been used to effectively reduce the viability of biofilm that adhered to zirconia dental implant surfaces. Stubinger *et al*. [198] studied the effect of diode (λ = 810 nm), CO_2 (λ = 10,600 nm), and Er:YAG laser (λ = 2,940 nm) on surface properties of yttria-stabilized tetragonal zirconia polycrystal (Y-TZP) implant surface using SEM, confocal 3D white light microscopy (CWLM), and energy-dispersive X-ray (EDX), and demonstrated that currently, diode lasers seem to be the only laser systems offering surface preservation and safety in the treatment of peri-implantitis with zirconia, while longer wavelengths did not. On the other hand, as shown in Figure 6.1(b), the %Transmittance of our nc-YSZ implant decreases for wavelengths lower than 810 nm, and thus 810nm allowed for a higher fluence to reach the bacteria through the implant, as well as surface preservation of the implant.

Nussbaum *et al*. [199] have investigated the effects of CW and frequency modulated 810 nm laser on the growth of E. coli and other bacterial species in culture previously, and found that the effect is dependent upon several factors, including bacterial species, modulation frequency, irradiance, and radiant exposure. Interestingly, both promotion and inhibition of bacterial growth rates were achieved by modulation of the laser parameters. While CW laser promoted E. coli growth regardless of radiant exposure (up to 50 J cm^{-2}, with 0.015 Wcm^{-2} irradiance), PW caused promotion and inhibition, depending on frequency and radiant exposure, but the trend was less clear. In a follow up study using

CW 810 nm laser, Nussbaum *et al*. [190] found promotion of E. coli growth similar to their previous study, but also inhibition of E. coli growth when irradiance was doubled (0.03 W cm^{-2}) and radiant exposure was sufficiently high (>30 J cm^{-2}). In our study, we observed inhibited E. coli growth for all laser parameters investigated. It should be noted, however, that while the radiant exposures reached in our study were similar to those reached by Nussbaum *et al*., the irradiance used in our study was substantially higher.

Our study further differs from these previous works due to the presence of the nc-YSZ implant overlying the bacteria during the laser treatment. As shown in Figure 6.1(b), the %Transmittance of the implant at 810 nm is ~30%, and thus only 30% of photons reach the E. coli. The remainder of the photons do not pass through the implant, and are primarily absorbed resulting in heating of the implant. Thus the observed reduction in biofilm formation may be due to direct (optical transmission through implant) or indirect (heating of implant) effects of the laser on the E. coli, or a combination of both direct and indirect effects.

To investigate these two simultaneous effects individually, we conducted an additional experiment where a 4 mm air gap was introduced between the bacteria and the implant during laser treatment. This air gap served as a thermal barrier to remove the indirect heating component, and isolate the direct optical effect on the bacterial growth. When the thermal component was removed, the statistically significant reduction in RLU of the biofilm is lost (Figure 6.5). While both laser treatments (CW, 3 W and 5 Hz, 3 W, 200 ms, bar #2 and bar #3, respectively) caused an increase in normalized RLU relative to control, this increase was not statistically significant ($P = 0.4868$). This result demonstrates

that the direct optical effect of the laser on the E. coli, alone, cannot account for the decrease in bacterial growth rate displayed in Figures 6.3 and 6.4.

Regarding the indirect effect of laser on the E. coli (i.e., heating of the implant), differences in the heat distribution of the implant must be considered. As shown in Figure 6.1(c), the implant is essentially opaque in the wavelength range measured by the thermal camera. Therefore, the temperatures reported in Figures 6.3 and 6.4 are only the temperature of the upper surface of the implant. Due to our experimental design, with the implant in physical contact with the bacteria during laser treatment (Figure 6.2), it was not possible to measure the temperature of the lower surface of the implant during the treatments. To estimate this temperature, we repeated the laser treatments on the implant in isolation in air, and measured the ΔT of both the upper and lower surfaces of the implant. We then adjusted the ΔT of the upper surface of the implant reported in Figures 6.3 and 6.4 by this ratio (Table 6.1). Laser treatments of the agar plate in isolation resulted in negligible temperature increase of the agar (data not shown), and thus the estimated temperature of the lower surface of the implant shown in Table 6.1 can be treated as an approximate temperature experienced by the E. coli in the laser treatments from Figures 6.3 and 6.4.

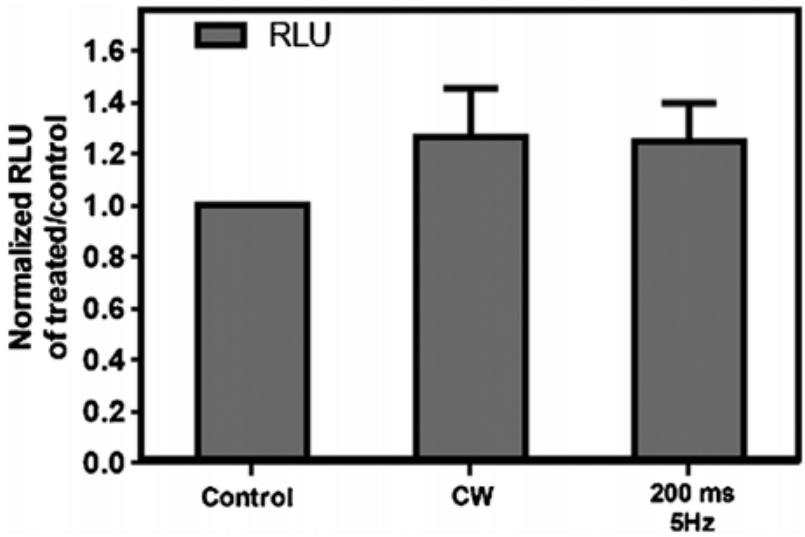

Figure 6.5. Normalized relative luminescence unit (RLU) of biofilm 24 hours after 20 seconds laser treatment using 3 W of power with CW and PW modes, with 4mm air gap between nc-YSZ and E. coli. Each bar represents mean ± SEM (n = 3 for each treatment). One-way ANOVA and Bonferroni's multiple comparison test *P<0.05, **P<0.01, ***P<0.001 relative to control.

Although there have been several *in vivo* and *in vitro* reports demonstrating the bactericidal effect of medical lasers on various strains, the underlying mechanisms of photochemical or/and photothermal effects remain controversial. Lee and Kaletunc [200] demonstrated that heating of E. coli from 55 to 70°C for 60 seconds decreases the viability significantly due to enthalpy change and irreversible damage to ribosomal subunits. Using the temperature range of 50–70°C and comparing temperature increase by CW high-power NIR laser (18–81 W cm^{-2}) and water bath, Hibst *et al*. [201] showed that inactivation of E. coli suspension is mainly driven by a thermal process. However, the estimated temperatures reached by the E. coli in our study (see Table 6.1) is much lower than the temperatures in these reports, and thus it is unlikely that the heating of the implant alone is responsible for the decrease in bacterial growth rate displayed in Figures 6.3 and 6.4.

TABLE 1. Estimated ΔT (°C) of the Lower Surface of the Implant at the End of the 20-Second Laser Treatments

	Measured ΔT (°C) of upper surface of implant	Measured ratio of ΔT (°C) of upper surface to ΔT (°C) of lower surface of implant	Estimated ΔT (°C) of lower surface of implant
CW, 1 W	5.27	2.88	1.83
CW, 2 W	11.79	2.69	4.38
CW, 3 W	18.85	2.64	7.14
5 Hz, 3 W, 200 ms	16.55	2.62	6.33
1 Hz, 3 W, 400 ms	12.62	2.74	4.60
1 Hz, 3 W, 200 ms	8.93	3.00	2.98
0.5 Hz, 3 W, 200 ms	4.17	3.11	1.34
0.3 Hz, 3 W, 200 ms	2.06	2.83	0.73

As neither a direct optical effect (Figure 6.5), nor an indirect thermal effect (Table 6.1) with the fluences and estimated temperatures reached in our study are alone sufficient to explain the observed inhibition in E. coli growth rate, it is possible that the combination of these effects is responsible. Lubart *et al*. [202] has previously suggested reactive oxygen species (ROS) generation as a mechanism for phototoxic effect of NIR light, while Nandakumar *et al*. [203] have reported that the bactericidal effect of laser is due to a reduction in ATP production which could in turn be due to damage of bacterial metabolic processes such as cellular respiration. While our results in Figure 6.5 showed that the isolated direct optical effect of the laser used in our study did not cause inhibition of the E. coli growth rate, perhaps the increased temperature of the E. coli, due to the indirect effect of the laser heating the implant, increases the susceptibility of the bacteria to these optical damage mechanisms. This possible explanation is speculative, and will require further study to determine the effect of E. coli temperature on the effectiveness of optical bactericidal treatments.

Further studies are essential to realize the potential of using lasers to reduce the formation of bacterial biofilm under the WttB *in vivo* due to differences in geometry, and optical and thermal properties of an *in vivo* model in comparison with the *in vitro* model

used in this study. For example, one of the differences of an *in vivo* model is that the bacterial biofilm will have lower local temperatures than our *in vitro* model, due to the presence of corticospinal fluid (CSF) that can act as a thermal barrier to the brain. Moreover, the distance between the brain and the inner surface of the skull mapped by Fournier *et al*. [204] ranges from 0.4 to 6.7 mm. Therefore, depending on the actual location of the implant, this distance has to be considered in planning treatment. In addition, low-level laser therapy (LLLT) using 810 nm lasers has been shown to significantly improve the neurobehavioral performance of mice after closed head traumatic brain injury (TBI) [205]. Therefore, with careful choice of 810 nm laser parameters, treatment of biofilm formation can be performed along with LLLT treatment of TBI. Finally, although the estimated temperature reached by the bacteria underlying the implant is below the critical threshold of 10°C, the temperature of the upper surface of the implant was unacceptably high for several of the laser parameters investigated in this study. Further studies will be needed to investigate methods of mitigating this high temperature during laser treatment, such as cryogenic cooling methods [206].

Conclusions

In conclusion, our results show that E. coli biofilm formation across the thickness of the nc-YSZ implant can be disrupted using NIR laser treatment. The results of this *in vitro* study suggest that using nc-YSZ as a cranial implant *in vivo* may also allow for local, noninvasive, chronic treatment of the formation of biofilm on the inner surface of the cranial implant, without inducing thermal damage to the underlying host tissue, when

appropriate laser parameters are used. Further *in vivo* studies are necessary to investigate the efficacy of biofilm inhibition and lack of thermal damage to peri-implant tissue *in situ*.

Citation: The work presented in this chapter was published in *Lasers in Surgery and Medicine* [11]:

> Damestani Y, De Howitt N, Halaney DL, Garay JE, Aguilar G. Evaluation of laser bacterial anti-fouling of transparent nanocrystalline yttria-stabilized-zirconia cranial implant. *Lasers in Surgery and Medicine* 48:782-789 (2016).

Acknowledgments

I would like to acknowledge the contribution of my co-authors to this work: Yasaman Damestani, Natalie De Hewitt, Javier E. Garay, and Guillermo Aguilar. This study was supported, in part, by the National Science Foundation (NSF) award no. 1547014 to GA and JEG. The authors would like to acknowledge Dr. Yasuhiro Kodera for fabricating the YSZ samples.

Chapter 7. Characterization of Ageing Resistant Transparent Nanocrystalline Yttria-Stabilized Zirconia Implants

Background

Polycrystalline zirconia-based ceramics have become the focus of recent investigations because of their unique combination of properties. Their high hardness and chemical inertness (high temperature stability and corrosion resistance) make them important target materials for various applications. Well-proven biocompatibility, low thermal conductivity, and high oxygen diffusivity [41] have made zirconia-based ceramics a favorable option for biomedical applications. By decreasing the grain size of the polycrystalline ceramics to nanoscale, novel characteristics such as high density (low porosity), transparency/translucency, and high refractive index and Abbe number have been reported [39, 207-210].

Recently, we have investigated the application of transparent nanocrystalline yttria-stabilized zirconia (nc-YSZ) ceramics as a biomedical transparent cranial implant, referred to in the literature as "Window to the Brain" (WttB) implant. The concept is illustrated in Figure 7.1. These transparent implants aim to provide chronic optical access to the brain [7, 61, 166, 211-213] to facilitate the diagnosis and treatment of neurological diseases [6]. A recent study also demonstrated the ability of this implant to improve ultrasound imaging of the brain compared to imaging through skull [43]. The transparency of the nc-YSZ is achieved by using ultra-fine yttria-stabilized zirconia (YSZ) powder and an innovative ceramic processing method, current-activated pressure-assisted densification (CAPAD), leading to transparent nc- YSZ ceramics [38]. CAPAD enables reduction of the number of

pores as well as reduction of their dimensions to nanometric scale and at these length scales, porosity is sufficiently small to minimize scattering in the spectral range of interest for medical imaging and laser therapies of the brain [39].

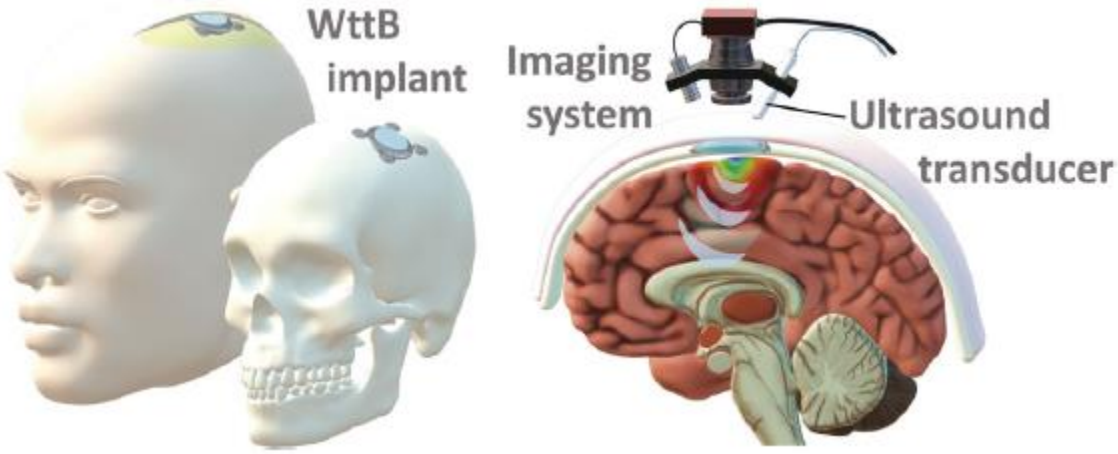

Figure 7.1. Illustration of the Window to the Brain cranial implant concept. The implant will be attached to the skull beneath the scalp, to allow for optical and ultrasonic transmission to and from the brain.

Although zirconia-based implants have been known for their excellent mechanical properties, the *in vivo* application was found to be affected by long-term failures for some samples with micrometric grain sizes, due to low temperature degradation (LTD). By contrast, YSZ with nanometric size grains are significantly more resistant to LTD [207]. LTD is due to a crystal phase transformation from tetragonal to monoclinic, which is associated with a volume increase of about 4–6% [214]. This expansion induces localized compressive stresses and eventually microcracks around the transformed zirconia particles [215]. These microcracks propagate through the sample bulk, and internal defects such as pores and crack surfaces [216]. Under such conditions, the material loses its cohesion and mechanical properties. Therefore, small amounts of porosity contribute to enhance the

nucleation and propagation of the monoclinic phase, so the use of very dense implants is required to reduce the transformation rate [215, 217].

As a modest amount of transformation can change optical characteristics such as transparency, in this chapter we investigated the optical properties of transparent nc-YSZ ceramics with different stabilizer contents (yttria dopant levels) of 3, 6, and 8 mol% before and after extended accelerated ageing treatments. Further, because mechanical properties become compromised when LTD occurs, we also compared the hardness of our samples before and after the accelerated ageing treatments. The treatment simulates *in vivo* ageing, according to the ISO 13356:2008 recommendations [216, 218] (i.e., autoclave processing at 134°C at a water partial pressure of 2–3 bar).

To our knowledge, this is the first study to compare the LTD of transparent nanocrystalline YSZ with differing stabilizer content (3, 6, and 8 mol% yttria). Most studies conducted on LTD of zirconia-ceramic have involved opaque micrometric-grained YSZ. The objective of this chapter is to assess the LTD of nc-YSZ through simulated ageing protocols, to model how the WttB implant will perform optically and mechanically over decades of ageing in the body.

Methods

Implant Fabrication and Preparation

Implant fabrication and preparation conducted for this chapter differed from the methods described in Chapter 2 (page 8). Commercial (Tosoh USA Inc., Grove City, OH) nanocrystalline 3YSZ, 6YSZ, and 8YSZ powders (respectively doped with 6, 12, and 16 mol% $YO_{1.5}$ nc-YSZ) with reported crystallite sizes of 55 nm, were densified via the

current activated pressure assisted (CAPAD) technique, to produce transparent yttria-stabilized zirconia ceramics [5]. In the literature, this technique is often called spark plasma sintering (SPS). We used CAPAD here to emphasize the fact that it is complimentary contributions of the current and an applied pressure that makes it successful [5]. During the fabrication processes of all samples for this work, 1.5000 g ± 0.0001 g of starting powder was poured into a graphite die of inner diameter measuring 19 mm, and secured between two plungers with the same outer diameter. The die, plungers, and powder assemblies were placed into the CAPAD apparatus and secured between two graphite spacers and copper electrodes, all enclosed within a vacuum chamber. A vacuum of 1×10^{-3} Torr was attained in all cases.

All powder compacts were prepressed to a maximum load of 30 kN, applied linearly, to produce a nominal compressive pressure of 106 MPa on the sample, and held for 2 min to achieve a green body of appreciable density. The load was then released, and the green body subjected to another uniaxial compressive stress of 106 MPa over a 3-min interval. Once the set-point temperature was reached, a second load ramp (kN min^{-1}) was applied. This ramp bringing the uniaxial pressuring on the sample up to 141 MPa, was maintained for 10 min, the duration of processing, and thereafter linearly released. In addition to the aforementioned load parameters, the green pellet was simultaneously heated to high temperature by applying electric current through the die and plunger assembly, consequently creating joule heating. All samples were processed at 1200°C, with an average heating rate of approximately 160°C/min, from room temperature, and held for 10 min.

The density of the samples was measured using the Archimedes method, and the ASTM standard designated B962-13 was followed [219]. Grain size measurements of the bulk sample made from fracture surfaces were evaluated using SEM.

The samples thicknesses were reduced by polishing with 30-micron diamond slurry on an automatic polisher (Pace Technologies, Tucson, AZ). The two faces were then polished using progressively finer abrasives (from 30 μm diamond slurry down to 0.2 μm colloidal silica slurry) to reduce light scattering by the implant surfaces and thus increase transparency as well as to create a uniform surface area between different samples. As ageing begins at surface and propagates into bulk, surface area is an important factor to control between samples when comparing ageing results. After preparation process, the polished samples underwent ageing tests.

Ageing Test

The test for simulating *in vivo* ageing, per the ISO 13356:2008 recommendations [220], uses hydrothermal treatment at 134°C, at a steam partial pressure of 2–3 bar which is known as autoclave processing. As seen in Figure 7.2, the samples were placed in a steel pressure chamber, and saturated high-pressure steam was generated by a boiler and sent to the sample chamber through an electronic valve. An electric heating jacket surrounded the chamber to prevent steam condensation and stabilize the temperature at 134°C. Two K-type thermocouples were used to measure the sample chamber and the boiler temperature, and an electronic pressure sensor was connected to the pressure chamber. A microcomputer (Raspberry Pie 3) coupled to the sensors controlled the heating jacket power and the valve status. The ageing treatments were performed in cycles of 5, 10, 10, 25, 25, 25 hr, for a

total of 100 hr for each sample. At the end of the treatments, the samples were cooled down to room temperature and dried.

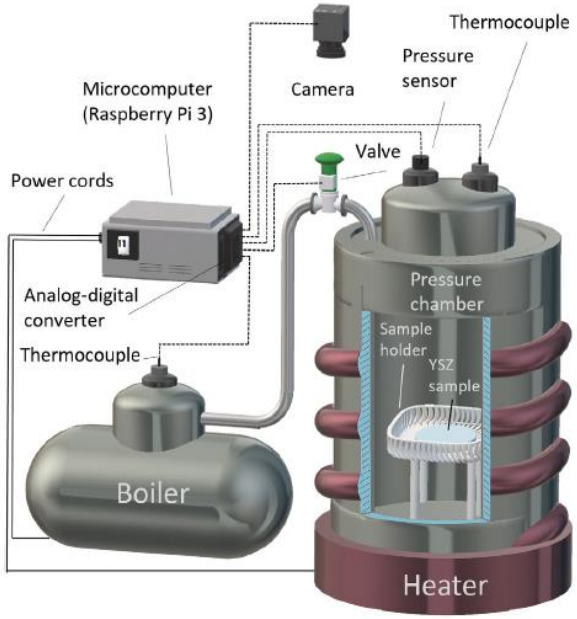

Figure 7.2. Hydrothermal treatment experimental setup schematic. Samples were placed inside a pressure chamber. Thermocouples and a pressure sensor coupled to a microcomputer maintained the temperature and pressure at 134°C and 2–3 bar.

Material Characterization

X-ray diffraction (XRD) analysis was used to detect any phase transformation due to the ageing treatments (Figure 7.3(a)). Due to its simplicity, this technique has been considered as a first step to investigate the ageing sensitivity of a particular zirconia. However, this technique suffers some limitations, such as poor precision during the first stages of ageing (which have also been reported with a much higher sensitivity using grazing incidence angles of 1–5° (2θ)) [216, 221] as well as the absence of local information on ageing processes [222]. Data were acquired on an Xray diffractometer (PANalytical Empyrean

Series 2) using a step size of 0.03° (2θ) and an acquisition time of 5 s per step. Various (hkl) planes were used to evaluate crystal structures, including cubic (111), tetragonal (101), and monoclinic ($\bar{1}11$ $\bar{1}11$ and 111) peaks at 30.2°, 30.2°, 28.2°, and 31.5° (2θ), respectively. It must be noted that the distance between cubic and tetragonal peaks is smaller than the width of the peaks which makes them indistinguishable and detected at the same angle (30.2°).

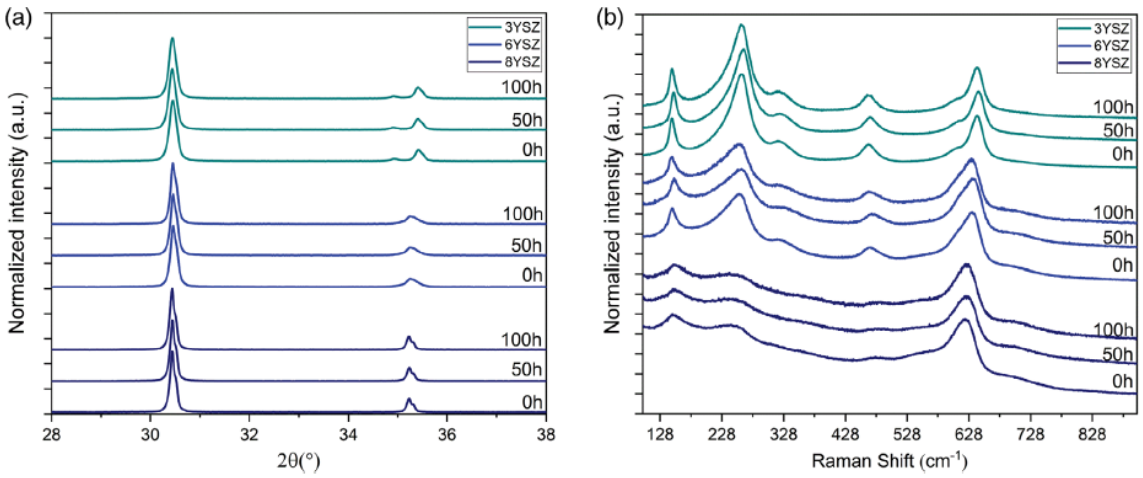

Figure 7.3. For 3YSZ, 6YSZ, and 8YSZ, XRD diffractogram a) and micro-Raman patterns b) obtained after up to 100 hr of hydrothermal treatment at 134°C. XRD, X-ray diffraction; YSZ, yttria-stabilized zirconia.

Raman spectroscopy was additionally performed to investigate the impact of ageing on the phase transformation (Figure 7.3(b)). Raman spectroscopy has been reported to show higher sensitivity to the smaller trace of monoclinic phase [223], associated with a higher lateral resolution than XRD [208]. Micro-Raman spectrum were recorded by using a spectrometer (Horiba's LabRam) with acquisition time of 60 s. The incident laser light with a wavelength of 532 nm was focused on the sample within a spot of 10 μm in diameter.

Presence of monoclinic phase was assessed by comparing monoclinic doublet at 179 and 190 cm^{-1} in the Raman spectra.

Optical Characterization

To qualitatively compare the transparency of the densified and polished 3YSZ, 6YSZ, and 8YSZ samples, photographs of a NBS 1963A resolution target (18 cycle/mm target, each black line width is 27.78 μm) through the ceramics were taken (Figure 7.4). For quantitative comparison, optical transmittance of the nc-YSZ samples were evaluated by optical spectrometry in visible and near-infrared light. The optical transmittance was measured using a white light source (HL2000 FHSA, Ocean Optics, FL) and a spectrometer (SD2000, Ocean Optics, FL) in the 500–1000 nm wavelength range. The sampling system used for specular transmittance consists of a rail coupled with two fiber holders including collimating lenses (MP-74-UV, Ocean Optics, FL) with a wavelength range of 185–2500 nm. A space for placing the samples was incorporated on one of the fiber holders. After placing the sample, the fiber holders were fixed by screws to mitigate the effects of ambient light. A couple of multimodal optical fibers (P400-2-VIS-NIR, Ocean Optics, FL) were connected from the light source to the fiber holder and from the other fiber holder to the spectrometer. The spectra were acquired as an average of 10 measurements, with integration time of 100 ms.

Figure 7.4. a) Photographs of an NBS 1963A resolution target, b) through the 3YSZ, c) 6YSZ, d) and 8YSZ samples. The resolutions shown are the 18 cycle/mm target (each black line width is 27.78 μm). NBS, National Bureau of Standards; YSZ, yttria-stabilized zirconia.

The normalized transmittance was calculated considering the ratio of light transmitted through the sample to the total light incident upon that sample [Equation (1)].

$$T(\lambda) = \frac{S(\lambda)-D}{I(\lambda)-D} \quad (1)$$

where T is transmittance, S(λ) is the measured spectral intensity, I(λ) is the total light incident, and D represents the reference in dark environment.

Mechanical Characterization

To compare the mechanical properties between the pristine samples and aged samples, indentation tests were performed using a micro Vickers hardness tester (900-391A, Phase II Plus, NJ). The indentation was performed using loading force of 4.9 N and 15 s duration. The instrument was recalibrated before and after testing, by performing a series of indentations on a certified steel reference sample. The average value and SD of 10 indentations were calculated for each sample before and after the ageing treatments.

Results

Densified Samples

The density of the CAPAD processed samples (discs of 1 mm thickness and 19 mm diameter) were 99.8%, 99.9%, and 99.9% for the 3YSZ, 6YSZ, and 8YSZ, respectively. Grain size measurements of the bulk samples were made from fracture surface measurements of SEM micrographs and showed an average grain size (AGS) of 147 ± 45 nm across all compositions. The polished sample thicknesses were 610 ± 1 μm, 584 ± 1 μm, and 601 ± 1 μm for 3YSZ, 6YSZ, and 8YSZ, respectively.

Material Characterization

Phase transformation to monoclinic was assessed with XRD and micro-Raman Spectroscopy. XRD patterns of samples before and after 50 and 100 hr of accelerated ageing via hydrothermal treatment are shown in Figure 7.3(a). XRD patterns in the range of 28°–38° are shown in Figure 7.2(a). Only cubic (111) and tetragonal (101) (both peaks inseparably appeared at 30.2°) can be seen in the XRD patterns, confirming that there is no monoclinic phase present. The peaks and patterns remained the same for all samples following ageing treatments, indicating that no phase transformation occurred. In Figure 7.3(b), the comparison of micro-Raman patterns in the 100–900 cm^{-1} region shows stability of tetragonal and cubic phases after the treatments, further confirming that no phase transformation to monoclinic (doublet at 179 and 190 cm^{-1}) occurred.

Optical Characterization

Figure 7.4 shows images of a National Bureau of Standards resolution target imaged through the transparent nc-YSZ samples. All of the samples clearly show the highest

resolution (18 cycles/mm) on the resolution target when transmitted light is observed through them. As seen in Figure 7.3, all the samples transmit light and appear as different shades of orange.

To assess any change in optical properties due to the accelerated ageing hydrothermal treatment, optical transmittance of the transparent samples was measured over the wavelength range of 500–1000 nm at baseline and after 50 and 100 hr of ageing. Figure 7.5 presents the normalized optical transmittance, T(λ), for both pristine and aged 3YSZ, 6YSZ, and 8YSZ samples. As shown in the figure, the transmittance curves for all three samples have approximately the same trend. However, for any given wavelength, the transmittance increases as the yttria content is increased. In addition, the samples transmit a higher percentage of light as the wavelength of the incident light is increased. These results are consistent with our previous measurements, showing relatively low transmission in the blue-green end of spectrum caused by absorption of oxygen vacancy related defects [38]. The insets in Figure 7.4 show the maximum difference between the transmittance curves between pristine and aged samples. The changes in transmittance values after the treatments (compared to the pristine samples), were less than 3%.

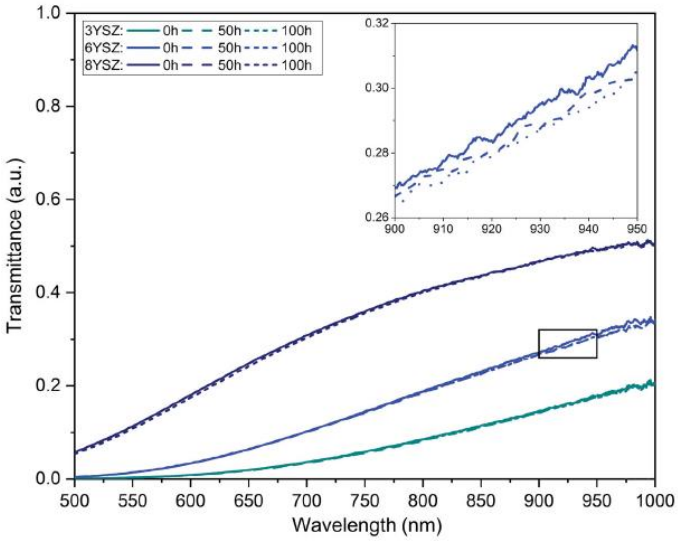

Figure 7.5. Mean T(λ) values obtained at wavelength range of 500–1000 nm to compare the transmittance values of various nc-YSZ samples (3YSZ, 6YSZ, and 8YSZ) before and after ageing. The inset shows the maximum difference in optical properties curves between the pristine and aged samples. YSZ, yttria-stabilized zirconia.

Hardness Characterization

As the phase transformation to monoclinic compromises mechanical properties, we compared the hardness of 3YSZ, 6YSZ, and 8YSZ before and after ageing. The averaged results and the standard deviations calculated from 10 indentation experiments per sample are summarized in Table 1 as a function of ageing treatment time and yttria content. For the pristine samples, the highest hardness value was obtained for 3YSZ sample. The 6YSZ and 8YSZ samples had slightly lower hardness values (6.64% and 4.26%, respectively). For 3YSZ and 8YSZ samples, changes in hardness were not significant (paired two-tail t test), with t values greater than 0.05. For the case of 6YSZ, changes in hardness between pristine sample and sample after 50 or 100 hr of ageing treatment was found to be

significant (t = 0.00094 and 0.0037, respectively), although these changes were small (less than 2% increase in hardness compared to pristine sample).

	Hardness (GPa)		
Sample	Pristine	After 50 hr	After 100 hr
3YSZ	13.84 ± 0.20	13.80 ± 0.16	13.71 ± 0.21
6YSZ	12.92 ± 0.10	13.16 ± 0.11	13.13 ± 0.13
8YSZ	13.22 ± 0.12	13.16 ± 0.18	13.17 ± 0.13

Table 1. Hardness of the pristine and aged samples. Data is given with SD (statistical processing of multiple indentations for each sample). Abbreviation: YSZ, yttria-stabilized zirconia.

Discussion

The transparent nc-YSZ ceramics evaluated in this study show promise for medical and nonmedical applications. Previously, we have investigated the application of 8YSZ for creating transparent cranial implants. By performing biocompatibility tests and brain imaging studies, we have demonstrated the feasibility of this application [6, 7, 37, 43, 61, 166, 211-213, 224, 225]. Phase transformation (ageing) resistance and the effect of hydrothermal treatment on optical and mechanical properties of the ceramics are crucial to understand for any medical or nonmedical application of the transparent nc-YSZ ceramics. Recently, fabrication of translucent and transparent YSZ with grain size on the microscale and nanoscale have been reported [39, 210, 224, 226]. However, a thorough investigation on preparation and evaluation of LTD and its influence on mechanical and optical properties in transparent nanocrystalline stabilized zirconia ceramics with various yttria dopant levels of 3, 6, and 8 mol% have not been reported.

Ageing caused by the transition of the tetragonal-to-monoclinic phase represents a common problem of zirconia ceramics stabilized by acceptor dopants. The process is triggered by the hydroxyl groups (with bound –OH) which can penetrate into the lattice over time through oxygen vacancies resulting from the doping process [38]. Degradation due to this transformation has been known to propagate gradually to the bulk of the material [214]. Unlike the porosity of micrometric-structured stabilized zirconia ceramics, the nanoscale grain and high densities of our nc-YSZ have proven highly effective in preventing the transformation, as shown by our results here as well as others [227, 228].

Considering the self-ionization of water, a greater number of OH^- ions produced at higher temperatures and pressures can accelerate the LTD process [229]. Accelerated ageing treatment has been a common method to evaluate zirconia ceramic LTD. Chevalier and Gremillard's evaluation based on actual observations of zirconia femoral heads implanted *in vivo* for 4 and 8 years, showed that 1 hr of autoclave treatment at 134°C had a similar effect as a 3–4 years *in vivo* ageing [216]. They proved that the ISO standard recommendations for determining the long-term duration of prosthetic zirconia were inadequate [230] and the ISO recommendation was revised according to Gremillard's suggestions [220]. Advances in grain size reduction resulted in YSZ ceramics that are more resistant against LTD, and for this reason Sanon *et al*. recommended to increase the ageing test up to 100 hr for better observation of the LTD process. Our simulation was extended to 100 hr following Sanon's proposal [231]. Given the very high LTD resistance that nanostructured YSZ ceramics have shown compared to conventional microcrystalline YSZ

ceramics, a new accelerated ageing simulation protocol will be needed to characterize any transformation and degradation which may occur in these samples [231].

We have shown our 3YSZ, 6YSZ, and 8YSZ samples with AGS of 147 nm ± 45 nm, prepared using CAPAD, satisfy the requirements for long-term performance as an optical implant. Indeed, for all the investigated samples the increase in monoclinic phase content was below the XRD and micro-Raman detection range, in agreement with our previous findings [224]. The ageing tests showed the ability of these materials to withstand common sterilization treatments as well. LTD resistant YSZ samples have been reported recently, however they are produced using the conventional zirconia doped 3 at% of yttria [228, 232], often co-doped with other cations [233]. In these studies, the samples were sintered by pressureless techniques with resulting grain sizes of hundreds of nanometers [226, 232, 233]. YSZ samples prepared by CAPAD (or SPS) with nanometric grain size have also been shown by others to have very high LTD resistance and density [210, 227]. It should also be noted that YSZ samples with similar grain size, mechanical properties, and aging resistance have been produced using more conventional multistep sintering methods [228].

Optical characterization of the pristine samples shows the optical transmittance is highly dependent on the yttria dopant level. Higher transmittance was found for the sample Fs with higher yttria dopant content, although the spectral behaviors are similar for the three sample types (3YSZ, 6YSZ, and 8YSZ). This indicates the increase in the yttria content which resulted in higher cubic content favors increased transparency [39]. Decreased symmetry of the tetragonal structure causes asymmetric scattering in the 3YSZ

sample while the more isotropic structure in the 6YSZ and 8YSZ reduces light scattering [39, 192]. This difference in crystal structure is the likely cause of the differences in light transmittance. 8YSZ is the most transparent sample, allowing the transmittance of light in a wider wavelength range, starting on 610 nm. The 3YSZ sample is the least transparent. In addition, we have shown the optical property values have a maximum change of 3% after 100 hr of the hydrothermal treatments in wavelength range of 500–1000 nm for all the samples. This small change is unlikely to be caused by surface crystal phase changes, and may instead be due to measurement error.

The hardness of our nanometric YSZ samples, both pristine and aged, compare well with similar YSZ materials reported in the literature [227, 234]. A reduced yttrium (~3 mol% yttria) content is generally associated with better mechanical properties. In samples with higher yttria dopant contents, the hardness values are lower, whereas, the transparency is notably increased. The 3YSZ sample (tetragonal structure) showed the best mechanical hardness and 6YSZ and 8YSZ showed slightly lower hardness, due to higher yttria dopant content which results in the presence of a mixed tetragonal-cubic structure (6YSZ) and cubic structure (8YSZ). The changes in the averaged hardness values after the treatments for the 3YSZ and 8YSZ were not significant (paired two-tailed t test) while a slight increase (<2%) was found for the hardness of 6YSZ after ageing treatment. Increased hardness due to ageing was an unexpected result, and may be due to measurement error of the hardness of pristine 6YSZ, which was notably lower than the hardness of the other pristine sample compositions.

Conclusions

The combination of YSZ nanopowder and CAPAD offers a procedure for the preparation of high-density, transparent implant material suitable for the production of WttB cranial prosthesis. All the samples with yttria dopant levels ranging between 3 and 8 mol%, showed a strong resistance to LTD due to nanostructuring, as demonstrated by extended ageing simulations performed following the ISO 13356:2008. The samples were able to sustain tens of hours of treatments at 134°C; conditions equivalent to many decades of ageing *in vivo*. A higher yttria dopant level (8YSZ) showed higher transmittance but presented slightly lower hardness. Finally, comparison of % monoclinic transformation, optical transparency, and mechanical properties of nc-YSZ samples at baseline and following up to 100 hr hydrothermal treatments shows our implant can withstand the extended ageing treatment.

Citation: The work presented in this chapter was published in the *Journal of Biomedical Materials Research Part B: Applied Biomaterials* [12]:

> Davoodzadeh N, Cano-Velazquez MS, Halaney DL, Sabzeghabae A, Uahengo G, Garay JE, Aguilar G. Characterization of ageing resistant transparent nanocrystalline yttria-stabilized zirconia implants. *Journal of Biomedical Materials Research Part B: Applied Biomaterials* 108(3):709-716 (2020).

Acknowledgments

I would like to acknowledge the contribution of my co-authors to this work: Nami Davoodzadeh, Mildred S. Cano-Velázquez, Ariana Sabzeghabae, Gottlieb Uahengo, Javier E. Garay, and Guillermo Aguilar. This work was supported by NSF awards #1545852 and #1547014 to GA and JEG and “Beca Mixta” from National Council of Science and

Technology of Mexico (CONACYT) (741249). The authors would like to acknowledge Gottlieb Uahengo for fabricating the YSZ samples.

Chapter 8. Group Refractive Index of Nanocrystalline Yttria-Stabilized Zirconia Transparent Cranial Implants

Background

Neurosurgeries often involve craniectomy (removal of a portion of the cranial bone) to gain access to the brain for therapy, followed by the placement of a cranial implant to replace the excised bone. Cranial implants are normally made from a variety of materials including metals, polymers and ceramics, and provide mechanical protection to the underlying brain tissue [1]. To our knowledge, current cranial implants available to patients lack optical transparency which could allow for brain optical imaging or therapy without implant removal or additional open skull procedures. We recently introduced a novel optically transparent cranial implant made from a biocompatible ceramic, nanocrystalline Yttria-Stabilized Zirconia (nc-YSZ), which we refer to as the "Window to the Brain" (WttB) implant [7, 9, 10, 12]. We have demonstrated chronic brain imaging across this implant *in vivo* using optical coherence tomography (OCT) [8]. OCT is an imaging technique based on broadband near-infrared light which can penetrate into scattering media such as brain tissue underlying the WttB implant. However, optical properties of these transparent cranial implants are neither completely characterized nor completely understood. Fundamental optical properties of the implant such as the group refractive index and chromatic dispersion are important to consider when planning or designing time-based and/or multispectral imaging strategies across the window, and for correct interpretation of recorded brain images. The group refractive index describes the speed at which a light wavepacket travels through the window, and is important to consider when focusing light

across the window as well as when interpreting OCT images, where on-axis dimensions of reconstructed images are determined by time-of-flight of the OCT wavepacket. Chromatic dispersion also effects the quality of images recorded with broadband light sources like the ones used to record OCT images. Characterizing variation of group refractive index and chromatic dispersion will allow development of dispersion compensation techniques for obtaining higher quality OCT images. Furthermore, design of other multispectral imaging strategies that utilize cranial implant windows will be impacted by the group refractive index and chromatic dispersion.

Methods to measure refractive index include non-interferometric methods and interferometric methods. Non-interferometric methods include the use of index matching liquids, and refractometers. Index matching liquids are not ideal for determining the refractive index of nc-YSZ, which has lower transparency in the visible range and enhanced transparency in the near-infrared, because these liquids are typically designed for visible wavelengths and require switching the liquid until a near match is found, giving a rough estimate of the index of nc-YSZ. Refractometers require the thickness to be known at each location under interrogation, and due to the thin nature of our samples, this thickness measurement must be very precise to yield an accurate index measurement. Because the samples we are measuring do not have perfect flatness nor perfectly uniform thickness, we needed a method which can simultaneously measure thickness and group refractive index at each location under interrogation on the sample. Of the interferometric methods available to measure refractive index, OCT is very precise. The measurement is taken over many wavelengths, providing a very good phase-sensitive estimate of the group

refractive index. Other interferometric methods are appropriate for highly transparent materials, whereas materials like transparent nc-YSZ exhibit some light scattering. This scattering is enough to introduce artifacts in other methodologies. OCT has been used to measure the group refractive index of tissue [235], which is highly scattering, and thus is capable of accurately assessing the group refractive index of nc-YSZ. There are no other methods for these materials as precise as OCT, but because OCT is a broadband technique, we are able to assess group delay and group refractive index rather than phase index. Because OCT brain imaging is one of the most applicable imaging techniques for use across the Window to the Brain implant, group index over OCT wavelengths is highly applicable to envisioned clinical applications for the implant.

In this chapter, we measured optical properties of transparent cranial implants using a swept source OCT system to characterize the group refractive index of the nc-YSZ window, over a narrow range of temperatures at which the implant may be used during imaging or therapy, ranging from room temperature to the point where thermal tissue damage begins to occur (20°C – 43°C) [236]. Additionally, chromatic dispersion of the OCT pulse was assessed.

Methods

Implant Fabrication and Preparation

Implant fabrication and preparation was conducted as described in Chapter 2 (page 8). A photograph of the nc-YSZ is shown in Figure 8.1(a).

OCT Imaging

The OCT system used in this study utilized a swept-source, mode-locked laser (Axsun, Billerica, MA) with central wavelength emission at 1300 nm, 136 nm sweep and an A-scan-rate of 100 kHz (Figure 8.1(b)). The swept source output was coupled into a fiber-optic (SMF-28) Mach-Zehnder interferometer with pathlength and dispersion matched sample and reference arms. Sample path light was collimated (RC04, Thorlabs) and directed onto two galvanometer mirrors (GVS012, Thor Labs Inc) positioned in a telecentric configuration with an aspheric ZnSe scanning lens (AR112-ZC-XWL-25-25, ISP Optics). An identical ZnSe lens was used in the reference path for dispersion compensation. Light backscattered from the sample and reflected from the reference mirror interfered and directed onto balanced detectors (BD) to obtain one-dimensional interferogram A-scans. Each one-dimensional scan (or A-line) collected contained 1472 points (or pixels) to complete the interferogram. A pixel in the depth dimension was determined to correspond to a real thickness in air of 6.19 μm. Orthogonal scanning galvanometer mirrors in the scan head allowed for recording two-dimensional images (or B-scans where each B-scan consisted of 512 A-lines).

Experimental Setup for Temperature-Dependent Measurements

The OCT imaging head was placed over a glass dish containing a 100 μm coverslip spacer with hole in the center and secured in place with epoxy. The refractive index of the coverslip spacer (made of borosilicate glass) is 1.504 at central wavelength of OCT at 1.31 μm. The glass dish was placed atop a temperature adjustable plate on a tilt and z-stage, allowing for the dish to be positioned with normal incidence to the OCT beam (Figure

8.1(c)). A baseline image was acquired, showing the vertical height of the dish and spacer when imaged in air (Figure 8.2(a)). In Figure 8.2(a), the dish surface appears displaced when imaged through the coverslip spacer compared to when imaged through the hole in the center of the spacer, due to the refraction of light in the coverslip spacer (red arrows), although this surface is in fact continuous and flat. Next, the nc-YSZ sample was carefully placed atop the spacer, and water was slowly added to submerge the sample. A thermocouple was used to measure the water temperature as 20.8°C. A room temperature (RT) image was acquired, showing the apparent displacement of the spacer and dish due to non-unity group refractive index of water (at locations F & G) or due to the nc-YSZ and water (at locations A, B, C, D & E) (Figure 8.2(b)). Weight of the water also caused a real downward displacement of the dish due to compression of the temperature adjustable plate. The water temperature was increased by heating the temperature adjustable plate to 38°C (near body temperature). After the temperature stabilized, an OCT image was acquired. Displacement in the image was observed to change relative to the RT image due to several factors. The increased temperature changes the group refractive index of the water, and potentially of the nc-YSZ. Evaporation of the water during the heating to 38°C decreased the height of the air-water interface as well as decreasing the real displacement of the temperature adjustable plate via compression. The temperature adjustable plate also undergoes thermal expansion during heating, translating the dish upwards in the image. Finally, the temperature was increased further, to 43.2°C. This temperature is near the upper limit with which the implant should be used *in vivo*. Higher temperatures were not attempted, as turbulence of the water became a confounding factor at temperatures above

45°C. Similar to the case with 38°C, the displacement in the image was observed to change relative to images recorded at lower temperatures due to the same factors discussed above.

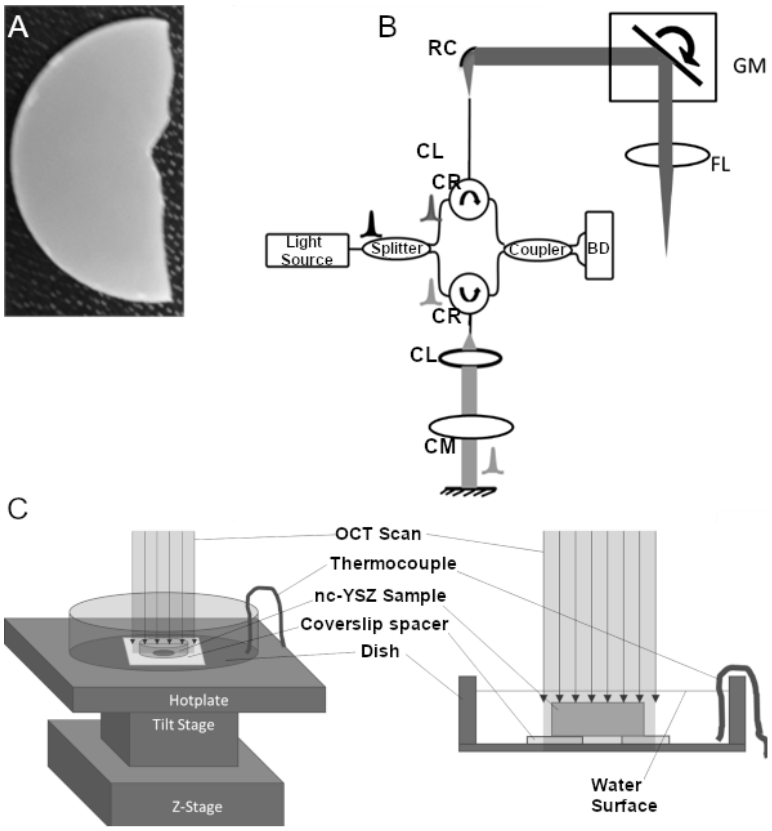

Figure 8.1. a) Photograph of nc-YSZ implant material. b) Schematic of bench-top OCT system. Intensity OCT uses a Mach-Zehnder interferometer with circulators in the sample and reference paths (CR) using balanced detection (BD) and dispersion compensation (CM). Sample path delivery fiber APC; and reference path uses a reflective collimator (RC). Sample path uses galvo-mirrors (GM) placed at the back focal plane of the scanning lens (FL). c) Experimental setup for temperature-dependent measurements.

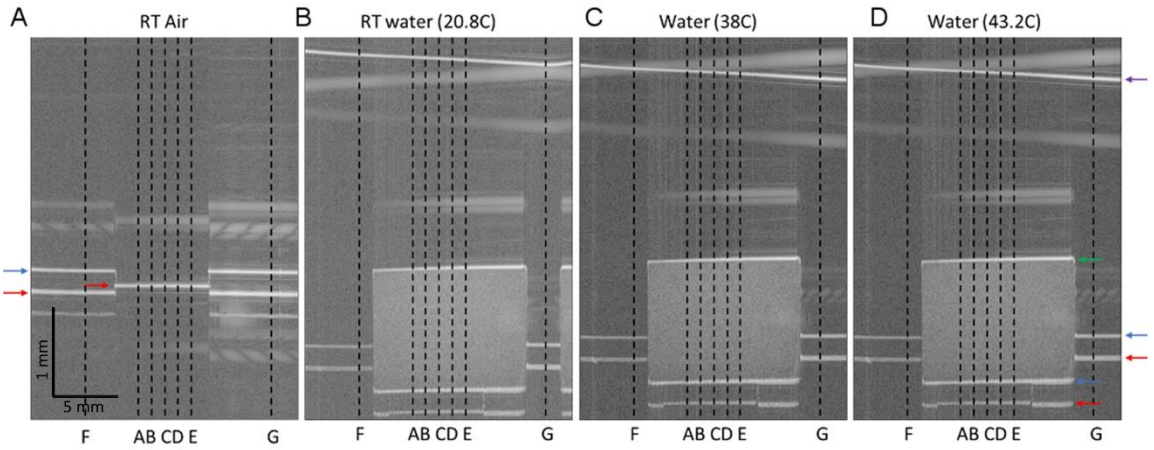

Figure 8.2. OCT B-Scans of nc-YSZ sample, with locations of interest identified. a) Spacer and dish imaged in air at room temperature, b) nc-YSZ sample imaged atop spacer and dish in water at room temperature (20.8°C), c) nc-YSZ imaged in water at 38°C, d) nc-YSZ imaged in water at 43.2°C. Locations A, B, C, D & E are used to analyze nc-YSZ optical properties, while F & G are used to measure the real vertical displacement of the experimental setup within the imaging field. Horizontal arrows highlight relevant surfaces (red = dish; blue = spacer top/nc-YSZ bottom; green = nc-YSZ top; purple = water surface).

Group Refractive Index of Water

Refractive index of water was calculated using reference data [237], and assuming 1.0221 bar atmospheric pressure. Refractive index values were calculated for several wavelengths near the central OCT wavelength of 1300 nm for each temperature of interest, and converted to group refractive index using Equation 1 [238]:

$$n_g = n - \lambda_0 \cdot (dn/d\lambda_0) \quad (1)$$

where n_g is the group refractive index, n is the phase index of wavelength λ, and λ_0 is the central OCT wavelength of 1300 nm. Calculated group refractive index values of water are 1.337, 1.339, and 1.340 at 20.8°C, 38°C, and 43.2°C, respectively.

Method 1: Image-based Analysis (Group Refractive Index and Sample Thickness)

Using Image J, distances within the image were quantified (in microns and pixels). At locations of interest (A, B, C, D, E, F & G in Figure 8.2), distances were measured from

the top of the image to the following features: top surface of spacer, bottom of dish, top and bottom surfaces of nc-YSZ sample, and surface of water (see Figure 8.2). From these measurements, and group refractive index values of water at 20.8°C, 38°C, and 43.2°C, it is possible to separate the total displacement in the image Δ_{total} into apparent displacement $\Delta_{apparent}$ of the dish bottom and/or spacer (due to non-unity group refractive index of water and nc-YSZ) and the real displacement Δ_{real} of the setup (due to compression and/or expansion of the temperature adjustable plate), using Equations 2 and 3:

$$\Delta_{total} = \Delta_{apparent} + \Delta_{real} \quad (2)$$

$$\Delta_{apparent} = T - d = T - \frac{T}{n_g} \quad (3)$$

Where T = optical thickness, d = real thickness, and n_g = group refractive index. First, the real displacement Δ_{real} of the setup at each temperature is found using the total displacement Δ_{total} of the spacer relative to the baseline image at locations F & G, where $\Delta_{apparent}$ is caused by n_{gwater} only. Combining Equations 2 and 3, Equation 4:

$$\Delta_{real} = \Delta_{total} - (T_{water} - \frac{T_{water}}{n_{gwater}}) \quad (4)$$

The room temperature (RT) image had a real downward displacement Δ_{real} = 4 px (~25 µm) relative to the baseline image in air. This is due to the weight of the water compressing the temperature adjustable plate. The 38°C image had a real upward displacement Δ_{real} = 2.5 px (~15 µm) relative to the baseline image in air. This is due to thermal expansion of the temperature adjustable plate and experimental setup, as well as evaporation of some of the water compared to the RT image. The 43.2°C image had a real upward displacement Δ_{real} = 4 px (~25 µm) relative to the baseline image in air, due to thermal expansion of the

temperature adjustable plate and experimental setup, as well as water evaporation compared to the RT and 38°C images.

Subtracting these real displacements from the total displacement Δ_{total} in the images (using Equation 2) yields the apparent displacement within the image. To calculate the group refractive index of nc-YSZ from the apparent displacement, the method is the same as that used to compute real displacement Δ_{real} above, except it is applied at locations A, B, C, D & E, where the apparent displacement $\Delta_{apparent}$ is due to non-unity group refractive index of water and nc-YSZ, using Equation 5:

$$\Delta_{apparent} = (T_{water} - d_{water}) + (T_{nc-YSZ} - d_{nc-YSZ})$$
$$= \left(T_{water} - \frac{T_{water}}{n_{gwater}}\right) + \left(T_{nc-YSZ} - \frac{T_{nc-YSZ}}{n_{gnc-YSZ}}\right) \quad (5)$$

Method 2: Spectral Phase Function based Analysis (Group Delay and Group Delay Dispersion)

The second method of analysis uses the spectral phase function to calculate group refractive index and chromatic dispersion [239]. The spectral phase function describes the relationship between the optical frequencies in the OCT pulse and the difference in phase for each frequency returning from the top and bottom surfaces of the nc-YSZ sample. The spectral phase function may be written as a Taylor series expanded about the central OCT optical frequency, Equation 6:

$$\Phi(\nu) = \Phi^{(0)} + \Phi^{(1)}(\nu_0)(\nu - \nu_0)' + \frac{1}{2}\Phi^{(2)}(\nu_0)(\nu - \nu_0)'' + \frac{1}{6}\Phi^{(3)}(\nu_0)(\nu - \nu_0)''' + \cdots \quad (6)$$

Where Φ is phase, ν is optical frequency, ν_0 is the central OCT optical frequency, $\Phi^{(0)}$ is a common phase shift, $\Phi^{(1)}(\nu_0)$ is the group delay (GD), $\Phi^{(2)}(\nu_0)$ is the group delay dispersion

(GDD), and higher order terms are higher order dispersion. Single A-lines were analyzed from the 5 locations of interest at the 3 temperatures. Each A-line was filtered using a Hilbert transform/narrowband phase-invariant spectral filter [240] to isolate photons returning from the top and bottom surfaces of the sample (defined by full-width-half-maximum, FWHM, of the intensity peaks at the surfaces). These two phase functions correspond to the spectral phase functions of light returned from the sample's top and bottom edges. Fitting this data with a polynomial curve can approximate the spectral phase function (Equation 6). Fourth-order polynomial fits of the optical phase vs frequency data were performed in MATLAB [241]. The curve fits were weighted by the normalized intensity spectrum of the OCT light source, and the high and low tails of the spectrum were trimmed by 200 pixels prior to the curve fitting to eliminate regions of low SNR and reduce the impact of noise. Root-mean-squared-error, RMSE, values were less than unity for all fits. The 1st order coefficient (Equation 6) of the spectral phase function approximation is the group delay (GD). The group delay of each interface corresponds to the actual optical path length difference between the interface and the reference arm. A subtraction of these GDs for the top and bottom interfaces corresponds to the distance the light experienced within the sample ($T = n_g \cdot d$, Equation 2). The 2nd order coefficient (Equation 6) of the spectral phase function of the bottom surface is the approximation of half of the group delay dispersion (GDD) the light experienced within the sample (from the top surface to the bottom surface of the sample).

Results

Group refractive index of nc-YSZ was determined at each location and each temperature using the image-based analysis (Method 1) described above (Table 1a). This method also allowed for determination of real sample thickness $d_{nc\text{-}YSZ}$ at each location and temperature, using the optical thickness *T* divided by the group refractive index *ng* (Equation 2) along with a calibration factor of 6.19 microns per pixel in the OCT image (Table 1b). This method is based on whole pixels, and an error analysis shows that the measurement has a 2% error.

Next, group delay (GD) of the nc-YSZ sample was calculated using the spectral phase function approach (Method 2) described above. The 1st order coefficient of the spectral phase function approximation (Equation 6) is the group delay (GD). The GD for each location and temperature are shown in Table 1c. From GD, group refractive index *ng* can be calculated using Equation 7 and sample thickness values $d_{nc\text{-}YSZ}$ obtained from Method 1 (Table 1b):

$$n_g = \frac{GD \cdot c}{4\pi \cdot d} \tag{7}$$

Where *c* = 2.998e+8 m/s. Group refractive index values calculated using Equation 7 are shown in Table 1d. Because this method uses sample thickness values determined from Method 1, it also has a 2% error in the calculated values of group refractive index, or an error of ~0.043.

The 2nd order coefficient of the spectral phase function approximation (Equation 6) is half of the group delay dispersion (GDD). The GDD for each location and temperature

are provided in Table 1e. Dividing the GDD by twice the sample thickness $d_{nc\text{-}YSZ}$ (round trip), the β-parameter of dispersion measured for the sample is shown in Table 1f.

$ng_{nc\text{-}YSZ}$	20.8°C	38°C	43.2°C
A	2.159	2.159	2.168
B	2.164	2.150	2.165
C	2.176	2.164	2.159
D	2.176	2.174	2.159
E	2.181	2.173	2.176
Average	2.171	2.164	2.165
St. Dev	0.009	0.010	0.007

Table 1a. Group refractive index of nc-YSZ measured at 5 locations and 3 temperatures, using an image-based approach.

$d_{nc\text{-}YSZ}$	20.8°C	38°C	43.2°C
A	668 µm	668 µm	665 µm
B	669 µm	671 µm	663 µm
C	663 µm	669 µm	671 µm
D	666 µm	666 µm	674 µm
E	667 µm	669 µm	666 µm

Table 1b. Real thickness of nc-YSZ sample measured at the 5 locations and 3 temperatures, using an image-based approach.

GD	20.8°C	38°C	43.2°C
A	6.059e-11 s	6.034e-11 s	6.178e-11 s
B	6.059e-11 s	6.207e-11 s	6.116e-11 s
C	6.059e-11 s	6.126e-11 s	6.208e-11 s
D	6.125e-11 s	6.126e-11 s	6.118e-11 s
E	5.998e-11 s	6.147e-11 s	6.144e-11 s

Table 1c. Group delay of nc-YSZ sample measured at the 5 locations and 3 temperatures.

$ng_{nc\text{-}YSZ}$	20.8°C	38°C	43.2°C
A	2.165	2.156	2.218
B	2.162	2.208	2.202
C	2.182	2.186	2.209
D	2.196	2.196	2.167
E	2.147	2.194	2.202
Average	2.170	2.188	2.200
St. Dev	0.019	0.019	0.019

Table 1d. Group refractive index of nc-YSZ sample calculated from group delay and sample thickness.

GDD	20.8°C	38°C	43.2°C
A	-4.83e-27 s^2	-3.16e-27 s^2	1.40e-25 s^2
B	-7.74e-27 s^2	1.61e-25 s^2	7.18e-26 s^2
C	-4.71e-27 s^2	8.25e-26 s^2	1.59e-25 s^2
D	8.02e-26 s^2	8.26e-26 s^2	8.01e-26 s^2
E	-2.91e-25 s^2	-1.26e-25 s^2	7.89e-26 s^2

Table 1e. Group delay dispersion of nc-YSZ sample measured at the 5 locations and 3 temperatures.

B	20.8°C	38°C	43.2°C
A	-3.61e-24 s^2/m	-2.36e-24 s^2/m	1.05e-22 s^2/m
B	-5.79e-24 s^2/m	1.20e-22 s^2/m	5.41e-23 s^2/m
C	-3.55e-24 s^2/m	6.16e-23 s^2/m	1.18e-22 s^2/m
D	6.02e-23 s^2/m	6.20e-23 s^2/m	5.94e-23 s^2/m
E	-2.18e-22 s^2/m	-9.40e-23 s^2/m	5.92e-23 s^2/m

Table 1f. β-parameter of nc-YSZ sample calculated from GDD and sample thickness.

Dispersion values varied greatly between locations in the sample and between temperatures at a single location, even flipping sign between normal and anomalous dispersion. These values were reproducible by sequential A-lines at each location and temperature, causing us to believe this variability is not due to recording method or analysis.

Discussion

Group refractive index of the nc-YSZ window is important to consider when interpreting OCT images of underlying brain tissue, like those we reported previously [8]. Because OCT is a time-based imaging technique, on-axis dimensions in reconstructed OCT images depend on time-of-flight of the OCT pulse. When imaging across the WttB implant with a group refractive index of ~2.1, the implant appears 2.1 times its mechanical thickness, and displaces other features beneath the window downward in the image. This effect can be visualized in Figure 8.2(b-d), where the coverslip spacer beneath the nc-YSZ implant is displaced downward and appears discontinuous with the parts of the coverslip spacer on either side of the implant (blue arrows). Knowing the group refractive index is also important for focusing light through the window onto underlying tissue. Changes in group refractive index between the different temperatures investigated in this study (20°C-43°C) were very small, and within the 2% uncertainty of the sample thickness measurement. This temperature stability is not surprising, since YSZ has high thermal stability [193] and stable broadband IR reflection at much greater temperatures than those used in this study (i.e., >1400°C) [242].

Chromatic dispersion values were found to vary greatly across different sample locations and different temperatures at fixed locations, even flipping sign between normal and anomalous dispersion (Table 1e and Table 1f). Despite this great variability, individual measurements were reproducible by repeated A-lines at each fixed location and temperature. Thus, this variability may be a material property and not an artifact of data recording or analysis. The observed dispersion variation may be due to light scattering within the bulk of the sample at grain boundaries. Scattering within the sample is apparent in recorded OCT images shown in Figure 8.2, and is quantified in Figure 8.3 at location E for each temperature. This chromatic dispersion should be studied further, and will be an important consideration for any multispectral optical approaches that propagate light through the window where precise pulse duration needs to be maintained.

There were several limitations to the current study. As explained in the introduction, an additional method to validate the OCT findings was not conducted, due to the scattering properties of our samples and the need for simultaneous determination of the sample thickness at each location being interrogated. Additionally, while this measurement covered the wavelength range and temperature range anticipated for clinical applications of the implant with OCT brain imaging, wavelengths and temperature effects outside of this range were not assessed.

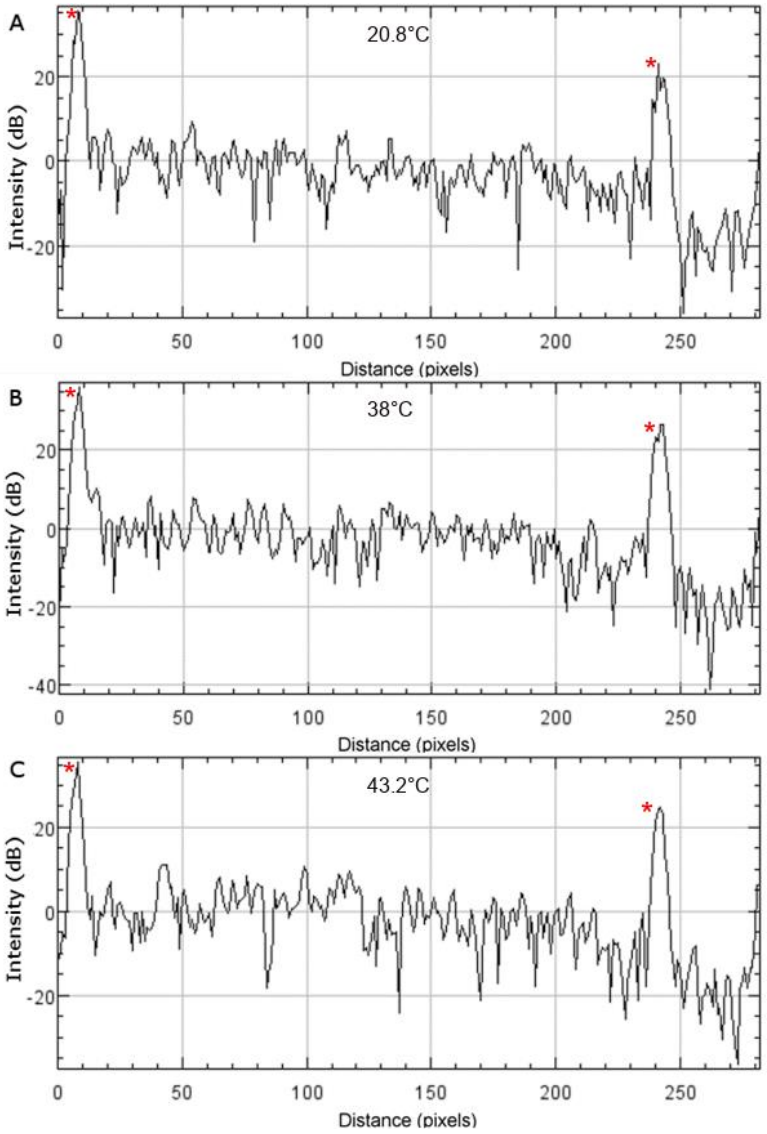

Figure 8.3. OCT intensity profiles of nc-YSZ sample at location E at a) 20.8°C RT, b) 38°C, and c) 43.2°C. The upper and lower surfaces of the sample are visible as intensity spikes on the left and right side of the profiles, respectively, and are identified with red asterisks.

Conclusion

Nc-YSZ cranial implant windows have a group refractive index of 2.1-2.2 for OCT imaging with a spectral range of 136 nm centered at 1300 nm at normal working implant temperatures (20°C-43°C). Chromatic dispersion for this spectral range was observed to

vary over the sample, sometimes flipping signs between normal and anomalous dispersion. These properties of nc-YSZ should be considered when designing optical systems and procedures that propagate light through the window.

Citation: The work presented in this chapter was submitted for publication to *Frontiers in Bioengineering and Biomedicine*:

> Halaney DL, Katta N, Fallah H, Aguilar G, Milner TE. Group Refractive Index of Nanocrystalline Yttria-Stabilized Zirconia Transparent Cranial Implants. *Fronteirs in Bioengineering and Biomedicine* (*submitted* October 2020).

Acknowledgments

I would like to acknowledge the contribution of my co-authors to this work: Nitesh Katta, Hamidreza Fallah, Guillermo Aguilar, Thomas E. Milner. This work was supported by the National Science Foundation (NSF-PIRE 1545852). The authors acknowledge Gottlieb Uahengo for providing the nc-YSZ sample used in this study.

Chapter 9. Recommendations for Future Work

While the results presented in this dissertation provide a proof-of-concept that the Window to the Brain implant can fulfill its promise to provide long-term optical access to the brain for imaging, there is much more work to be done before this technology can benefit patients. In this chapter, I provide my recommendations on next steps and future directions to realize the full potential of this cranial implant for chronic brain imaging and therapeutic applications.

Optical Therapy

As demonstrated in the previous chapters, the Window to the Brain nc-YSZ implant allows transmission of light to and from the brain. Specific successful examples include continuous wave (CW) laser irradiation at 810 nm for LSI imaging (see Chapters 2, 3, and 4) and laser bacterial antifouling (see Chapter 6), white light from flash lamps from 560 nm – 610 nm for MSRI (see Chapter 4) and for optical transmittance characterization from 500 nm – 1000 nm (see Chapter 7) and 900 nm – 2400 nm (see Chapter 5), and spectral-domain OCT source at 1298 nm ± 60 nm (see Chapter 3) and swept-source OCT source at 1300 nm ± 68 nm (see Chapter 8). Other examples of successful transmittance of laser across the window include, not included in this dissertation, include femtosecond laser pulses at 1030 nm [243, 244]. However, I encountered problems when attempting to perform laser coagulation of blood vessels across the window using microsecond laser pulses at 1070 nm. In this case, the laser caused the window to ablate when focused, and crack when unfocused, using 50 μs pulses with a 10% duty cycle and power of 45W and higher. This phenomenon may be due to absorption by trapped gasses in pores within the

nc-YSZ, or due to microcracks or other defects from the CAPAD densification or polishing steps in sample fabrication and preparation, although these hypotheses require further study to understand, so that problematic laser schemes can be avoided or the window manufacturing process can be improved to avoid these issues in the future. Until this issue is understood, I recommend that avoiding microsecond laser strategies in animal models and patient applications.

Laser Bacterial Antifouling

As discussed in Chapter 6, bacterial infection and fouling of cranial implants represents the leading cause of conventional cranial implant failure, typically necessitating implant removal and replacement through additional invasive open-skull procedures. The optical transparency of the Window to the Brain implant creates the potential to treat bacterial infection and fouling of the implant *in situ*, using laser irradiation. Chapter 6 explored the use of continuous wave and chopped continuous wave NIR irradiation, which was somewhat successful but limited due to heating of the implant. Other related *in vitro* studies [243, 244] have shown efficacy killing bacteria (E. coli and S. aureus) across the window without causing the implant to heat up, using femtosecond laser irradiation, antibacterial nanoparticles of zinc oxide and titanium nitride, or a combination of these nanoparticles and femtosecond laser irradiation. While these *in vitro* studies show promise, *in vivo* studies are needed to determine if these strategies are effective enough to mitigate infection of the implant *in situ*, within the cranial environment and eliminate fouling of the implant to restore clear optical access to the brain. The survival mouse model described in Chapters

2 and 3 could be easily adapted for this purpose, by growing E. coli or S. aureus on the Window to the Brain cranial implant prior to implantation.

LSI Imaging of Brain Hemodynamics Across the Window

As discussed in Chapters 2 and 4, LSI is a simple and inexpensive imaging technique which can provide relative velocity blood flow maps of the brain across the Window to the Brain implant, including the microvasculature. In Chapter 4, this technique was combined with MSRI to allow for determination of veins vs. arteries. While this information has clinical and scientific utility (e.g., in the study of stroke), additional complementary information would make this imaging strategy even more useful. Specifically, the combination with other intrinsic optical signal imaging methods such as pulse oximetry to provide oxygen partial pressure information, spatially co-registered with the flow velocity maps, could help determine regions of ischemic damage after stroke. In addition, by merging an extrinsic optical signal imaging method like calcium-sensitive fluorescent imaging and LSI, simultaneous acquisition of a brain blood flow map as well as measures of brain activity could be achieved. Advances in LSI image acquisition and processing to decrease the influence of motion artifacts and increase the depth and resolution of imaging would also extend the usefulness of this technique.

Coupling of Optical Fiber Devices with the Window to the Brain for Extended Theranostic Applications

The Window to the Brain implant allows light to pass through, circumventing the optical barrier of the skull. As discussed in Chapter 5, optical clearing agents can render the scalp temporarily transparent, to allow for optical access to the window without scalp resection.

Despite this access, attenuation of light within the optically-cleared scalp, Window to the Brain implant, and brain tissue itself limits the depth within the brain at which imaging and therapy can be performed. Infrared wavelengths can penetrate deeper into brain tissue than visible light, but attenuation still limits the resolution and effective optical dose that can be achieved. One potential way that deeper theranostics could be achieved is by coupling optical fibers to the Window to the Brain implant. These fibers could be implanted in the brain at the time of implant placement, to locations where deeper therapy is needed. Several optical fiber devices including temperature [245] and pressure probes and optical fiber microheaters [246] have been developed which could be used in such a scenario. Optrodes [247] represent another fiber device which could be used in conjunction with the Window to the Brain. In general, any fiber device could be allocated either adjacent or butt-coupled and glued to the window. In the case of directly coupling the fiber to the window, thermal effects may appear, heating the nc-YSZ. These effects will need to be studied and potentially mitigated before application in patients.

Optical Waveguides to Direct Light Across the Window to the Brain Implant

While the Window to the Brain implant allows for light to pass through the implant to and from the brain, the transmittance is limited, particularly for visible wavelengths. Moreover, light scattering within the window, as discussed in Chapter 8, results in some backscatter and chromatic dispersion which could temporally broaden broadband light pulses. Related studies have shown that waveguides of various types can be written into the nc-YSZ windows [62, 248, 249], which could channel light more effectively than passing it directly across the window unguided. Moreover, waveguides written in different geometries along

and across the window (e.g., divergent waveguides) could allow for light to be spread out across the brain surface and/or focused when returning from the brain. Waveguides could also aid in coupling light to and from optical fibers, as discussed in the proceeding section. An important next step will be to optimize these waveguides for NIR wavelengths, since it is this type of light that is commonly used for tissue interactions in medical applications, and because the nc-YSZ transmits light much more effectively in this part of the spectrum.

References

1. Bonda, D.J., et al., *The Recent Revolution in the Design and Manufacture of Cranial Implants: Modern Advancements and Future Directions.* Neurosurgery, 2015. **77**(5): p. 814-824.

2. Roome, C.J. and B. Kuhn, *Chronic cranial window with access port for repeated cellular manipulations, drug application, and electrophysiology.* Front Cell Neurosci, 2014. **8**: p. 379.

3. Zuluaga-Ramirez, V., S. Rom, and Y. Persidsky, *Craniula: A cranial window technique for prolonged imaging of brain surface vasculature with simultaneous adjacent intracerebral injection.* Fluids and Barriers of the CNS, 2015. **12**: p. 24.

4. Heo, C., et al., *A soft, transparent, freely accessible cranial window for chronic imaging and electrophysiology.* Sci Rep, 2016. **6**: p. 27818.

5. Garay, J.E., *Current-Activated, Pressure-Assisted Densification of Materials.* Annual Review of Materials Research, 2010. **40**(1): p. 445-468.

6. Damestani, Y., et al., *Transparent nanocrystalline yttria-stabilized-zirconia calvarium prosthesis.* Nanomedicine, 2013. **9**(8): p. 1135-8.

7. Davoodzadeh, N., et al., *Evaluation of a transparent cranial implant as a permanent window for cerebral blood flow imaging.* Biomedical Optics Express, 2018. **9**(10): p. 4879-4892.

8. Halaney, D.L., et al., *Chronic Brain Imaging Across a Transparent Nanocrystalline Yttria-Stabilized-Zirconia Cranial Implant.* Front Bioeng Biotechnol, 2020. **8**: p. 659.

9. Davoodzadeh, N., et al., *Optical Access to Arteriovenous Cerebral Microcirculation Through a Transparent Cranial Implant.* Lasers in Surgery and Medicine, 2019. **51**(10): p. 920-932.

10. Cano-Velázquez, M.S., et al., *Enhanced near infrared optical access to the brain with a transparent cranial implant and scalp optical clearing.* Biomedical optics express, 2019. **10**(7): p. 3369-3379.

11. Damestani, Y., et al., *Evaluation of laser bacterial anti-fouling of transparent nanocrystalline yttria-stabilized-zirconia cranial implant.* Lasers in Surgery and Medicine, 2016: p. 782–789.

12. Davoodzadeh, N., et al., *Characterization of ageing resistant transparent nanocrystalline yttria-stabilized zirconia implants.* J Biomed Mater Res B Appl Biomater, 2019.

13. Asakura, T. and N. Takai, *Dynamic laser speckles and their application to velocity measurements of the diffuse object.* Applied physics, 1981. **25**(3): p. 179-194.

14. Fujii, H., et al., *Evaluation of blood flow by laser speckle image sensing. Part 1.* Appl Opt, 1987. **26**(24): p. 5321-5.

15. Rothberg, S.J. and B.J. Halkon. *Laser vibrometry meets laser speckle*. in *Sixth International Conference on Vibration Measurements by Laser Techniques: Advances and Applications*. 2004. SPIE.

16. Fujii, H., T. Asakura, and Y. Shindo, *Measurement of surface roughness properties by using image speckle contrast.* Journal of the Optical Society of America, 1976. **66**(11): p. 1217-1222.

17. Tang, M.X., et al., *Photoacoustics, thermoacoustics, and acousto-optics for biomedical imaging.* Proc Inst Mech Eng H, 2010. **224**(2): p. 291-306.

18. Li, J., G. Ku, and L.V. Wang, *Ultrasound-modulated optical tomography of biological tissue by use of contrast of laser speckles.* Applied Optics, 2002. **41**(28): p. 6030-6035.

19. Briers, J.D. and S. Webster, *Laser speckle contrast analysis (LASCA): a nonscanning, full-field technique for monitoring capillary blood flow.* J Biomed Opt, 1996. **1**(2): p. 174-9.

20. Dunn, A.K., et al., *Dynamic imaging of cerebral blood flow using laser speckle.* J Cereb Blood Flow Metab, 2001. **21**(3): p. 195-201.

21. Cheng, H., et al., *Modified laser speckle imaging method with improved spatial resolution.* J Biomed Opt, 2003. **8**(3): p. 559-64.

22. Liu, Q., Z. Wang, and Q. Luo, *Temporal clustering analysis of cerebral blood flow activation maps measured by laser speckle contrast imaging.* J Biomed Opt, 2005. **10**(2): p. 024019.

23. Boas, D.A. and A.K. Dunn, *Laser speckle contrast imaging in biomedical optics.* Journal of Biomedical Optics, 2010. **15**(1): p. 011109.

24. Briers, J.D., *Laser speckle contrast imaging for measuring blood flow.* Optica Applicata, 2007. **37**.

25. Konishi, N. and H. Fujii. *Real-time visualization of retinal microcirculation by laser flowgraphy*. 1995. SPIE.

26. Li, P., et al., *Imaging cerebral blood flow through the intact rat skull with temporal laser speckle imaging.* Opt Lett, 2006. **31**(12): p. 1824-6.

27. Parthasarathy, A.B., S.M. Kazmi, and A.K. Dunn, *Quantitative imaging of ischemic stroke through thinned skull in mice with Multi Exposure Speckle Imaging.* Biomed Opt Express, 2010. **1**(1): p. 246-259.

28. Shih, A.Y., et al., *A polished and reinforced thinned-skull window for long-term imaging of the mouse brain.* J Vis Exp, 2012(61).

29. Wang, J., et al., *An innovative transparent cranial window based on skull optical clearing.* Laser Physics Letters, 2012. **9**(6): p. 469.

30. Li, N., et al., *High spatiotemporal resolution imaging of the neurovascular response to electrical stimulation of rat peripheral trigeminal nerve as revealed by in vivo temporal laser speckle contrast.* J Neurosci Methods, 2009. **176**(2): p. 230-6.

31. Zhu, D., et al., *Imaging dermal blood flow through the intact rat skin with an optical clearing method.* J Biomed Opt, 2010. **15**(2): p. 026008.

32. Chen, W., et al., *Cocaine-Induced Abnormal Cerebral Hemodynamic Responses to Forepaw Stimulation Assessed by Integrated Multi-wavelength Spectroimaging and Laser Speckle Contrast Imaging.* IEEE J Sel Top Quantum Electron, 2016. **22**(4).

33. Yuan, S., et al., *Determination of optimal exposure time for imaging of blood flow changes with laser speckle contrast imaging.* Appl Opt, 2005. **44**(10): p. 1823-30.

34. Aizu, Y., et al., *Measurements of flow velocity in a microscopic region using dynamic laser speckles based on the photon correlation.* Optics Communications, 1989. **72**(5): p. 269-273.

35. Smith, S.S., Magnusen, P. & Pletka, B. J., *Fracture toughness of glass using the indentation fracture technique.* Fracture Mechanics for Ceramics, Rocks, and Concrete (ASTM International), 1981.

36. Hulbert, S.F., *The use of alumina and zirconia in surgical implants.* An Introduction to Bioceramics, 1993. **1**: p. 25–40.

37. Damestani, Y., et al., *Inflammatory response to implantation of transparent nanocrystalline yttria-stabilized zirconia using a dorsal window chamber model.* Nanomedicine, 2016. **12**(7): p. 1757-1763.

38. Alaniz, J.E., et al., *Optical properties of transparent nanocrystalline yttria stabilized zirconia.* Optical Materials, 2009. **32**(1): p. 62-68.

39. Casolco, S.R., Xu, J. & Garay, J. E., *Transparent/translucent polycrystalline nanostructured yttria stabilized zirconia with varying colors.* Scr. Mater., 2008.

40. Christel, P., Meunier, A., Heller, M., Torre, J. P. & Peille, C. N., *Mechanical properties and short-term in-vivo evaluation of yttrium-oxide-partially-stabilized zirconia.* J. Biomed. Mater. Res., 1989. **23**: p. 45-61.

41. Nakamura, K., Kanno, T. & Milleding, P. , *Zirconia as a dental implant abutment material: a systematic review.* Aquat. Microb. Ecol. , 2010.

42. Christel, P.e.a., *Biomechanical compatibility and design of ceramic implants for orthopedic surgery.* Ann. N. Y. Acad. Sci., 1988. **523**: p. 234–256.

43. Gutierrez, M., et al., *Novel Cranial Implants of Yttria-Stabilized Zirconia as Acoustic Windows for Ultrasonic Brain Therapy.* Advanced Healthcare Materials, 2017. **6**(21): p. 1700214.

44. Davoodzadeh, N., et al. *Laser speckle imaging of brain blood flow through a transparent nanocrystalline yttria-stabilized-zirconia cranial implant*. in *SPIE BiOS*. 2018. SPIE.

45. Fauver, M., et al., *Three-dimensional imaging of single isolated cell nuclei using optical projection tomography.* Opt Express, 2005. **13**(11): p. 4210-23.

46. Hutchinson, E.B., et al., *Spatial flow-volume dissociation of the cerebral microcirculatory response to mild hypercapnia.* Neuroimage, 2006. **32**(2): p. 520-30.

47. Gourley, J.K. and D.D. Heistad, *Characteristics of reactive hyperemia in the cerebral circulation.* American Journal of Physiology-Heart and Circulatory Physiology, 1984. **246**(1): p. H52-H58.

48. Roustit, M. and J.L. Cracowski, *Assessment of endothelial and neurovascular function in human skin microcirculation.* Trends Pharmacol Sci, 2013. **34**(7): p. 373-84.

49. Rizzoni, D., et al., *How to assess microvascular structure in humans.* High Blood Press Cardiovasc Prev, 2011. **18**(4): p. 169-77.

50. Gnyawali, S.C., et al., *Retooling Laser Speckle Contrast Analysis Algorithm to Enhance Non-Invasive High Resolution Laser Speckle Functional Imaging of Cutaneous Microcirculation.* Scientific Reports, 2017. **7**: p. 41048.

51. Fowkes, F.G., et al., *Comparison of global estimates of prevalence and risk factors for peripheral artery disease in 2000 and 2010: a systematic review and analysis.* Lancet, 2013. **382**(9901): p. 1329-40.

52. Sokolnicki, L.A., et al., *Contribution of nitric oxide to cutaneous microvascular dilation in individuals with type 2 diabetes mellitus.* Am J Physiol Endocrinol Metab, 2007. **292**(1): p. E314-8.

53. Khalil, Z., et al., *Impaired peripheral endothelial microvascular responsiveness in Alzheimer's disease.* J Alzheimers Dis, 2007. **11**(1): p. 25-32.

54. Gnyawali, S.C., et al., *High-resolution harmonics ultrasound imaging for non-invasive characterization of wound healing in a pre-clinical swine model.* PLoS One, 2015. **10**(3): p. e0122327.

55. Eriksson, S., J. Nilsson, and C. Sturesson, *Non-invasive imaging of microcirculation: a technology review.* Med Devices (Auckl), 2014. **7**: p. 445-52.

56. Kisler, K., et al., *In vivo imaging and analysis of cerebrovascular hemodynamic responses and tissue oxygenation in the mouse brain.* Nat Protoc, 2018. **13**(6): p. 1377-1402.

57. Holtmaat, A., et al., *Long-term, high-resolution imaging in the mouse neocortex through a chronic cranial window.* Nat Protoc, 2009. **4**(8): p. 1128-44.

58. Costantini, I., et al., *A versatile clearing agent for multi-modal brain imaging.* Sci Rep, 2015. **5**: p. 9808.

59. Amyot, F., et al., *A Review of the Effectiveness of Neuroimaging Modalities for the Detection of Traumatic Brain Injury.* J Neurotrauma, 2015. **32**(22): p. 1693-721.

60. Szu, J.I., et al., *Thinned-skull Cortical Window Technique for In Vivo Optical Coherence Tomography Imaging.* Journal of Visualized Experiments : JoVE, 2012(69): p. 50053.

61. Cano-Velázquez MS, D.N., Halaney D, et al., *Evaluation of Optical Access to the Brain in the Near Infrared Range with a Transparent Cranial Implant.* In: Latin

America Optics and Photonics Conference. Optical Society of America, 2018: p. Tu5C.2.

62. Castillo-Vega, G.R., et al., *Waveguide-like structures written in transparent polycrystalline ceramics with an ultra-low fluence femtosecond laser.* Optical Materials Express, 2012. **2**(10): p. 1416-1424.

63. Wang, Y., et al., *GPU accelerated real-time multi-functional spectral-domain optical coherence tomography system at 1300 nm.* Opt Express, 2012. **20**(14): p. 14797-813.

64. Ren, H., et al., *Real-time in vivo blood-flow imaging by moving-scatterer-sensitive spectral-domain optical Doppler tomography.* Optics Letters, 2006. **31**(7): p. 927-929.

65. Tao, Y.K., A.M. Davis, and J.A. Izatt, *Single-pass volumetric bidirectional blood flow imaging spectral domain optical coherence tomography using a modified Hilbert transform.* Opt Express, 2008. **16**(16): p. 12350-61.

66. Srinivasan, V.J., et al., *OCT methods for capillary velocimetry.* Biomedical optics express, 2012. **3**(3): p. 612-629.

67. Baran, U. and R.K. Wang, *Review of optical coherence tomography based angiography in neuroscience.* Neurophotonics, 2016. **3**(1): p. 010902-010902.

68. Zhu, J., et al., *Can OCT Angiography Be Made a Quantitative Blood Measurement Tool?* Applied sciences (Basel, Switzerland), 2017. **7**(7): p. 687.

69. Hyle Park, B., et al., *Real-time fiber-based multi-functional spectral-domain optical coherence tomography at 1.3 μm.* Optics Express, 2005. **13**(11): p. 3931-3944.

70. Pierce, M.C., et al., *Simultaneous intensity, birefringence, and flow measurements with high-speed fiber-based optical coherence tomography.* Optics Letters, 2002. **27**(17): p. 1534-1536.

71. Vermeer, K.A., et al., *Depth-resolved model-based reconstruction of attenuation coefficients in optical coherence tomography.* Biomedical optics express, 2013. **5**(1): p. 322-337.

72. Raichle, M.E., *Behind the scenes of functional brain imaging: a historical and physiological perspective.* Proc Natl Acad Sci U S A, 1998. **95**(3): p. 765-72.

73. Raichle, M.E., *The neural correlates of consciousness: an analysis of cognitive skill learning.* Philos Trans R Soc Lond B Biol Sci, 1998. **353**(1377): p. 1889-901.

74. Schwartz, W.J., et al., *Metabolic mapping of functional activity in the hypothalamo-neurohypophysial system of the rat.* Science, 1979. **205**(4407): p. 723-5.

75. Ghaffari, H., et al., *Regulation of CSF and Brain Tissue Sodium Levels by the Blood-CSF and Blood-Brain Barriers During Migraine.* Frontiers in computational neuroscience, 2020. **14**: p. 4-4.

76. Gusnard, D.A., M.E. Raichle, and M.E. Raichle, *Searching for a baseline: functional imaging and the resting human brain.* Nat Rev Neurosci, 2001. **2**(10): p. 685-94.

77. Hyder, F., et al., *Quantitative functional imaging of the brain: towards mapping neuronal activity by BOLD fMRI.* NMR in Biomedicine, 2001. **14**(7-8): p. 413-431.

78. Ganesh, T., et al., *A non-invasive magnetic resonance imaging approach for assessment of real-time microcirculation dynamics.* Sci Rep, 2017. **7**(1): p. 7468.

79. Kidwell, C.S. and A.W. Hsia, *Imaging of the brain and cerebral vasculature in patients with suspected stroke: advantages and disadvantages of CT and MRI.* Curr Neurol Neurosci Rep, 2006. **6**(1): p. 9-16.

80. Holdsworth, D.W. and M.M. Thornton, *Micro-CT in small animal and specimen imaging.* Trends in Biotechnology, 2002. **20**(8): p. S34-S39.

81. Miles, K.A., *Perfusion imaging with computed tomography: brain and beyond.* Eur Radiol, 2006. **16 Suppl 7**: p. M37-43.

82. Zhou, J., *Intraoperative imaging of the brain macro-and microcirculation.* Appl Cardiopulm Pathophysiol, 2012. **16**: p. 270-275.

83. Bash, S., et al., *Intracranial vascular stenosis and occlusive disease: evaluation with CT angiography, MR angiography, and digital subtraction angiography.* AJNR Am J Neuroradiol, 2005. **26**(5): p. 1012-21.

84. Towle, E.L., et al., *Comparison of indocyanine green angiography and laser speckle contrast imaging for the assessment of vasculature perfusion.* Neurosurgery, 2012. **71**(5): p. 1023-30; discussion 1030-1.

85. Scerrati, A., et al., *Indocyanine green video-angiography in neurosurgery: a glance beyond vascular applications.* Clin Neurol Neurosurg, 2014. **124**: p. 106-13.

86. Jonathan, E., J. Enfield, and M.J. Leahy, *Correlation mapping method for generating microcirculation morphology from optical coherence tomography (OCT) intensity images.* J Biophotonics, 2011. **4**(9): p. 583-7.

87. Hu, S., et al., *Functional transcranial brain imaging by optical-resolution photoacoustic microscopy.* J Biomed Opt, 2009. **14**(4): p. 040503.

88. Leahy, M., *Microcirculation Imaging.* John Wiley & Sons, 2012.

89. Devor, A., et al., *Frontiers in optical imaging of cerebral blood flow and metabolism.* J Cereb Blood Flow Metab, 2012. **32**(7): p. 1259-76.

90. Tsytsarev, V., et al., *Photoacoustic and optical coherence tomography of epilepsy with high temporal and spatial resolution and dual optical contrasts.* Journal of neuroscience methods, 2013. **216**(2): p. 142-145.

91. Gottschalk, S., et al., *Correlation between volumetric oxygenation responses and electrophysiology identifies deep thalamocortical activity during epileptic seizures.* Neurophotonics, 2017. **4**(1): p. 011007.

92. Zhang, Q., et al., *Wide-field optical coherence tomography based microangiography for retinal imaging.* Scientific Reports, 2016. **6**(1): p. 22017.

93. Sun, J., et al., *In vivo imaging of cerebral hemodynamics using high-frequency micro-ultrasound.* Cold Spring Harb Protoc, 2010. **2010**(9): p. pdb.prot5495.

94. Alam, S.K. and K.J. Parker, *Implementation issues in ultrasonic flow imaging.* Ultrasound Med Biol, 2003. **29**(4): p. 517-28.

95. Klein, K.U., et al., *Measurement of cortical microcirculation during intracranial aneurysm surgery by combined laser-Doppler flowmetry and photospectrometry.* Neurosurgery, 2011. **69**(2): p. 391-8.

96. Zhao, L., Li Y, Lu H, Yuan L, Tong S, *Separation of cortical arteries and veins in optical neurovascular imaging.* J Innov Opt Health Sci, 2014. **07**(03): p. 1350069.

97. Shi, R., et al., *Accessing to arteriovenous blood flow dynamics response using combined laser speckle contrast imaging and skin optical clearing.* Biomedical optics express, 2015. **6**(6): p. 1977-1989.

98. Ba, A.M., et al., *Multiwavelength optical intrinsic signal imaging of cortical spreading depression.* J Neurophysiol, 2002. **88**(5): p. 2726-35.

99. Dunn, A.K., et al., *Simultaneous imaging of total cerebral hemoglobin concentration, oxygenation, and blood flow during functional activation.* Opt Lett, 2003. **28**(1): p. 28-30.

100. Lu, G. and B. Fei, *Medical hyperspectral imaging: a review.* J Biomed Opt, 2014. **19**(1): p. 10901.

101. Torricelli, A., et al., *Time domain functional NIRS imaging for human brain mapping.* Neuroimage, 2014. **85 Pt 1**: p. 28-50.

102. Jones, P.B., et al., *Simultaneous multispectral reflectance imaging and laser speckle flowmetry of cerebral blood flow and oxygen metabolism in focal cerebral ischemia.* J Biomed Opt, 2008. **13**(4): p. 044007.

103. Afromowitz, M.A., et al., *Multispectral imaging of burn wounds: a new clinical instrument for evaluating burn depth.* IEEE Trans Biomed Eng, 1988. **35**(10): p. 842-50.

104. Ferris, D.G., et al., *Multimodal hyperspectral imaging for the noninvasive diagnosis of cervical neoplasia.* J Low Genit Tract Dis, 2001. **5**(2): p. 65-72.

105. Benavides, J., et al., *Multispectral digital colposcopy for in vivo detection of cervical cancer.* Opt Express, 2003. **11**(10): p. 1223-36.

106. Sakadzić, S., et al., *Simultaneous imaging of cerebral partial pressure of oxygen and blood flow during functional activation and cortical spreading depression.* Applied optics, 2009. **48**(10): p. D169-D177.

107. Shin, H.K., et al., *Normobaric hyperoxia improves cerebral blood flow and oxygenation, and inhibits peri-infarct depolarizations in experimental focal ischaemia.* Brain, 2007. **130**(Pt 6): p. 1631-42.

108. Shin, H.K., et al., *Mild induced hypertension improves blood flow and oxygen metabolism in transient focal cerebral ischemia.* Stroke, 2008. **39**(5): p. 1548-55.

109. Dunn, A.K., et al., *Spatial extent of oxygen metabolism and hemodynamic changes during functional activation of the rat somatosensory cortex.* Neuroimage, 2005. **27**(2): p. 279-90.

110. Drew, P.J., et al., *Chronic optical access through a polished and reinforced thinned skull.* Nature Methods, 2010. **7**: p. 981.

111. Hillman, E.M., *Optical brain imaging in vivo: techniques and applications from animal to man.* J Biomed Opt, 2007. **12**(5): p. 051402.

112. Bouchard, M.B., et al., *Ultra-fast multispectral optical imaging of cortical oxygenation, blood flow, and intracellular calcium dynamics.* Opt Express, 2009. **17**(18): p. 15670-8.

113. Zhang, C., et al., *A large, switchable optical clearing skull window for cerebrovascular imaging.* Theranostics, 2018. **8**(10): p. 2696-2708.

114. Zhao, Y.-J., et al., *Skull optical clearing window for in vivo imaging of the mouse cortex at synaptic resolution.* Light: Science & Applications, 2018. **7**(2): p. 17153-17153.

115. Chen, B.R., et al., *High-speed vascular dynamics of the hemodynamic response.* Neuroimage, 2011. **54**(2): p. 1021-30.

116. Davoodzadeh N, Uahengo G, Halaney D, Garay JE, Aguilar G. *"Influence of low temperature ageing on optical and mechanical properties of transparent yittria stabilized-zirconia cranial prosthesis."* Proceedings of SPIE BiOS, San Francisco, CA (2018).

117. Park, J., *Bioceramics: Properties, Characterizations, and Applications.* Springer Science & Business Media. 2009.

118. Robles, F.E., S. Chowdhury, and A. Wax, *Assessing hemoglobin concentration using spectroscopic optical coherence tomography for feasibility of tissue diagnostics.* Biomedical optics express, 2010. **1**(1): p. 310-317.

119. Frangi AF, N.W., Vincken KL, Viergever MA, *Multiscale vessel enhancement filtering.* In: Medical Image Computing and Computer-Assisted Intervention — MICCAI'98. Springer Berlin Heidelberg, 1998: p. 130-137.

120. Yousefi, S., et al., *Label-free optical lymphangiography: development of an automatic segmentation method applied to optical coherence tomography to visualize lymphatic vessels using Hessian filters.* J Biomed Opt, 2013. **18**(8): p. 86004.

121. Kroon, D., *Hessian based Frangi Vesselness filter. MATLAB Central File Exchange.* http://www.mathworks.com/matlabcentral/fileexchange/24409-hessian-based-frangivesselnessfilter. Accessed Mar 02, 2010. 2009.

122. Prahl, S. *Optical absorption of hemoglobin.* http://omlc.ogi.edu/spectra/hemoglobin. 1999. https://ci.nii.ac.jp/naid/20001378052/. Accessed December 17, 2018.

123. Dufour, S., et al., *Evaluation of laser speckle contrast imaging as an intrinsic method to monitor blood brain barrier integrity.* Biomed Opt Express, 2013. **4**(10): p. 1856-75.

124. Postnov, D.D., et al., *Cardiac pulsatility mapping and vessel type identification using laser speckle contrast imaging.* Biomedical Optics Express, 2018. **9**(12): p. 6388-6397.

125. Wang, Y., et al., *Cerebral artery-vein separation using 0.1-Hz oscillation in dual-wavelength optical imaging.* IEEE Trans Med Imaging, 2011. **30**(12): p. 2030-43.

126. Narasimha-Iyer, H., et al., *Automatic Identification of Retinal Arteries and Veins From Dual-Wavelength Images Using Structural and Functional Features.* IEEE Transactions on Biomedical Engineering, 2007. **54**(8): p. 1427-1435.

127. Schiessl, I., W. Wang, and N. McLoughlin, *Independent components of the haemodynamic response in intrinsic optical imaging.* Neuroimage, 2008. **39**(2): p. 634-46.

128. Vanzetta, I., R. Hildesheim, and A. Grinvald, *Compartment-resolved imaging of activity-dependent dynamics of cortical blood volume and oximetry.* J Neurosci, 2005. **25**(9): p. 2233-44.

129. Luo, Z., et al., *Simultaneous imaging of cortical hemodynamics and blood oxygenation change during cerebral ischemia using dual-wavelength laser speckle contrast imaging.* Opt Lett, 2009. **34**(9): p. 1480-2.

130. Zhang, H.F., et al., *Imaging of hemoglobin oxygen saturation variations in single vessels in vivo using photoacoustic microscopy.* Applied Physics Letters, 2007. **90**(5): p. 053901.

131. Miao P, L.M., Li N, et al. , *Detecting cerebral arteries and veins: from large to small.* J Innov Opt Health Sci, 2010. **03**(01): p. 61-67.

132. Feng, N., et al., *Simultaneous automatic arteries-veins separation and cerebral blood flow imaging with single-wavelength laser speckle imaging.* Opt Express, 2011. **19**(17): p. 15777-91.

133. Hu, D., et al., *Separation of arteries and veins in the cerebral cortex using physiological oscillations by optical imaging of intrinsic signal.* J Biomed Opt, 2010. **15**(3): p. 036025.

134. MacKenzie LE, H.A., *Oximetry using multispectral imaging: theory and application.* J Opt, 2018. **20**(6): p. 063501.

135. Jacques, S.L., *Optical properties of biological tissues: a review.* Phys Med Biol, 2013. **58**(11): p. R37-61.

136. Sordillo, L.A., et al., *Deep optical imaging of tissue using the second and third near-infrared spectral windows.* J Biomed Opt, 2014. **19**(5): p. 056004.

137. Hong, G., A.L. Antaris, and H. Dai, *Near-infrared fluorophores for biomedical imaging.* Nature Biomedical Engineering, 2017. **1**(1): p. 0010.

138. Bashkatov, A.N., et al., *Measurement of tissue optical properties in the context of tissue optical clearing.* J Biomed Opt, 2018. **23**(9): p. 1-31.

139. Golovynskyi, S., et al., *Optical windows for head tissues in near-infrared and short-wave infrared regions: Approaching transcranial light applications.* Journal of Biophotonics, 2018. **11**(12): p. e201800141.

140. Madsen, S.J., *Optical Methods and Instrumentation in Brain Imaging and Therapy*. 2012: Springer Science & Business Media.

141. Hong, G., et al., *Through-skull fluorescence imaging of the brain in a new near-infrared window.* Nature photonics, 2014. **8**(9): p. 723-730.

142. Shi, L., et al., *Transmission in near-infrared optical windows for deep brain imaging.* J Biophotonics, 2016. **9**(1-2): p. 38-43.

143. Curcio, J.A. and C.C. Petty, *The Near Infrared Absorption Spectrum of Liquid Water.* J. Opt. Soc. Am., 1951. **41**: p. 302-304.

144. Tsai, C.L., J.C. Chen, and W.J. Wang, *Near-infrared absorption property of biological soft tissue constituents.* J. Med. Biol. Eng., 2001(21): p. 7–14.

145. Tsukasaki, Y., et al., *Synthesis and optical properties of emission-tunable PbS/CdS core–shell quantum dots for in vivo fluorescence imaging in the second near-infrared window.* RSC Adv., 2014(4): p. 41164–41171.

146. Wilson, R.H., et al., *Review of short-wave infrared spectroscopy and imaging methods for biological tissue characterization.* J Biomed Opt, 2015. **20**(3): p. 030901.

147. James, N.S., et al., *Comparative tumor imaging and PDT Efficacy of HPPH conjugated in the mono- and di-forms to various polymethine cyanine dyes: part - 2.* Theranostics, 2013. **3**(9): p. 703-18.

148. Xu, H.T., et al., *Choice of cranial window type for in vivo imaging affects dendritic spine turnover in the cortex.* Nat Neurosci, 2007. **10**(5): p. 549-51.

149. Grutzendler, J., N. Kasthuri, and W.-B. Gan, *Long-term dendritic spine stability in the adult cortex.* Nature, 2002. **420**(6917): p. 812-816.

150. Lee, W.C., et al., *A dynamic zone defines interneuron remodeling in the adult neocortex.* Proc Natl Acad Sci U S A, 2008. **105**(50): p. 19968-73.

151. Genina, E.A., A.N. Bashkatov, and V.V. Tuchin, *Optical clearing of cranial bone.* Adv. Opt. Technol., 2008: p. 267867.

152. Sharova, A.S., et al., *Sapphire implant based neuro-complex for deep-lying brain tumors phototheranostics.* Journal of Physics: Conference Series, 2018. **945**: p. 012009.

153. Tuchin, V., *Tissue Optics Light Scattering Methods and Instruments for Medical Diagnosis*, in *SPIE*. 2000.

154. Tuchin, V.V., et al., *Light propagation in tissues with controlled optical properties.* J Biomed Opt, 1997. **2**(4): p. 401-17.

155. Genina, E.A., et al., *Optical clearing of tissues: Benefits for biology, medical diagnostics, and phototherapy*, in *Handbook of Optical Biomedical Diagnostics, Volume 2: Methods*. 2016, SPIE Press.

156. Salehpour, F., et al., *Near-infrared photobiomodulation combined with coenzyme Q10 for depression in a mouse model of restraint stress: reduction in oxidative stress, neuroinflammation, and apoptosis.* Brain Res Bull, 2019. **144**: p. 213-222.

157. Caldieraro, M.A. and P. Cassano, *Transcranial and systemic photobiomodulation for major depressive disorder: A systematic review of efficacy, tolerability and biological mechanisms.* J Affect Disord, 2019. **243**: p. 262-273.

158. Hamblin, M.R., *Photobiomodulation for traumatic brain injury and stroke.* J Neurosci Res, 2018. **96**(4): p. 731-743.

159. Hemmer, E., et al., *Exploiting the biological windows: current perspectives on fluorescent bioprobes emitting above 1000 nm.* Nanoscale Horiz, 2016. **1**(3): p. 168-184.

160. Xue, Z., S. Zeng, and J. Hao, *Non-invasive through-skull brain vascular imaging and small tumor diagnosis based on NIR-II emissive lanthanide nanoprobes beyond 1500 nm.* Biomaterials, 2018. **171**: p. 153-163.

161. Sordillo, D.C., et al., *Short wavelength infrared optical windows for evaluation of benign and malignant tissues.* J Biomed Opt, 2017. **22**(4): p. 45002.

162. Thiagarajah, J.R., M.C. Papadopoulos, and A.S. Verkman, *Noninvasive early detection of brain edema in mice by near-infrared light scattering.* J Neurosci Res, 2005. **80**(2): p. 293-9.

163. Shi, R., et al., *A useful way to develop effective in vivo skin optical clearing agents.* J Biophotonics, 2017. **10**(6-7): p. 887-895.

164. Zhu, D., et al., *Recent progress in tissue optical clearing.* Laser Photon Rev, 2013. **7**(5): p. 732-757.

165. Filatova, S.A., I.A. Shcherbakov, and V.B. Tsvetkov, *Optical properties of animal tissues in the wavelength range from 350 to 2600 nm.* J Biomed Opt, 2017. **22**(3): p. 35009.

166. Davoodzadeh, N., et al., *Assessment of bacteria growth under transparent nanocrystalline yttria stabilized-zirconia cranial implant using laser speckle imaging.* Lasers in Surgery and Medicine, 2018. **50**: p. S5–S6.

167. Damestani, Y., et al., *Optical clearing agent perfusion enhancement via combination of microneedle poration, heating and pneumatic pressure.* Lasers in Surgery and Medicine, 2014. **46**(6): p. 488-498.

168. Briggs, S., et al., *Gram-negative bacillary meningitis after cranial surgery or trauma in adults.* Scand J Infect Dis, 2004. **36**(3): p. 165-73.

169. Gordon, C.R., et al., *Multidisciplinary approach for improved outcomes in secondary cranial reconstruction: introducing the pericranial-onlay cranioplasty technique.* Neurosurgery, 2014. **10 Suppl 2**(0 2): p. 179-89; discussion 189-90.

170. Moreira-Gonzalez, A., et al., *Clinical outcome in cranioplasty: critical review in long-term follow-up.* J Craniofac Surg, 2003. **14**(2): p. 144-53.

171. Stephens, F.L., et al., *Cranioplasty complications following wartime decompressive craniectomy.* Neurosurg Focus, 2010. **28**(5): p. E3.

172. Yadla, S., et al., *Effect of early surgery, material, and method of flap preservation on cranioplasty infections: a systematic review.* Neurosurgery, 2011. **68**(4): p. 1124-9; discussion 1130.

173. Busscher, H.J., R.J. Ploeg, and H.C. van der Mei, *SnapShot: Biofilms and biomaterials; mechanisms of medical device related infections.* Biomaterials, 2009. **30**(25): p. 4247-8.

174. Wang, K.W., et al., *Post-neurosurgical nosocomial bacterial meningitis in adults: microbiology, clinical features, and outcomes.* J Clin Neurosci, 2005. **12**(6): p. 647-50.

175. du Moulin, G.C., et al., *E. coli peritonitis and bacteremia cause increased blood-brain barrier permeability.* Brain Res, 1985. **340**(2): p. 261-8.

176. Dashti, S.R., et al., *Operative intracranial infection following craniotomy.* Neurosurg Focus, 2008. **24**(6): p. E10.

177. Goh, R.C.W., et al., *Customised fabricated implants after previous failed cranioplasty.* Journal of Plastic, Reconstructive & Aesthetic Surgery, 2010. **63**(9): p. 1479-1484.

178. Haas, R., et al., *Elimination of bacteria on different implant surfaces through photosensitization and soft laser. An in vitro study.* Clin Oral Implants Res, 1997. **8**(4): p. 249-54.

179. Mason, M.L., *Using the laser for implant maintenance.* Dent Today, 1992. **11**(4): p. 74-5.

180. Kato, T., H. Kusakari, and E. Hoshino, *Bactericidal efficacy of carbon dioxide laser against bacteria-contaminated titanium implant and subsequent cellular adhesion to irradiated area.* Lasers Surg Med, 1998. **23**(5): p. 299-309.

181. Block, C.M., J.A. Mayo, and G.H. Evans, *Effects of the Nd:YAG dental laser on plasma-sprayed and hydroxyapatite-coated titanium dental implants: surface alteration and attempted sterilization.* Int J Oral Maxillofac Implants, 1992. **7**(4): p. 441-9.

182. Eriksson, A.R. and T. Albrektsson, *Temperature threshold levels for heat-induced bone tissue injury: a vital-microscopic study in the rabbit.* J Prosthet Dent, 1983. **50**(1): p. 101-7.

183. Kreisler, M., H. Al Haj, and B. d'Hoedt, *Temperature changes at the implant-bone interface during simulated surface decontamination with an Er:YAG laser.* Int J Prosthodont, 2002. **15**(6): p. 582-7.

184. Geminiani, A., J.G. Caton, and G.E. Romanos, *Temperature increase during CO(2) and Er:YAG irradiation on implant surfaces.* Implant Dent, 2011. **20**(5): p. 379-82.

185. He, X., *Thermostability of biological systems: fundamentals, challenges, and quantification.* The open biomedical engineering journal, 2011. **5**: p. 47-73.

186. Contag, C.H., et al., *Photonic detection of bacterial pathogens in living hosts.* Mol Microbiol, 1995. **18**(4): p. 593-603.

187. Dinjaski, N., et al., *Near-infrared fluorescence imaging as an alternative to bioluminescent bacteria to monitor biomaterial-associated infections.* Acta Biomater, 2014. **10**(7): p. 2935-44.

188. Hamblin, M.R., et al., *Rapid control of wound infections by targeted photodynamic therapy monitored by in vivo bioluminescence imaging.* Photochem Photobiol, 2002. **75**(1): p. 51-7.

189. Sennhenn-Kirchner, S., et al., *Decontamination of rough titanium surfaces with diode lasers: microbiological findings on in vivo grown biofilms.* Clin Oral Implants Res, 2007. **18**(1): p. 126-32.

190. Nussbaum, E.L., L. Lilge, and T. Mazzulli, *Effects of low-level laser therapy (LLLT) of 810 nm upon in vitro growth of bacteria: relevance of irradiance and radiant exposure.* J Clin Laser Med Surg, 2003. **21**(5): p. 283-90.

191. Kim, S., et al., *In vitro bactericidal effects of 625, 525, and 425 nm wavelength (red, green, and blue) light-emitting diode irradiation.* Photomed Laser Surg, 2013. **31**(11): p. 554-62.

192. Kodera, et al., *Transmitting, emitting and controlling light: Processing of transparent ceramics using current-activated pressure-assisted densification.* Scripta Materialia, 2013(69): p. 149-154.

193. Ghosh, S., et al., *Thermal properties of the optically transparent pore-free nanostructured yttria-stabilized zirconia.* Journal of Applied Physics, 2009. **106**(11): p. 113507.

194. Amaya, C., et al., *A non-destructive method for determination of thermal conductivity of YSZ coatings deposited on Si substrates.* Materials Chemistry and Physics, 2012. **136**(2): p. 917-924.

195. Hauser-Gerspach, I., S. Stübinger, and J. Meyer, *Bactericidal effects of different laser systems on bacteria adhered to dental implant surfaces: an in vitro study comparing zirconia with titanium.* Clin Oral Implants Res, 2010. **21**(3): p. 277-83.

196. Cho, Y.R. and A.K. Gosain, *Biomaterials in craniofacial reconstruction.* Clin Plast Surg, 2004. **31**(3): p. 377-85, v.

197. Darouiche, R.O., *Antimicrobial Approaches for Preventing Infections Associated with Surgical Implants.* Clinical Infectious Diseases, 2003. **36**(10): p. 1284-1289.

198. Stübinger, S., et al., *Effect of Er:YAG, CO(2) and diode laser irradiation on surface properties of zirconia endosseous dental implants.* Lasers Surg Med, 2008. **40**(3): p. 223-8.

199. Nussbaum, E.L., L. Lilge, and T. Mazzulli, *Effects of 810 nm laser irradiation on in vitro growth of bacteria: comparison of continuous wave and frequency modulated light.* Lasers Surg Med, 2002. **31**(5): p. 343-51.

200. Lee, J. and G. Kaletunç, *Evaluation of the Heat Inactivation of Escherichia coli and Lactobacillus plantarum by Differential Scanning Calorimetry.* Applied and Environmental Microbiology, 2002. **68**(11): p. 5379.

201. Hibst, R., et al., *Mechanism of high-power NIR laser bacteria inactivation.* J Biophotonics, 2010. **3**(5-6): p. 296-303.

202. Lubart, R., et al., *A possible mechanism for the bactericidal effect of visible light.* Laser therapy, 2011. **20**(1): p. 17-22.

203. Nandakumar, K., et al., *Laser impact on bacterial ATP: insights into the mechanism of laser-bacteria interactions.* Biofouling, 2003. **19**(2): p. 109-14.

204. Fournier, M., et al., *Mapping the distance between the brain and the inner surface of the skull: interest for the study of fossil endocasts*, in *80th annual meeting of the American Association of Physical Anthropologists*. 2011: Minneapolis, United States. p. 137-138.

205. Ando, T., et al., *Comparison of therapeutic effects between pulsed and continuous wave 810-nm wavelength laser irradiation for traumatic brain injury in mice.* PLoS One, 2011. **6**(10): p. e26212.

206. Majaron, B., et al., *Intermittent cryogen spray cooling for optimal heat extraction during dermatologic laser treatment.* Physics in Medicine and Biology, 2002. **47**(18): p. 3275-3288.

207. Anselmi-Tamburini, U., J.N. Woolman, and Z.A. Munir, *Transparent Nanometric Cubic and Tetragonal Zirconia Obtained by High-Pressure Pulsed Electric Current Sintering.* Advanced Functional Materials, 2007. **17**(16): p. 3267-3273.

208. Grasso, S., et al., *Highly Transparent Pure Alumina Fabricated by High-Pressure Spark Plasma Sintering.* Journal of the American Ceramic Society, 2010. **93**(9): p. 2460-2462.

209. Rosenflanz, A., et al., *Bulk glasses and ultrahard nanoceramics based on alumina and rare-earth oxides.* Nature, 2004. **430**(7001): p. 761-4.

210. Xiong, Y., et al., *Preparation of Transparent 3Y-TZP Nanoceramics with No Low-Temperature Degradation.* Journal of the American Ceramic Society, 2014. **97**(5): p. 1402-1406.

211. Aminfar, A., et al., *Application of optical flow algorithms to laser speckle imaging.* Microvascular Research, 2019. **122**: p. 52-59.

212. Davoodzadeh, N., et al. *Evaluation of a Transparent Cranial Implant for Multi-Wavelength Intrinsic Optical Signal Imaging*. in *Neural Imaging and Sensing, International Society for Optics and Photonics, 108650B.* 2019.

213. Halaney, D.L., et al. *Optical Coherence Tomography and Laser Speckle Imaging of the Brain Through a Transparent Cranial Implant in a Chronic Mouse Model*. in *Lasers in Surgery and Medicine*. 2018. Hoboken, NJ, USA.

214. Chevalier, J., B. Cales, and J.M. Drouin, *Low-Temperature Aging of Y-TZP Ceramics.* Journal of the American Ceramic Society, 1999. **82**(8): p. 2150-2154.

215. Lughi, V. and V. Sergo, *Low temperature degradation -aging- of zirconia: A critical review of the relevant aspects in dentistry.* Dent Mater, 2010. **26**(8): p. 807-20.

216. Chevalier, J., L. Gremillard, and S. Deville, *Low-Temperature Degradation of Zirconia and Implications for Biomedical Implants.* Annual Review of Materials Research, 2007. **37**(1): p. 1-32.

217. Muñoz-Saldaña, J., et al., *Mechanical properties and low-temperature aging of tetragonal zirconia polycrystals processed by hot isostatic pressing.* Journal of Materials Research, 2003. **18**(10): p. 2415-2426.

218. Deville, S., J. Chevalier, and L. Gremillard, *Influence of surface finish and residual stresses on the ageing sensitivity of biomedical grade zirconia.* Biomaterials, 2006. **27**(10): p. 2186-2192.

219. ASTM and International, *ASTM B962-13. For Testing AS, on Metal Powders MCB, Products MP. Standard Test Methods for Density of Compacted or Sintered Powder Metallurgy (PM) Products Using Archimedes' Principle*. 2009.

220. *ISO 13356:2008. Implants for surgery – Ceramic materials based on yttria-stabilized tetragonal zirconia (Y-TZP)*. 2008.

221. Keefer, K.D. and T.A. Michalske, *Determination of Phase Transformation Depth Profiles with Synchrotron Radiation.* Journal of the American Ceramic Society, 1987. **70**(4): p. 227-231.

222. Chevalier, J., *What future for zirconia as a biomaterial?* Biomaterials, 2006. **27**(4): p. 535-43.

223. Kim, D.-J., J.-W. Jang, and H.-L. Lee, *Effect of Tetravalent Dopants on Raman Spectra of Tetragonal Zirconia.* Journal of the American Ceramic Society, 1997. **80**(6): p. 1453-1461.

224. Aguilar, G., et al. *Influence of Low Temperature Ageing on Optical and Mechanical Properties of Transparent Yittria Stabilized-Zirconia Cranial Prosthesis*. in *SPIE*. 2018. San Francisco, California, United States.

225. Davoodzadeh, N. *Low-Temperature Ageing of Transparent Nanocrystalline Yttria-Stabilized-Zirconia Calvarium Prothesis*. in *Lasers in Surgery and Medicine*. 2017. Hoboken, NJ, USA.

226. Zhang, F., et al., *Highly-translucent, strong and aging-resistant 3Y-TZP ceramics for dental restoration by grain boundary segregation.* Acta Biomater, 2015. **16**: p. 215-22.

227. Tredici, I.G., et al., *Low temperature degradation resistant nanostructured yttria-stabilized zirconia for dental applications.* Ceramics International, 2016. **42**(7): p. 8190-8197.

228. Wei, C. and L. Gremillard, *Towards the prediction of hydrothermal ageing of 3Y-TZP bioceramics from processing parameters.* Acta Materialia, 2018. **144**: p. 245-256.

229. Pitzer, K.S., *Self-ionization of water at high temperature and the thermodynamic properties of the ions.* The Journal of Physical Chemistry, 1982. **86**(24): p. 4704-4708.

230. Perrichon, A., et al., *A testing protocol combining shocks, hydrothermal ageing and friction, applied to Zirconia Toughened Alumina (ZTA) hip implants.* J Mech Behav Biomed Mater, 2017. **65**: p. 600-608.

231. Sanon, C., et al., *A new testing protocol for zirconia dental implants.* Dent Mater, 2015. **31**(1): p. 15-25.

232. Lucas, T.J., et al., *Effect of grain size on the monoclinic transformation, hardness, roughness, and modulus of aged partially stabilized zirconia.* Dent Mater, 2015. **31**(12): p. 1487-92.

233. Zhang, et al., *Effect of cation dopant radius on the hydrothermal stability of tetragonal zirconia: Grain boundary segregation and oxygen vacancy annihilation.* Acta Materialia, 2016(106): p. 48-58.

234. Luo, J. and R. Stevens, *Porosity-dependence of elastic moduli and hardness of 3Y-TZP ceramics.* Ceramics International, 1999. **25**(3): p. 281-286.

235. Tearney, G.J., et al., *Determination of the refractive index of highly scattering human tissue by optical coherence tomography.* Opt. Lett., 1995. **20**: p. 2258-2260.

236. Yarmolenko, P.S., et al., *Thresholds for thermal damage to normal tissues: an update.* International journal of hyperthermia : the official journal of European Society for Hyperthermic Oncology, North American Hyperthermia Group, 2011. **27**(4): p. 320-343.

237. Thormählen, I., J. Straub, and U. Grigull, *Refractive Index of Water and Its Dependence on Wavelength, Temperature, and Density.* Journal of Physical and Chemical Reference Data, 1985. **14**(4): p. 933-945.

238. Paschotta, R., *article on 'Group Index'*, in *RP Photonics Encyclopedia*. 2021: https://www.rp-photonics.com/group_index.html.

239. Walmsley, I., L. Waxer, and C. Dorrer, *The role of dispersion in ultrafast optics.* Review of Scientific Instruments, 2001. **72**(1): p. 1-29.

240. Baumann, B., et al., *Full range complex spectral domain optical coherence tomography without additional phase shifters.* Optics express, 2007. **15**(20): p. 13375-13387.

241. Mathworks, *Curve Fitting Toolbox: User's Guide (R2020b).* Retrieved October 8, 2020 from https://www.mathworks.com/help/pdf_doc/curvefit/curvefit.pdf. 2020.

242. Leib, E.W., et al., *Yttria-stabilized zirconia microspheres: novel building blocks for high-temperature photonics.* Journal of Materials Chemistry C, 2016. **4**(1): p. 62-74.

243. Alvarez, C., et al., *Growth inhibition of Staphylococcus Aureus by a combined treatment of ZnO nanoparticles and femtosecond laser light*. 2019: Photonic Diagnosis and Treatment of Infections and Inflammatory Disease II. Vol. 10863. International Society for Optics and Photonics.

244. Luna-Palacios, Y., et al., *Femtosecond laser assisted antibacterial activity of ZnO nanoparticles*. 2017: Proceedings of the European Conferences on Biomedical Optics, Munich, Germany.

245. Sánchez-Escobar, S. and J. Hernández-Cordero, *Fiber optic fluorescence temperature sensors using up-conversion from rare-earth polymer composites*. 2019: Opt Lett. p. 1194-1197.

246. Hernández-Arenas, A., et al., *A fiber optic probe for thermal therapy*. 2020: NUSOD.

247. Chen, S., et al., *A fiber-based implantable multi-optrode array with contiguous optical and electrical sites.* Journal of Neural Engineering, 2013. **10**(4): p. 046020.

248. Castillo, G., et al., *Depressed-Cladding 3-D Waveguide Arrays Fabricated With Femtosecond Laser Pulses*. 2017: J Lightwave Technol. p. 2520-2525.

249. Guerra-Olvera, C., et al., *Circular Depressed Cladding Waveguides in Mechanically Robust, Biocompatible nc-YSZ Transparent Ceramics by fs Laser Pulses*. 2019: J Lightwave Technol. p. 3119-3126.